Edge region fluctuation measurements in the STOR-M tokamak

A Thesis Submitted to the

College of Graduate and Postdoctoral Studies

in Partial Fulfillment of the Requirements

for the Degree of Master of Science

in the Department of Physics & Engineering Physics

of College of Arts & Science

University of Saskatchewan

Saskatoon

By

Igor Voldiner

Permission to Use

In presenting this thesis in partial fulfilment of the requirements for a Postgraduate degree from the University of Saskatchewan, I agree that the Libraries of this University may make it freely available for inspection. I further agree that permission for copying of this thesis in any manner, in whole or in part, for scholarly purposes may be granted by the professor or professors who supervised my thesis work or, in their absence, by the Head of the Department or the Dean of the College in which my thesis work was done. It is understood that any copying or publication or use of this thesis or parts thereof for financial gain shall not be allowed without my written permission. It is also understood that due recognition shall be given to me and to the University of Saskatchewan in any scholarly use which may be made of any material in my thesis.

Requests for permission to copy or to make other use of material in this thesis in whole or part should be addressed to:

Dean

College of Graduate and Postdoctoral Studies

University of Saskatchewan

116 Thorvaldson Building, 110 Science Place

Saskatoon, Saskatchewan S7N 5C9

Canada

or

Head of the Department

Department of Physics and Engineering Physics

University of Saskatchewan

116 Science Place, Rm 163

Saskatoon, Saskatchewan S7N 5E2

Canada

ABSTRACT

Transport in plasma is one of the major topics related to modern magnetically confined fusion experiments. Anomalous transport that exceeds estimations of neoclassical transport theory is usually associated with micro-scale instabilities in plasma. Microwave, Langmuir-probe and magnetic diagnostics have been used to study fluctuations of the edge plasma in the Saskatchewan Torus Modified tokamak (STOR-M). The main work includes development, test and comparison of these diagnostic tools for investigation of edge plasma fluctuations. These fluctuations can play a role in particle and energy transport and are crucial for studies of improved-confinement regimes in tokamaks. The experiment set-up consists of movable triple Langmuir probe, discrete poloidal Mirnov coil array of 12 separate coils and fixed frequency ordinary mode reflectometer. Using measurements from the triple Langmuir probe at different insertions depths, the radial profiles of the mean electron temperature, plasma density, potential and, consequently, the radial electric field are obtained. Comparisons between different diagnostics are attempted when possible in order to validate experimental models used and to determine the scope of applicability of these diagnostic tools. Along with the studies, the poloidal MHD modes are extracted via application of Fourier analysis to Mirnov array signals. Strong similarity is found between the probe potential and magnetic fluctuation signals. The reflectometer signal on the other hand has shown little connections to other discharge parameters.

Acknowledgements

Dedicated to my beloved wife Liubov, my loving parents Maria and Alexey, dear sisters Jane and Vera and cherished grandmother Sveta. Without your love, support and trust I would never stand a chance to get this far.

Contents

List of Tables

LIST OF FIGURES

List of Abbreviations

2D	2-dimensional
AC	Alternating current
ADC	Analog to digital converter
CPSD	Cross-power spectral density
DAQ	Data acquisition
DC	Direct current
DFT	Discrete Fourier transform
EM	Electro-magnetic
ESD	Energy spectral density
ETG	Electron temperature gradient
FT	Fourier transform
HFS	High field side
IC	Integrated circuit
IDFT	Inverse discrete Fourier transform
IFT	Inverse Fourier transform
ITG	Ion temperature gradient
LCFS	Last closed flux surface
LFS	Low field side
LTFAT	Large time-frequency analysis toolbox
MCF	Magnetically confined fusion
MHD	Magneto hydro-dynamics
MVDF	Maxwellian velocity distribution function
MW	Micro-wave
PSD	Power spectral density
SOL	Scrape-off layer
SOL	Scrape-off layer
STFT	Short-time Fourier transform
STOR-M	Saskatchewan torus-modified
TEM	Trapped electron modes
TLP, TP	Triple Langmuir probe
VCO	Voltage controlled oscillator
VDF	Velocity distribution function
WKBJ	Wentzel-Kramers-Brillouin-Jeffreys approximation

Chapter 1

Introduction

This chapter introduces main concepts of plasma as a state of matter, idea of nuclear fusion, possible approaches towards it and main challenges that it poses. Also some background is provided in types and construction of magnetic confinement systems for fusion plasmas, their geometry, current achievements and roadblocks towards fusion as a commercially feasible source of energy. Diagnostic tools used in plasma fusion experiments are discussed with particular emphasis on ones that were used in this work. Then thesis motivation and objectives are formulated and the outline for the whole work is stated.

1.1 What is plasma

Plasma is a sufficiently large quasi-neutral aggregation of charged and neutral particles, in which collective interactions due to electromagnetic forces dominate over binary collisions, resulting in many remarkable effects, and unique properties [1], [2], [3]. Plasma exhibits diverse physical phenomena observed in various environments, often referred to as the "4th state of matter". This classification follows naturally from the conventional phase changes that occur with any material under heating: first transition happens from solid to liquid, second from liquid to gas. If additional energy is provided to gas, it is possible to break the bonds between nuclei and electrons, separating charged particles. Such a gas-like medium, that on the macro scale will have no net charges, is known as plasma. The characteristic energy scale of the transition energies for water (H_2O) is shown in Fig. 1.1. Energy required to separate an electron from atom, i.e. ionization energy, of a Hydrogen atom is 13.6 eV [1], and for other atoms lays approximately in the range from 5 eV to 25 eV. Being one of the fundamental states plasma forms more than 99% of observable matter in the universe. All of the stars, and interstellar media exist as plasma. However, plasma occurrence on Earth is not as common, yet it can still be witnessed in lightning, welding arcs, Aurora Borealis, etc. The phenomena associated with plasmas is extensive, so it comes as no surprise that studies of plasma are carried out worldwide for practical applications, such as space weather prediction, material processing, microelectronics manufacturing, medical applications and fusion energy.

---

[1]The energy unit eV, or electron-Volt is commonly used in plasma physics, 1 eV $\approx 1.6 \times 10^{-19}$ J
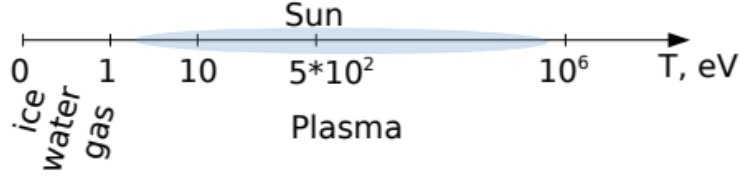
Figure 1.1: Phase transition energies for water.

1.2 Nuclear fusion

One of the most potentially important applications of plasma physics in the future is the controlled thermonuclear fusion energy. Bonding of two light nuclei, forming a heavier one and releasing energy is termed nuclear fusion, a promising and sustainable future energy source for mankind. Both fission and fusion nuclear reactions release energy based on the well known Einstein equation:

$$\Delta E = \Delta m c^2 \tag{1.1}$$

where ΔE is the released energy, Δm is the difference in mass between the reacting and resultant nuclei and c is the speed of light. Figure 1.2 shows the average binding energy per nucleon as a function of number of nucleons in nuclei. The energy released in fusion reactions, for example with formation of helium, are significantly larger in comparison to fission reactions. In order for fusion reactions to take place, it is necessary for the positively charged nuclei to overcome repelling electrostatic forces in order for reaction to take place. This energy barrier of electrostatic forces is smallest for isotopes of hydrogen because of singular positive charge. This explains why the first generation of fusion power plant will be based on fusion involving isotopes of hydrogen, such as deuterium $_1^2\text{D}$ and tritium $_1^3\text{T}$. Some of corresponding fusion reactions are listed below [4]:

$$_1^2\text{D} +_1^3\text{T} \rightarrow_2^4 \text{He}(3.5\text{MeV}) +_0^1 \text{n}(14.1\text{MeV}) \tag{1.2}$$

$$_1^2\text{D} +_1^2\text{D} \rightarrow_2^3 \text{He}(0.82\text{MeV}) +_0^1 \text{n}(2.45\text{MeV}) \tag{1.3}$$

$$_1^2\text{D} +_1^2\text{D} \rightarrow_1^3 \text{T}(1.01\text{MeV}) +_1^1 \text{p}(3.02\text{MeV}) \tag{1.4}$$

$$_1^2\text{D} +_2^3\text{He} \rightarrow_2^4 \text{He}(3.6\text{MeV}) +_1^1 p(14.7\text{MeV}) \tag{1.5}$$

For comparison, energy released in chemical reaction of oxidation of hydrogen (burning) is about 3 eV:

$$2H_2 + O_2 \rightarrow 2H_2O(2.96\text{eV}) \tag{1.6}$$

which is 6-7 orders of magnitude lower in comparison to nuclear fusion.

Probability of fusion reaction happening in collision between particles for each of the reactions above is
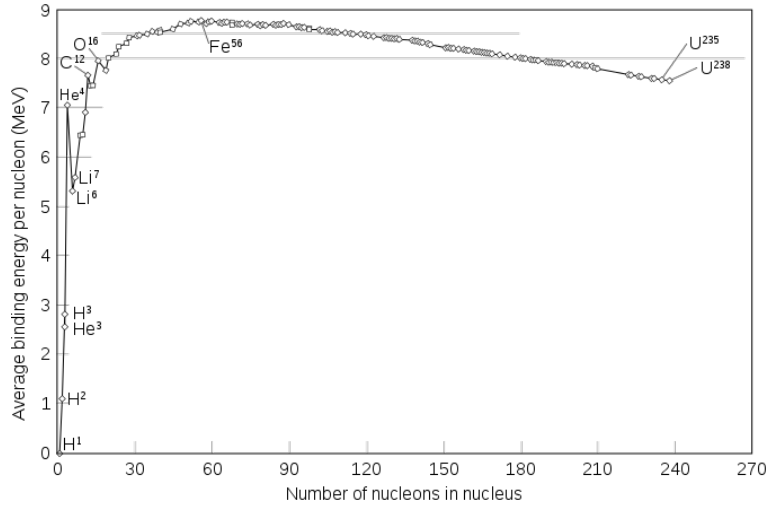
Figure 1.2: Binding energy as a function of number of nucleons. Adopted from: Wikimedia Commons. Average binding energy per nucleon in mev against number of nucleons in nucleus. `https://commons.wikimedia.org/wiki/File:Binding_energy_curve_-_common_isotopes.svg`. Accessed: 2019-06-09.

described by cross-section of this reaction. Cross-section depends on the relative velocities, v, or energy, E, between the reactants. Figure 1.3 represents cross-sections, $\sigma(E)$, associated with some of the reactions listed above. For a given velocity distribution of colliding particles, the reactivity $\langle \sigma v \rangle$ can be calculated by averaging product of reaction cross-section and velocity over velocity distribution function,

Reaction rate provides an estimate for number of reactions of the branch channel α per unit volume and per unit time between two different groups of particles with densities n_1 and n_2 respectively:

$$N_\alpha = n_1 n_2 \langle \sigma_\alpha v \rangle \tag{1.7}$$

Fusion reaction may be achieved by heating the nuclei in the plasma. When the kinetic energy of the colliding particles associated with their random thermal velocity is sufficiently high to overcome Coulomb barrier fusion reaction occurs. The reactivity, calculated based on Maxwellian distribution function, as a function of temperature peaks at a certain value as shown in Fig. 1.4. The maximum of reactivity for majority fusion reactions is reached when temperature is on order of tens of keV. In order to approach these temperatures, the fuel is heated and when its temperature gets comparable to its ionization energy it transitions to a plasma. This approach to nuclear fusion is called thermonuclear. It is important to efficiently confine extremely hot plasma so that the nuclei will have sufficient probability of undergoing fusion reaction before they escape the confinement device.

Thermonuclear reactions naturally occur in stars, where gravitational forces confine the plasma. If the appropriate conditions are created for extracting fusion energy in a controllable fashion, fusion reactors can provide humankind with abundant and ecologically friendly energy source. Unlike fission reactions which directly produce a considerable amount of long-life radioactive waste, fusion reactors do not. In fusion
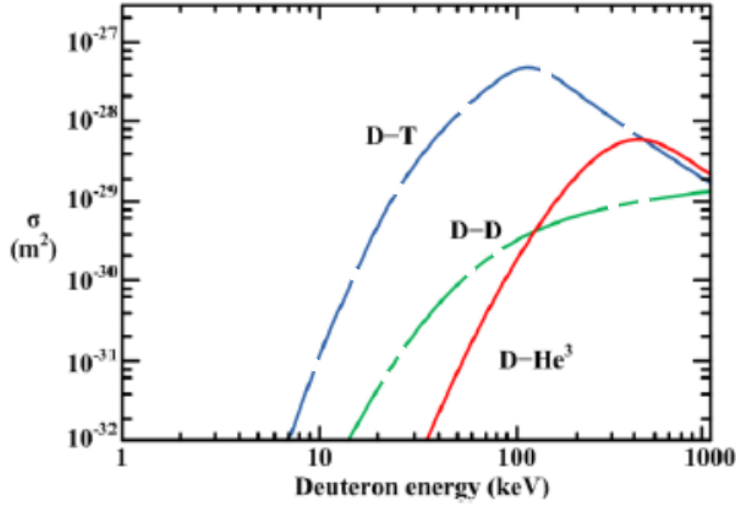
Figure 1.3: Cross-section against energy for some fusion reactions. Adopted from: J. Wesson. *Tokamak.* Oxford Science Publication, 2011.

reactors there is no danger of catastrophic accident, because the amount of reacting particles inside the device at any given time is too small to cause any significant damage to the facility or the environment. Malfunction will degrade the fusion condition and stop the reactor. Possibility of terrestrial thermonuclear reaction has already been proven in experiments with thermonuclear bombs back in the 1950s and multiple particle accelerator experiments. However controlling fusion reaction to produce net positive energy output still remains a topic of research.

It is possible to estimate conditions needed to reach the state of the so-called "ignition", when energy produced by fusion reactions is sufficient to compensate for energy losses due to imperfect confinement, thus maintaining reaction. The calculation involve concept of energy confinement time, τ_E , which is defined as energy density W in plasma divided by power loss density P_{loss}:

$$\tau_E = \frac{W}{P_{loss}} \tag{1.8}$$

where W can be expressed through kinetic energy of the plasma particles, which under assumption of thermal equilibrium and quasi-neutrality results in:

$$W = 3nk_BT \tag{1.9}$$

where n is the plasma density, T temperature, and k_B the Boltzmann constant.

It is necessary for power loss density to be lower than power released in reaction per unit volume per unit time. The energy carried by the resultant charged particles from the fusion reaction is assumed to heat the plasma. It is required that the product of volume rate of this reaction and energy of the resultant charged
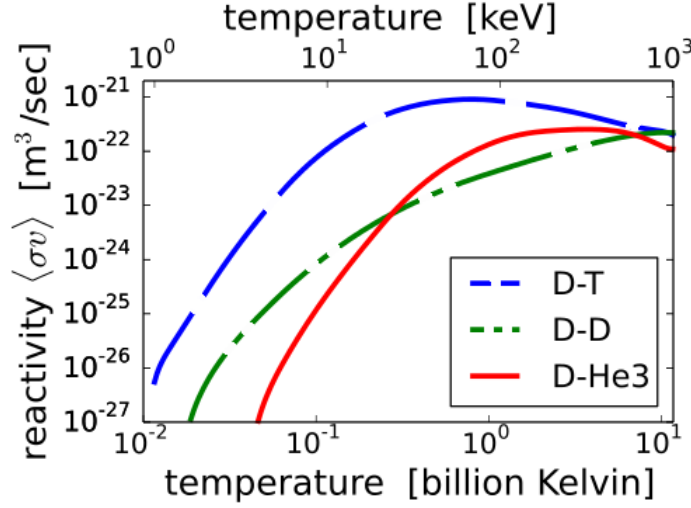
Figure 1.4: Reactivity against temperature for some fusion reactions. Based on data from: Naval Research Laboratory. *NRL: Plasma Formulary.* NRL, 2004.

particle per fusion reaction $E_{charged}$ is greater than the power loss:

$$NE_{charged} \geq P_{loss} \tag{1.10}$$

which leads to:

$$\frac{n^2 \langle \sigma v \rangle E_{charged}}{4} \geq \frac{3nk_BT}{\tau_E} \tag{1.11}$$

where factor of $\frac{1}{4}$ comes from consideration of equal amounts of Deuterium and Tritium in the plasma. Re-arranging yields:

$$n\tau_E \geq L \equiv \frac{12}{E_{charged}} \frac{k_BT}{\langle \sigma v \rangle} \tag{1.12}$$

where L is called Lawson criterion, derived by John Lawson in 1957 [8]. This criterion is used as a general minimum requirement of a fusion system. If maximum possible reactivity, i.e. optimal temperature of reactants is assumed and value of energy released with charged particles for deuterium-tritium reaction, $E_{charged} = 3.5\text{MeV}$ is substituted one will get for DT reaction:

$$n\tau_E \geq 1.5 \cdot 10^{20} \frac{\text{s}}{\text{m}^3} \tag{1.13}$$

To achieve 'ignition' and to make use of fusion reactions a viable energy source, it is necessary to confine plasma at high enough density and temperature for a long enough time. The triple product, $nT\tau$, is called the figure of merit of a fusion plasma system. The goal of the fusion research is to confine hot and dense plasma for a sufficiently long time. It should be pointed out that the energy confinement time in a tokamak fusion research device, on the order of second, is different from the operation time of a tokamak which can

be operated in a steady-state fashion. The energy confinement time is a characteristic time scale of energy degradation in the confined plasma, while operation time is determined by the power supply capacity for heating and confining systems of device in order to sustain the discharge.

1.3 Approaches to fusion

Plasma must reach extremely high temperatures in order for a feasible number of fusion reactions to take place in it. Not only there is no material in existence that could withstand direct contact with hot plasma under such harsh conditions, heating would be inefficient if plasma excessively deposits energy to the surroundings. Ideally, plasma should be separated from the wall of the chamber that confines it. There are two main approaches, along with their derivatives and various combinations, available for terrestrial fusion plasma confinement. They focus on reaching Lawson criterion either by creating extremely dense plasma for a short period of time or confining plasma with lower density for a longer period of time, corresponding to inertial confinement fusion (ICF) and magnetic confinement fusion (MCF) respectively. Magnetic confinement using the so called tokamak device will be discussed in more details in the following subsections.

1.3.1 Toroidal geometry

Plasma confinement configurations that are toroidal in shape are very common. A section of donut shaped toroid shown in Fig. 1.5 is symmetric to the vertical axis, $\mathbf{z}$, characterized by two parameters: major radius, R_0, the distance between the center axis of the torus to the symmetrical axis, and minor radius, a, the shortest distance from the surface of the toroid to the center axis of the torus. Any point within a toroid can be described by three variables. The minor radius, r, represents the distance from the point to the center axis of the torus on a vertical cross-section. Rotational angle about the center axis of the torus, θ, is called the poloidal angle. Rotational angle of major radius R, φ, about the vertical symmetrical axis is called toroidal angle. The horizontal plane that goes through the geometric center separating upper and lower halves of the torus is referred to as equatorial plane.

1.3.2 Magnetic confinement

In the straight and uniform magnetic field, the motion of a charged particle in the plane perpendicular to the magnetic field lines is a rotational motion around a magnetic field line due to Lorentz force. The radius of the circular orbit is the so-called Larmor radius, which is inversely proportional to magnetic field strength [1], [10]. For a sufficiently high magnetic field the Larmor radius becomes small enough compared to the characteristic length scale of the device, resulting in "trapping" of a particle around the field line, effectively limiting its motion perpendicular to the field line, as long as collisions are not considered. This is the basic concept of magnetic confinement. Magnetic field generated by straight solenoid coils can be used to create such field and confine plasma. However, the motion of the charged particles along the magnetic field line is not influenced
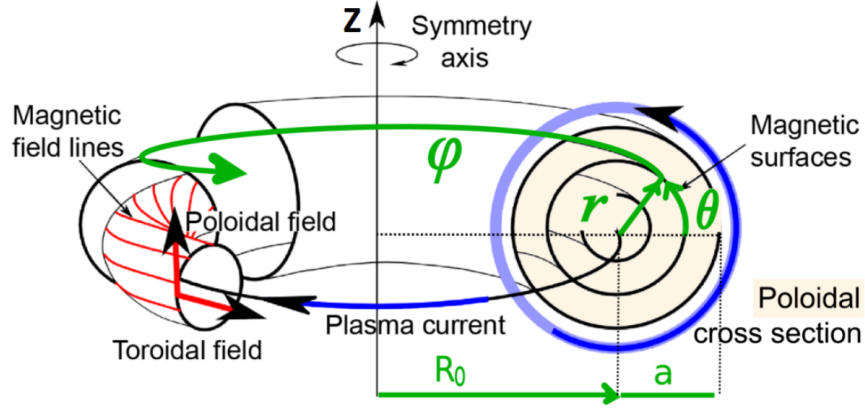
Figure 1.5: Toroidal coordinate system of tokamak. Adopted from: Olivier Février. *Global modelling of magnetic island control in tokamaks.* PhD thesis, Université d'Aix-Marseille, 2016.

by the magnetic field, leading to the so-called "end loss" of particles to the chamber wall intercepting the magnetic field lines. Even particles with initial zero axial velocity, due to the velocity deflection through Coulomb scattering in binary collisions, will eventually gain axial velocity and leave confinement region, carrying away particles and thermal energy. Such linear magnetic field configuration is not practical for fusion reactors. Other approaches such as "magnetic bottle" and "Ying-Yang"/"Baseball" magnetic configurations alter the magnetic field lines on the ends of the solenoid to reduce end losses. However, devices with axially symmetric magnetic field have to be proven for plasma confinement. An intuitive solution is to bend the solenoid so to connect its ends together, creating a torus. This indeed eliminates the problem of end losses. However, this transformation creates a curvature in the magnetic field lines and a gradient of magnetic field strength along the major radius direction (inversely proportional to major radius $\nabla B \propto 1/R$). When charged particles travel along the curved magnetic field lines, while gyrating around them, they experience centrifugal force due to curvature of the trajectory. The gradient and the curvature cause particles to drift perpendicular to the magnetic field lines at a velocity:

$$\mathbf{v}_{R,\nabla} = \frac{m}{2qB}\left(v_\parallel^2 + v_\perp^2\right)\frac{\mathbf{B} \times (\nabla B)}{B^2} \tag{1.14}$$

where $v_\parallel$ and $v_\perp$ are respectively velocities parallel and perpendicular to the field lines and m and q are particle mass and charge. So, direction of drift velocity depends on the sign of the charge, implying opposite drift directions for positively and negatively charged particles. The resultant charge separation in vertical direction induces the vertical electric field. This electric field, being perpendicular to the toroidal magnetic field $\mathbf{B}_\varphi$, causes yet another drift along major radius of the device, with velocity $\mathbf{v}_{\mathbf{E}\times\mathbf{B}}$:

$$\mathbf{v}_{\mathbf{E}\times\mathbf{B}} = \frac{\mathbf{E} \times \mathbf{B}}{B^2} \tag{1.15}$$

7

in the same direction for both ions and electrons, as depicted in Fig. 1.6, resulting in loss of both species, electrons and ions. Therefore this configuration with simple toroidal magnetic field lines is unable to confine plasma effectively.
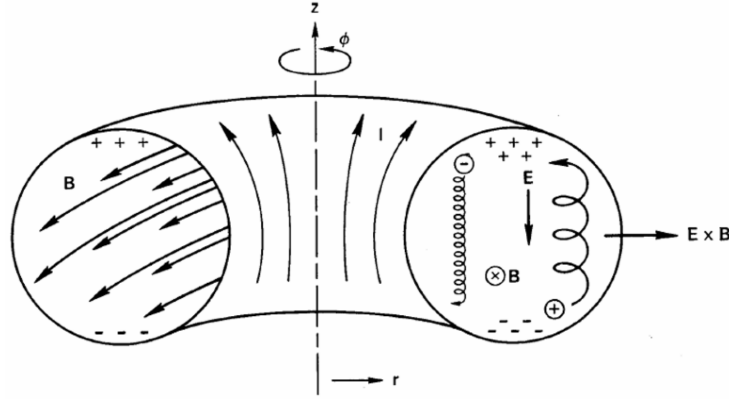
Figure 1.6: Demonstration of particle drift directions due to charge separation in reconnected donut-shaped solenoid Adopted from: F.F. Chen. *Introduction to Plasma Physics and Controlled Fusion.* Springer, 2016.

If a poloidal magnetic field component can be added to the toroidal magnetic field, helical magnetic field lines will be created, rotating in both the toroidal and poloidal directions. The ions drifting upwards will eventually move to the bottom along the helical magnetic field lines, so the charge separation is neutralized, vertical electric field can be avoided, and the outwards $E \times B$ drift is prevented. Generally two approaches exist for introduction of such poloidal field: through external and internal current. In tokamak devices internal currents in the toroidal direction inside the plasma give rise to a poloidal magnetic field.

1.3.3   Tokamak

Design that relies on induction of toroidal current in plasma for its confinement was originally introduced by Oleg Lavrentiev and further developed by Soviet physicists Andrei Sakharov and Igor Tamm in 1950s under a name ToKaMaK, which stands for an acronym in Russian signifying toroidal chamber with magnetic coils. Tokamak is the most promising fusion confinement configuration at the moment and the majority of MCF research is associated with the tokamak configuration. A schematics of such a machine is shown in a Fig. 1.7. The toroidal magnetic field coils are used to generate a strong toroidal magnetic field. The pulsed current through the central solenoid generates an electric field in the toroidal direction which breaks down the gas in the chamber and induces a current in the toroidal direction which gives rise to a poloidal magnetic field. The combination of the toroidal and poloidal magnetic field produces the desired helical magnetic field lines. The current heats the plasma through ohmic heating. Additional sets of coils are shown as well (poloidal, vertical field). These serve a purpose to provide control over plasma shape and position respectively.

Figure 1.8 shows possible cross-sections of tokamak plasma. Plasma fills almost the whole volume of the vacuum vessel of the tokamak. Cooling of plasma is inevitable due to interactions between the plasma and
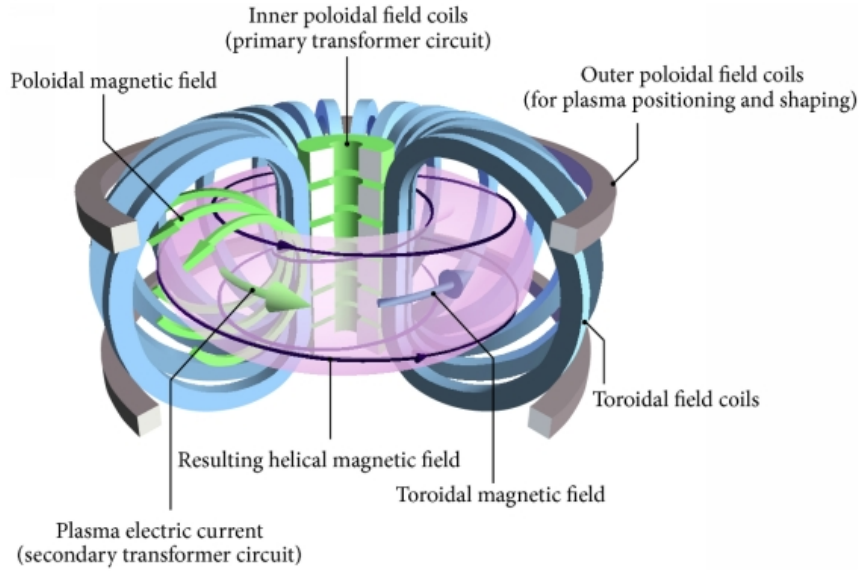
Figure 1.7: Basic tokamak schematic, demonstrating main components and magnetic field lines. Adopted from: Z. Ren S. Li, H. Jiang and C. Xu. Optimal tracking for a divergent-type parabolic pde system in current profile control. *Abstract and Applied Analysis*, 2014, 2014.

the walls and additional radiational losses. When the impurities adsorbed on the inner surface of the wall and the wall materials are sputtered off by plasma particles at high energy and enter the plasma, radiation loss is enhanced due to the high-Z nuclei in the plasma. In order to minimise plasma-wall interaction, limiters and divertors are used. Limiter is a heat resistant diaphragm or plate intercepting magnetic field lines. Magnetic flux surface that approaches but does not cross the limiter is called the last closed flux surface (LCFS). Using this surface plasma can be separated into two regions. 'Core' plasma lies within LCFS and flows freely along field lines. Scrape-off layer (SOL) is the region between LCFS and the wall of the vacuum vessel. In contrast, the plasma in SOL can not flow freely along field lines, as it will eventually encounter the limiter or the chamber wall. The SOL region acts like a buffer zone between the hot plasma and the walls of the chamber. Due to active interaction with walls and lack of direct heating the plasma temperature in SOL is significantly lower in comparison to the 'core' plasma. A more sophisticated way to prevent plasma cooling and interaction with the wall utilizes a divertor. It creates specific distortion in the magnetic field, by running a current along one or more coils parallel to the plasma current near the chamber wall, to create a diverging (hence the name - divertor) magnetic field and to guide particles to the specially designed plates which can endure large heating power. The divertor configuration is found on the majority of modern machines. The STOR-M tokamak on which this research has conducted uses a a less sophisticated limiter.
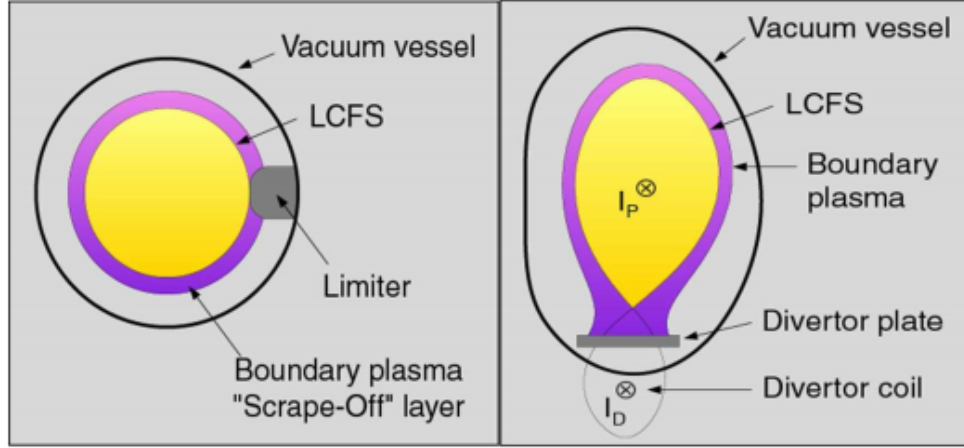
Figure 1.8: Schematics of poloidal cross-section of the limiter (left) and the divertor (right) tokamaks Adopted from: Martin Kocan. *Ion temperature measurements in the scrape-off layer of the Tore Supra tokamak.* PhD thesis, Université Henri Poincaré, 2009.

1.3.4 Fluctuations and instabilities in fusion plasma

A host of various types of waves and perturbations exists in such complex phenomena as plasma, causing rapid particle and energy transport. Abundant energy available from steep density and temperature gradients (unavoidable by the sole nature of confining device) in the fusion plasma serves as the source for instabilities and fluctuations around the equilibrium parameters (temperature, density, fields, etc.). Some instabilities are associated with magneto-hydro-dynamics (MHD) and arise whenever infinitesimal perturbation from an equilibrium state has a positive growth rate. Such instabilities have a large scale and are intricate result of interactions and perturbations within plasma and magnetic field. These instabilities can be understood from conditions of plasma equilibrium and are specific to particular confinement geometry. Additionally, another type of instabilities exists on the microscopic scale. They are mostly due to gyrokinetic effects which could not be described or predicted by MHD theory. Previously mentioned gradients can also 'drive' micro-instabilities, e.g. instabilities on scale size significantly smaller than size of the device and comparabable to gyro-radius. Those instabilities are observable as oscillations of plasma density, temperature (and pressure accordingly) and magnetic field on top of the equilibrium values and can develop to turbulent state with multiple time and spatial scales. Such turbulent state of plasma can enhance radial transport causing anomalous particle and energy losses and degradation of confinement beyond the classical Coulomb scattering theory. It is also possible that such fluctuations can grow in time and trigger large-scale MHD instabilities which may cause disruptions to terminate the tokamak discharge. This is an extremely undesirable event, leading to loss of confinement. When this happens energy from hot plasma is rapidly dissipated to the surrounding vessel which may damage the chamber wall. The sudden stop of the huge plasma current could induce tremendous electromagnetic forces on the conducting structure, damaging the entire device. Study of instabilities, fluctuations and their effects on plasma confinement is one of the priority research topics in MCF.

1.3.5 Diffusive transport

Previously discussed example of particle confinement via magnetic field, based on the so-called single particle model, did not include any effects associated with particle interactions, which lead to diffusion. The Neoclassical Transport Model is based on classical Coulomb scattering theories under toroidal geometry in tokamaks. This model can be used to predict diffusive particle, momentum and heat transport in the tokamak plasma. For example, the neoclassical transport model is able to predict such effect as bootstrap current. However, in most experiments the observed transport exceeds these predictions sometimes by orders of magnitude. This is due to the fact that this model is a classical theory and describes plasma in quiescent state, assuming various conditions, such as Maxwell's velocity distribution and equilibrium of plasma without considering the turbulent vortices in the plasma. Thus theory does not include any transport caused by fluctuations or gyrokinetic effects.

1.3.6 Anomalous transport

The observed difference between measured transport and model predictions is referred to as anomalous transport. It is generally assumed that such anomalous transport is non-diffusive in nature and is generated by turbulence vortexes driven by micro-instabilities. Plasma can potentially host a plethora of instabilities, being in state far from thermodynamic equilibrium, driven by steep pressure, temperature, density and current gradients. There is host of instabilities in tokamak plasma such as Ion and Electron Temperature Gradient (ITG, ETG), Trapped Electron Modes (TEM). These turbulent instabilities have been widely observed in experiments and numerical simulations. However, there is no turbulence theory based on the first principle of physics.

1.3.7 High confinement mode

Despite the significant progress in approach to Lawson criterion, discovered phenomenon of "power degradation" became one of the main issues in further development of MCF technology. This phenomenon describes non-linear growth in radial heat transport with applied power of auxiliary heating. However it was discovered in 1984 during experiments on ASDEX tokamak that, if sufficient energy was transferred to plasma, the plasma parameters were suddenly improved [13]. This mode of operation is referred to as High-confinement mode, or simply H-mode, in contrast to ordinary Low-confinement. In this regime density, temperature and, consequently, pressure increase and their radial profile appears to have a local steep region, forming a pedestal at some specific minor radius as shown in Fig. 1.9. This effect is associated with creation of transport barriers in the plasma [14], [15]. Ohmic H-mode can also be induced by electrode biasing driving a radial current, $\mathbf{j}_r$, that creates a shear in electric field and thus a shear in the $\mathbf{E} \times \mathbf{B}$ flow. Sheared poloidal flow layer breaks the large turbulent eddies and reduces the equivalent characteristic radial transport step length, leading to a transport barrier. External momentum input, may also generate such sheared flow.
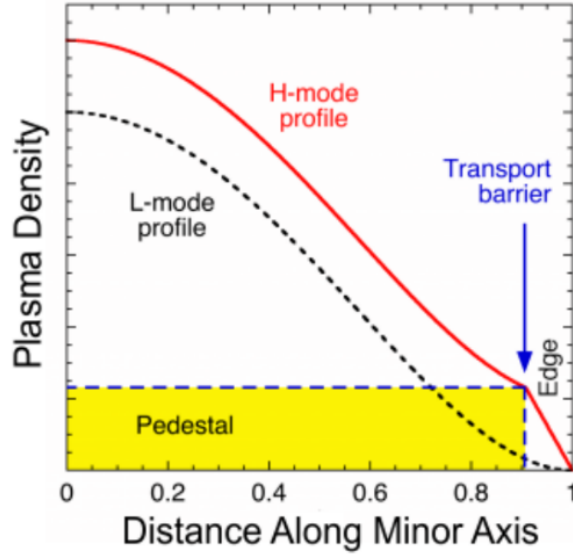
Figure 1.9: Illustration of difference in radial density profiles between regular (L-mode) and H-mode ('pedestal' effect) Adopted from: Boudewijn van Milligen. Sketch of h-mode profile and pedestal. `http://fusionwiki.ciemat.es/wiki/File:H-mode.png`. Accessed: 2019-09-30.

1.4 Diagnostics

To study plasma experimentally, and obtain all the important details about its behaviour, it is necessary to develop tools to measure its parameters and theoretical models to explain and predict experimental results. The techniques used to measure plasma parameters are commonly referred to as plasma diagnostics. Various properties in plasma such as refractive index, magnetic and electric fields, particle fluxes, radiation emission and scattering are utilized to measure plasma parameters [17], [18]. Hostile environment of the fusion plasma puts stringent limitations on diagnostic tools. High temperature, transient/intermittent events and small-size structures along with complexity of the studied phenomena sometimes limit applicability of certain methods. Several diagnostic tools were simultaneously utilized in this project to study fluctuations in the plasma edge region of the STOR-M tokamak.

Historically, one of the first diagnostic techniques applied to plasma were material probes, commonly referred to as Langmuir probes in honor of the scientist who pioneered their application. Despite it's simplicity, Langmuir probe is a very useful tool to measure particle flux under different bias voltage with respect to the plasma, allowing determination of a host of spatially resolved parameters such as electron density, temperature, floating and plasma potentials. However, these measurements introduce disturbance to the plasma and are applicable mostly to low temperature plasma due to material limitations. In fusion plasma in particular, application of material probes, such as the Langmuir probe, is limited to the edge regions to avoid damage of the probe with excessive heat fluxes and to prevent sputtering of the probe material. The location has to be well-thought out and probe materials chosen accordingly. These types of probes, sometimes arranged

12

in arrays are used to investigate plasma behavior in the vicinity of LCFS and in SOL. There is a need as well for non-intrusive diagnostic tools that could provide information about core plasma, as it is inaccessible by material probes. Usually neutral and ion beams, spectroscopy and refractive index measurements are utilized for that purpose. As it will be shown later for refractive index measurements, either microwave or optical EM-sources can be used, depending on expected levels of plasma density. Generally, active microwave diagnostics, which include interferometry and reflectometry, are used in tokamaks to determine refractive properties of plasma related to electron density and it's fluctuations [19]. Interferometry is a widely used tool in tokamaks for line-averaged density measurements and density profile reconstruction [20]. Reflectometry is used for density profile reconstruction and additionally allows for time and spatial resolved observations of plasma density fluctuations [21], [22].

The magnetic probes are simple magnetic flux pick-up coils which can be inserted into the plasma or placed outside of the plasma vessel. An array of coils, sometimes called Mirnov coils, named after the inventor, can be used to measure fluctuations of the poloidal magnetic field associated with the MHD activity. Properties such as its spatial configuration and rotational speed can be extracted. In conjunction with other diagnostics, such as the Langmuir probes or reflectometer, the Mirnov coil array allows investigation of connection between the MHD activity in plasma and density fluctuations in edge region.

1.5   Thesis motivation and objectives

Various experiments on STOR-M are conducted or planned to study the transition to high confinement mode through plasma biasing, resonant magnetic perturbations and momentum injection via compact torus. Observation of processes occurring at the edge plasma is important for better understanding of H-mode transition. The focus of this research is on development and implementation of a triple Langmuir probe (TLP) assembly to conduct time-resolved measurement of equilibrium (average) and fluctuating plasma parameters, particularly the density fluctuations. The measured results will be compared with the density fluctuations captured with a microwave reflectometer and also with the magnetic fluctuations recorded with a Mirnov coils array. Those fluctuating quantities originate at different locations and could be of different physics nature. Thus it is important to verify if the observed fluctuations are global or local and what their possible origin is. In addition, refined density evolution reconstruction based on the interferometer measurement is needed to resolve miscounting problems associated with an existing hardware-based phase fringe counter electronics.

Following tasks for this thesis work were set:

1. Design of the power supply circuit for triple Langmuir probe assembly along with its installation.

2. Development of programs for numerical processing of signals from diagnostic tools and their interpretation.

3. Series of experiments combining reflectometry, TLP, and Mirnov coil arrays in order to investigate properties of signals and correlations between different diagnostics.

1.6   Thesis outline

Following this introduction chapter, the second chapter will cover basic theoretical background, including treatment of electromagnetic wave propagation in continuous medium and in plasma. Sheath theory is discussed and probe data analysis theory and data interpretation is explained. Diagnostic techniques for plasma magnetic field fluctuations and MHD activities are then introduced.

The third chapter describes measurement methods and gives a brief overview of data analysis algorithms that were used in this work and their implementation.

The fourth chapter presents an experimental setup of STOR-M tokamak, its main parameters, description of utilized diagnostic tools and their arrangement and other experimental considerations.

The fifth chapter presents the experimental results and discussion.

The sixth chapter summarizes the major findings of this thesis work and suggests future research.

The Appendix describes a possible approach to estimation of density profile from the reflectometer signals at cut-off density during the STOR-M start-up phase.

Chapter 2

Theoretical background

This chapter will give an introduction to an environment of fusion plasma and a brief overview of underlying theory relevant to plasma diagnostic tools used in this thesis. First section will discuss particle fluxes in plasma, along with basics of sheath theory and its particular application to Langmuir probes. Second section deals with EM wave propagation through plasma, plasma conductivity and wave propagation in plasma. Lastly typical MHD activities in tokamak plasma will be briefly discussed and its classification will be presented.

2.1   Model of tokamak plasma

Prior to discussion of certain phenomena in plasma, it is useful to make and verify several simplifications which shall aid further analysis. A characterization of tokamak plasma should be given. Plasma of tokamak discharge is mostly 'collisionless'. This happens due to the relatively high temperature of plasma leading to almost full ionization of particles in the core region. This is true for the bulk of the plasma, however plasma in the outermost region of SOL will usually deviate from that. As it has already been discussed, in order to provide confinement, plasma is subject to a strong external magnetic field. Tokamak is magnetized, since the gyrofrequincies of particles are significantly higher than the inverse of the confinement time. For tokamaks, Larmour radius of ions (which is significantly larger than one of electrons) is of order of millimeters or sub-millimeters which is significantly smaller than the size of the device. Thus, plasma in tokamak is magnetized, and the presence and effects of the magnetic field have to be taken into account.

2.2   Particle fluxes

Electrostatic probes are used to measure charged particle fluxes on biased electrodes submerged into plasma, by investigating relations between applied voltages and currents in them. This is an intrusive method which distorts plasma, as it is affected locally by introduced electrodes, currents and fields that it creates. Despite the attractive simplicity of measurements, interpretation is not trivial. It is necessary to understand exactly how presence of the probe modifies plasma parameters locally and how measured values are related to unperturbed plasma parameters far away from the probe. In order to extract that information from these potential measurements and I-V (current-voltage) curves it is necessary to use an appropriate theoretical

model for particle fluxes within the vicinity of the probe and its relation to unperturbed parameters. This section will cover the approach usually taken and necessary assumptions.

2.2.1 Distribution function

Charged particle fluxes, and thus current densities and currents, are determined by charges arriving at the probe. It is almost impossible and, moreover unnecessary, to try to follow trajectories of all individual particles. As these currents consist of significantly large number of charge carriers, it is reasonable to use statistical approach by using velocity distribution function $f_\alpha = f_\alpha(t, \mathbf{x}, \mathbf{v})$ (VDF). $f_\alpha(t, \mathbf{x}, \mathbf{v})d^3\mathbf{x}d^3\mathbf{v}$ defines probability of finding particles of type α at time t within a volume of $d^3\mathbf{x}$ at location $\mathbf{x}$ and velocity volume of $d^3\mathbf{v}$ near $\mathbf{v}$. Generally, determination of VDF over time and space yields *all* the information about plasma, however it is a very ambitious goal. Some diagnostic tools, at best, can determine its local value over a certain period of time. However, it is possible to determine several most important quantities related to VDF f - its moments. For the homogeneous and constant in time VDF, the kth moment is defined as:

$$\mathbf{M}^k = \int (\mathbf{v})^k f(\mathbf{v}) d^3\mathbf{v} \tag{2.1}$$

where in general $\mathbf{M}$ is a tensor of kth order. For example, substitution for 0-th order yields:

$$\mathbf{M}^0 = \int (\mathbf{v})^0 f(\mathbf{v}) d^3\mathbf{v} = n \tag{2.2}$$

where n is density. Particle flux will be the result of taking the first moment:

$$\mathbf{M}^1 = \int (\mathbf{v})^1 f(\mathbf{v}) d^3\mathbf{v} = n\bar{\mathbf{v}} = \mathbf{\Gamma} \tag{2.3}$$

where $\bar{\mathbf{v}}$ stands for mean particle velocity. The second order moment is usually written in a following form:

$$m(\mathbf{M}^2 - n\bar{\mathbf{v}}\bar{\mathbf{v}}) = m \int (\mathbf{v} - \bar{\mathbf{v}})(\mathbf{v} - \bar{\mathbf{v}}) f(\mathbf{v}) d^3\mathbf{v} = \mathbf{p} \tag{2.4}$$

resulting in a pressure tensor $\mathbf{p}$. Following from its symmetry, there exists a coordinate system where this tensor can be expressed in a diagonal form:

$$\mathbf{p} = \begin{bmatrix} p_\perp & 0 & 0 \\ 0 & p_\perp & 0 \\ 0 & 0 & p_\parallel \end{bmatrix} \tag{2.5}$$

For the isotropic VDF this tensor turns to scalar, $p_\perp = p_\parallel = p$. In this case, the temperature can be defined in units of energy:

$$T = p/n \tag{2.6}$$

16

For the non-isotropic cases the perpendicular and parallel temperatures, $T_\perp$, $T_\parallel$, can be defined accordingly. For arbitrary VDF these equations provide effective temperature. In the particular case of Maxwellian distribution, VDF will yield "classical" temperature. Where Maxwellian VDF (MVDF) in isotropic, homogeneous media is defined as follows:

$$f(\mathbf{v}) = n \left(\frac{m}{2\pi kT} \right)^{\frac{3}{2}} \exp \left(-\frac{m}{2kT} (v_x^2 + v_y^2 + v_z^2) \right) \tag{2.7}$$

All of the moments of VDF , $k = 0$ to ∞, can be defined. However even the lower order moments are sufficient to provide reasonable approximations. To describe a system using only lower order moments it is sometimes necessary to limit variability of f by assuming that it is a known distribution. Most frequently Maxwellian VDF is used as de-facto in derivations, e.g. the system is considered to be in thermal equilibrium. Even in cases when this condition is not verified or strictly satisfied, such approach allows to extract approximate values, however the error in result will increase with increasing difference between real VDF and assumed Maxwellian VDF. This makes interpretation of results problematic at times, especially when absolute values of moments are in question, but the situation can be improved by incorporation of experimental VDF data measured by means of other diagnostics.

2.2.2 Particle fluxes and sheath formation

VDF allows to statistically determine particle fluxes on the probe. For the plasma that consists of 2 species, electrons and ions, the current density can be determined by summation of electron and ion current densities:

$$\mathbf{j} = \mathbf{j}_i + \mathbf{j}_e = Zn_i e\bar{\mathbf{v}}_i - n_e e\bar{\mathbf{v}}_e \approx n_e e(\bar{\mathbf{v}}_i - \bar{\mathbf{v}}_e) \tag{2.8}$$

The RHS of Eq. (2.8) is written under assumption of quasi-neutrality condition, $n_e \approx Zn_i$, where Z is the charge of ion. By integrating the velocity component projected the to normal of a flat unit surface area over VDF the particle flux through it from one side can be found in homogeneous isotropic medium:

$$\Gamma = \int \cos\theta(\mathbf{v})^1 f(\mathbf{v}) d^3\mathbf{v} = \frac{1}{4} n\bar{\mathbf{v}} \tag{2.9}$$

where θ is an angle between normal and velocity vectors and $\bar{\mathbf{v}}$ is the mean particle velocity.

When a probe is submerged into a plasma and the potential of the probe is kept the same as that of surrounding plasma, $V = V_p$, There are no perturbations to the motions of electrons or ions. For comparable electron and ion temperatures and even in case of thermal equilibrium between them, $T_e = T_i$, the electron thermal velocity will be significantly higher than one of ions:

$$\frac{\bar{v}_e}{\bar{v}_i} = \left(\frac{T_e m_i}{T_i m_e} \right)^{\frac{1}{2}} \approx \left(\frac{m_i}{m_e} \right)^{\frac{1}{2}} \gg 1 \tag{2.10}$$

which allows to express particle and current flux densities by rewriting Eq. (2.8) approximately, using $\bar{v}_e \gg \bar{v}_i$:

$$\mathbf{J} \approx ne(\bar{\mathbf{v}}_i - \bar{\mathbf{v}}_e) \approx -\frac{1}{4}ne\bar{\mathbf{v}}_e \qquad (2.11)$$

So the current flowing into the probe with surface area, A, can be expressed:

$$I = -\frac{1}{4}ne\int \mathbf{n}_A \cdot \bar{\mathbf{v}}_e dA \approx -\frac{1}{4}neA\bar{v}_e \qquad (2.12)$$

where $\mathbf{n}_A$ is the unit normal vector of the probe surface. This current is referred to as electron saturation current, I_{es}. In this regime all the electrons in surrounding plasma that arrive to the probe are collected, and low energy ions are repelled. If probe potential is lower than plasma potential, $V < V_p$, then only electrons, that have sufficient energy to overcome potential barrier, $\delta V = V_p - V$, are collected. When probe potential is decreased below a certain level, $V \ll V_p$, all electrons are reflected and the probe collects only ions, this regime is known as ion saturation current, I_{is}. It is worth noticing that the ion saturation current is not related to flux of ions with thermal velocity, $I_{is} \neq \frac{1}{4}neAv_i$. When the probe is floated (e.g., no drain is provided for charges) it will initially collect mostly electrons, due to their higher thermal velocity, however that will cause negative charge accumulation, leading to creation of a negative electric field, thus reducing flux of electrons and increasing flux of ions. Potential that probe will take under such zero net current conditions is named "floating" potential, V_f. The collected probe current as a function of voltage, usually referred to as characteristic I-V curve, is illustrated in Fig. 2.1.

However, this only provides qualitative understanding, but not quantitative information about connection between the I-V curve features and plasma parameters. In order to understand how insertion of a biased probe modifies plasma, perturbation of potential should be considered. In plasma potential is screened due to mobility of electrons. For example if potential of a point charge in vacuum is inversely proportional to distance, $\phi_{vacuum}(r) \propto \frac{1}{r}$, in plasma it will decay exponentially, $\phi_{plasma}(r) \propto e^{-\frac{r}{\lambda_D}}$, with a characteristic scale of Debye's length, λ_D :

$$\lambda_D = \sqrt{\frac{\epsilon_0 kT_e T_i}{e^2 n(T_e + T_i)}} \qquad (2.13)$$

However, because probes cannot be operated in core plasma, and can only be employed in edge region, where ion temperature is usually lower than one of electrons, Eq. (2.13) can be simplified, by ignoring T_i term:

$$\lambda_D \approx \sqrt{\frac{\epsilon_0 kT_e}{e^2 n}} \qquad (2.14)$$

Placing negatively (relative to plasma potential, V_p) biased probe of potential V_0 into plasma will cause formation of the so-called sheath, a region within which perturbations to potential are noticeable. Sheath thickness is on order of several Debye's length, $x_s \approx 5\lambda_D$. Unperturbed plasma parameters at a distance from a probe will be denoted with subscript ∞, for example unperturbed density n_∞. Outside sheath potential
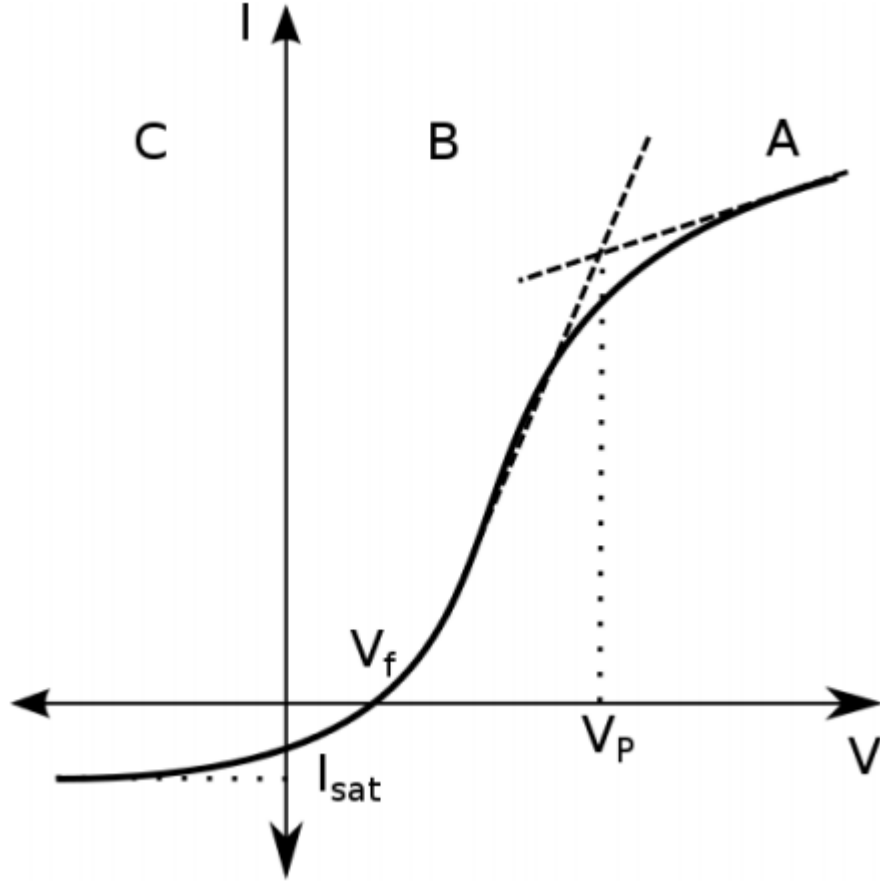
Figure 2.1: Current through Langmuir probe as a function of biasing voltage. Region A - electron saturation current; region B - ions and electrons are collected; region C - ion saturation current.

approaches plasma potential. One dimensional representation is presented in Fig. 2.2.

For this case potential can be obtained by solving Poisson's equation:

$$\nabla^2 V(x) = -\frac{\rho}{\epsilon_0} = -\frac{e}{\epsilon_0}(n_i - n_e) \tag{2.15}$$

Which requires knowledge of ion and electron densities, n_i, n_e. Ion current can be derived under the assumption of negligible ion velocity outside the sheath (cold ions), therefore conservation of energy yields:

$$|v_i| = \sqrt{\frac{-2eV}{m_i}} \tag{2.16}$$

Further, it is necessary to make an assumption regarding the effects of collisions. Generally effects of collisions might be neglected if the mean free path, l, for the particle collisions is significantly larger than the sheath thickness:

$$l \gg x_s \tag{2.17}$$
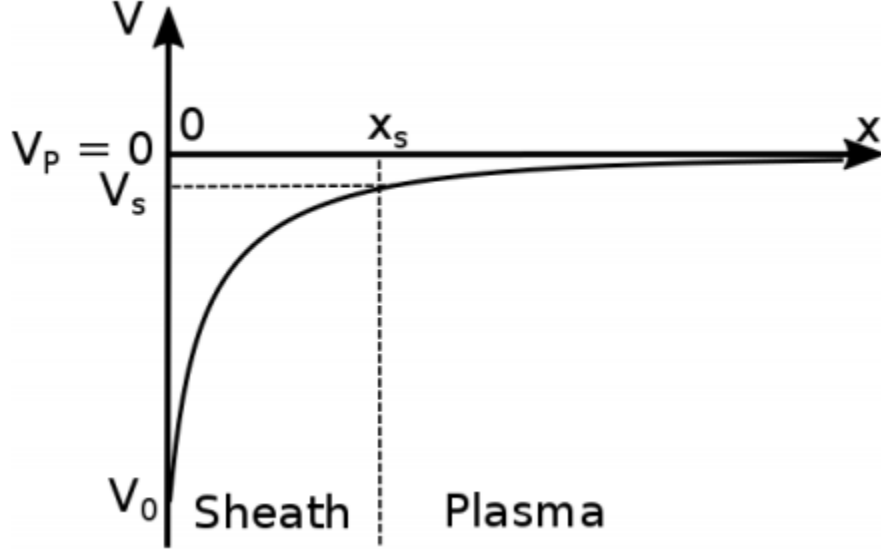
Figure 2.2: One dimensional representation of sheath in plasma.

In fusion experiments plasma is almost fully ionized and Coulomb collisions dominate. The mean free path for Coulomb collisions can be roughly estimated in units of Debye's length:

$$l_c \approx (n\lambda_D^3)\lambda_D \tag{2.18}$$

So, condition 2.17 is satisfied, and collisions may be omitted in further derivation. In that case, almost all the ions that enter the sheath are collected. Resulting in ion flux:

$$\Gamma_i = S(x)n_i v_i \tag{2.19}$$

where $S(x)$ is a fixed surface area around the probe within sheath at $(x < x_s)$. This allows to express ion density:

$$n_i(x) = \sqrt{\frac{m_i}{-2eV(x)}}\frac{\Gamma_i}{S(x)} \tag{2.20}$$

Because of negative potential of the probe, most of the electrons are repelled, and only those, with velocity higher than v_c can overcome potential of the probe and are collected:

$$v > v_c = \sqrt{\frac{2e}{T_e}(V(x) - V_0)} \tag{2.21}$$

20

Assuming Maxwellian VDF for electrons at infinity, the VDF at position x from the probe surface will be:

$$f(x,v) = \begin{cases} \sqrt{\dfrac{m_e}{2\pi Te}} n_\infty e^{\left(-m_e v^2/2 + eV(x)\right)/T_e} & v \leq v_c \\ 0 & v > v_c \end{cases} \tag{2.22}$$

After integration the electron density at the position x is obtained:

$$n_e = n_\infty e^{eV(x)/T_e} 0.5 \left(1 + erf\left[\sqrt{\{V(x) - V_0\}e/T_e}\right]\right) \tag{2.23}$$

where $erf(x)$ is error function:

$$erf(x) = \frac{2}{\sqrt{\pi}} \int_0^x e^{-t^2} dt \tag{2.24}$$

However, if biasing potential, V_0, is sufficiently low, in order to assume that all of the electrons repelled, the above equation can be approximated:

$$n_e \approx n_\infty e^{eV(x)/T_e} \tag{2.25}$$

Substituting Eqs. (2.25), (2.20) into Poisson Eq. (2.15) yields:

$$\nabla^2 V(x) = -\frac{e}{\epsilon_0}\left(\sqrt{\frac{m_i}{-2eV(x)}}\frac{\Gamma_i}{S(x)} - n_\infty e^{eV(x)/T_e}\right) \tag{2.26}$$

In a particular case when sheath thickness is significantly smaller than the probe dimensions, i.e., $x_s \ll a$, the curvature effects of the probe can be neglected and results obtained from 1D model can be effectively used. Effective collecting surface, $S(x)$ can be taken constant at x_s. Quasi-neutrality at plasma-sheath transition location, $n_i(x_s) = n_e(x_s)$, imposes a condition, $V_s = -T_e/e$ in order for Eq. (2.26) to have an exponentially decaying solution, thus forming a sheath. Expression for ion saturation current can be now evaluated at x_s:

$$I_{is} = -e^{-1/2}eS(x_s)n_\infty\sqrt{\frac{T_e}{m_i}} \tag{2.27}$$

where $\sqrt{\dfrac{T_e}{m_i}}$ stands for Bohm's velocity, sometimes also called ion sound velocity.

2.2.3 Effects of presence of magnetic field

As it has been already mentioned, the magnetic field restricts motion of a charged particle in two dimensions, while movement along the magnetic field is unaffected. Particles rotate in a plane perpendicular to magnetic field line with Larmor radius:

$$r_L = \frac{mv_\perp}{eB} \approx \frac{1}{eB}\sqrt{mkT} \tag{2.28}$$

As the Larmor radius for electrons is significantly smaller than that of ions, $r_{Le} \approx \sqrt{\dfrac{m_e}{m_i}}r_{Li}$, electrons are affected more than ions. In most fusion experiments the effective collection surface of the probe to its

21

projection to the plane perpendicular to the field lines. However it is insufficient to prevent electrons from setting up Boltzmann density distribution around the probe due to their unrestricted mobility along the field lines. Thus, electrons are considered fully 'magnetized' and the resulting effect will vary with behaviour of ions depending on the magnitude of the magnetic field. Generally the problem is complex as motion of ions has to be solved relative to the shape of the probe. Nevertheless, two limiting cases significantly simplify the treatment. If the ion Larmor radius is considerably larger than the characteristic scale, a, of probe (usually, probes largest dimension), than the ions are assumed 'unmagnetized', as on the scale of the sheath thickness and probe geometry, their motion is barely affected. Allowing applicability of all previously discussed treatment. If the opposite is true and ion Larmor radius is significantly smaller than probe scale length, $r_{Li} \ll a$, the ion motion along the magnetic flux tube is considered as collisionless and diffusion of ions across the magnetic field has to be considered. In this case, similarly to magnetized electrons, effective collective area has to be adjusted, and the scaling factor for ion saturation current is slightly changed.

2.3 Refractive index of plasma

Plasma parameters affect EM wave propagation in plasma. This is exploited in various forms in diagnostic tools such as reflectometry and interferometry. Before attempting to cover wave propagation in inhomogeneous plasma, a simpler case of homogenous medium will be discussed first.

2.3.1 EM-waves in homogeneous medium

Starting with Maxwell's equations in vacuum:

$$\boldsymbol{\nabla} \times \mathbf{E} = -\frac{d\mathbf{B}}{dt} \tag{2.29}$$

$$\boldsymbol{\nabla} \times \mathbf{B} = \mu_0 \mathbf{j} + \epsilon_0 \mu_0 \frac{d\mathbf{E}}{dt}$$

and assuming harmonic solutions in the form:

$$A(x,t) = A(k,\omega) = A_0 e^{i(\mathbf{k} \cdot \mathbf{x} - \omega t)} \tag{2.30}$$

$$\boldsymbol{\nabla} \to i\mathbf{k}$$

$$\frac{d}{dt} \to -i\omega$$

following wave equation can be obtained:

$$\mathbf{k} \times (\mathbf{k} \times \mathbf{E}) + i\omega(\mu_0 \boldsymbol{\sigma} \cdot \mathbf{E} - i\epsilon_0 \mu_0 \omega \mathbf{E}) \tag{2.31}$$

which can be further converted to a secular equation system for the electric field:

$$(\mathbf{k}\mathbf{k} - k^2\mathbf{I} + \frac{\omega^2}{\epsilon_0\mu_0}\boldsymbol{\epsilon}) \cdot \mathbf{E} \tag{2.32}$$

where $\mathbf{I}$ is the unit tensor and the electric permittivity tensor, $\boldsymbol{\epsilon}$, is a function of the conductivity tensor $\boldsymbol{\sigma}$:

$$\boldsymbol{\epsilon} = \mathbf{I} + \frac{i}{\omega\epsilon_0}\boldsymbol{\sigma} \tag{2.33}$$

For $\boldsymbol{E}$ to have non trivial solution it is necessary for the determinant of matrix in the brackets to vanish:

$$det \left(\mathbf{k}\mathbf{k} - k^2\mathbf{I} + \frac{\omega^2}{\epsilon_0\mu_0}\boldsymbol{\epsilon}\right) = 0 \tag{2.34}$$

By solving the above equation it is possible to obtain the dispersion relation:

$$k = k(\omega) \tag{2.35}$$

For isotropic case $\boldsymbol{\sigma} = \sigma\mathbf{I}$ and for a wave propagating along $\mathbf{z}$ direction:

$$det\ (\mathbf{k}\ \mathbf{k} - k^2\mathbf{I} + \frac{\omega^2}{\epsilon_0\mu_0}\boldsymbol{\epsilon}) = det \begin{bmatrix} -k^2 + \dfrac{\omega^2\epsilon}{\epsilon_0\mu_0} & 0 & 0 \\ 0 & -k^2 + \dfrac{\omega^2\epsilon}{\epsilon_0\mu_0} & 0 \\ 0 & 0 & \dfrac{\omega^2\epsilon}{\epsilon_0\mu_0} \end{bmatrix} \tag{2.36}$$

Which gives following solutions along $\mathbf{x}, \mathbf{y}, \mathbf{z}$:

$$(-k^2 + \frac{\omega^2\epsilon}{\epsilon_0\mu_0})E_x = 0 \tag{2.37}$$

$$(-k^2 + \frac{\omega^2\epsilon}{\epsilon_0\mu_0})E_y = 0$$

$$(\frac{\omega^2\epsilon}{\epsilon_0\mu_0})E_z = 0$$

So, it can be seen that there can be two different modes: transverse and longitudinal with according dispersion relations:

$$k^2 = \frac{\omega^2\epsilon}{\epsilon_0\mu_0} \tag{2.38}$$

$$\frac{\omega^2\epsilon}{\epsilon_0\mu_0} = 0 \tag{2.39}$$

23

The transverse EM-waves are of main interest. The phase velocity for such waves follows:

$$v = \frac{\omega}{k} \tag{2.40}$$

$$v_{vacuum} = \frac{\omega_0}{k_0} = c \tag{2.41}$$

Refractive index is defined as relation of speed of light, v, of the wave in the medium to the speed of light in vacuum, c:

$$N = \frac{v}{c} = \frac{\omega}{kc} = \sqrt{\epsilon} \tag{2.42}$$

So it is necessary to investigate how refractive index depends on plasma properties.

2.3.2 Microwave conductivity of the collisionless plasma

The previously obtained results are applicable to any uniform linear medium in which EM waves may propagate. It is conductivity, $\boldsymbol{\sigma}(k, w)$, or, equivalently, dielectric permittivity, $\boldsymbol{\epsilon}(k, w)$, of the media that define its refractive index. As phase velocity of EM waves in question is significantly higher than thermal velocities of electrons, the so-called "cold" plasma approximation can be utilized, which will ignore thermal motion of the particles. And because of the high frequency of the waves ion motion can be ignored due to its high inertia. It is electrons that play a dominant role in plasma conductivity at high frequencies. Equation of motion of a single electron in plasma with static magnetic field, $\mathbf{B_0}$, can be written:

$$m_e \frac{\partial \mathbf{v}}{\partial t} = -e(\mathbf{E} + \mathbf{v} \times \mathbf{B_0}) \tag{2.43}$$

where the second order small term $(\mathbf{v} \cdot \boldsymbol{\nabla})\mathbf{v}$ and collisions are omitted. Than, by solving for $\mathbf{v}$ in terms of $\mathbf{E}$ and combining with the Ohm's law:

$$\mathbf{j} = -en_e\mathbf{v} = \boldsymbol{\sigma} \cdot \mathbf{E} \tag{2.44}$$

the expression for conductivity $\boldsymbol{\sigma}$, by choosing $\mathbf{B_0}$ along $\mathbf{z}$, can be obtained:

$$\boldsymbol{\sigma} = \frac{in_e e^2}{m_e \omega} \cdot \frac{1}{1 - \Omega^2/\omega^2} \begin{bmatrix} 1 & -i\Omega/\omega & 0 \\ 0 & 1 & 0 \\ i\Omega/\omega & 0 & 1 - \Omega^2/\omega^2 \end{bmatrix} \tag{2.45}$$

where $\Omega \equiv eB_0/m_e$ is the gyro-frequency of electrons.

2.3.3 EM-wave propagation in homogeneous plasma

Equation (2.45), in the simplest case of electromagnetic wave propagating through collisionless plasma in absence of magnetic field, simplifies to give a scalar plasma conductivity, ($\mathbf{j} = \sigma \mathbf{E}$):

$$\sigma = -i \frac{ne^2}{m\omega} \tag{2.46}$$

The timescale of plasma response to potential perturbation is determined by the plasma frequency ω_p which is given by:

$$\omega_p = \sqrt{\frac{ne^2}{m_e \epsilon_0}} \tag{2.47}$$

For numerical value it is straightforward to obtain:

$$f_p = \frac{\omega_p}{2\pi} = 8979 \sqrt{n[\text{cm}^{-3}]} \text{ [Hz]} \tag{2.48}$$

which yields frequencies in microwave range for typical laboratory plasmas. Then plasma permittivity ϵ can be expressed from Eqs. (2.46), (2.47):

$$\epsilon = 1 - i \frac{\sigma}{\epsilon_0 \omega} = 1 - \frac{ne^2}{\epsilon_0 m \omega^2} = 1 - \frac{\omega_p^2}{\omega^2} \tag{2.49}$$

which can be used to calculate reafractive index of the medium by substitution into Eq. (2.42):

$$N = \sqrt{\epsilon} = \sqrt{1 - \frac{\omega_p^2}{\omega^2}} \tag{2.50}$$

From Eq. (2.50) it can be concluded that EM wave of a certain frequency ω, depending on plasma density, n, may be either reflected from plasma ($\omega < \omega_p(n)$), or penetrate plasma ($\omega > \omega_p(n)$). It is common to define critical density n_c for a given frequency ω:

$$\omega = \sqrt{\frac{n_c e^2}{\epsilon_0 m}} \tag{2.51}$$

As it can be seen from Eq. (2.51), n_c defines the upper limit of plasma density where propagation of EM wave of frequency ω is possible. Locations, $\mathbf{x}_c$, in plasma where density of plasma is equal to the critical density, $n(\mathbf{x}_c) = n_c$, is referred to as cut-off layer, or reflection layer.

2.3.4 Magnetized collisionless plasma

Stationary magnetic field strongly affects motion of charge carriers and thus, conductivity of plasma, making it highly anisotropic. Refractive index, N, for EM-wave propagation in plasma in presence of the magnetic

field can be found by expressing dielectric tensor, $\boldsymbol{\epsilon}$, through conductivity tensor, $\boldsymbol{\sigma}$, defined in Eq. (2.45):

$$\boldsymbol{\epsilon} = \begin{bmatrix} 1 - \dfrac{\omega_p^2}{\omega^2 - \Omega^2} & \dfrac{i\omega_p^2\Omega}{\omega(\omega^2 - \Omega^2)} & 0 \\ -\dfrac{i\omega_p^2\Omega}{\omega(\omega^2 - \Omega^2)} & 1 - \dfrac{\omega_p^2}{\omega^2 - \Omega^2} & 0 \\ 0 & 0 & 1 - \dfrac{\omega_p^2}{\omega^2} \end{bmatrix} \tag{2.52}$$

then by substituting Eq. (2.52) to Eq. (2.36) and introducing the following abbreviations for dimensionless quantities [17]:

$$X = \frac{\omega_p^2}{\omega^2} \tag{2.53}$$

$$Y = \frac{\Omega}{\omega} = \frac{eB_0}{m\omega} \tag{2.54}$$

$$N = \frac{kc}{\omega} = \sqrt{\epsilon} \tag{2.55}$$

and choosing rectangular coordinate axes such that $k_x = 0$:

$$\mathbf{k} = k(0, \sin\theta, \cos\theta) \tag{2.56}$$

where θ is the angle between $\mathbf{k}$ and $\mathbf{B_0}$ in the $\boldsymbol{z}$ direction, the following dispersion relationship can be obtained:

$$N^2 = \epsilon = 1 - \frac{X(1 - X)}{1 - X - \dfrac{1}{2}Y^2\sin^2\theta \pm \left[\left(\dfrac{1}{2}Y^2\sin^2\theta\right)^2 + (1 - X)^2\,Y^2\cos^2\theta\right]^{1/2}} \tag{2.57}$$

This expression is known as the Appleton-Hartree formula for the refractive index. From the above equation the wave propagating perpendicular to the magnetic field lines $\theta = \pi/2$ is of our main interest, because this case is most commonly found in experiments with magnetically confined plasma, as microwave beam is launched from the side of the torus into the plasma. There are two distinct cases for which the expression considerably simplifies. In case when the polarization of the incident wave is parallel to magnetic field $\mathbf{E} \parallel \mathbf{B_0}$, the relation reduces to:

$$N^2 = 1 - X = 1 - \frac{\omega_p^2}{\omega^2} \tag{2.58}$$

Wave described by this dispersion relationship may seem familiar because it is identical to wave propagation in unmagnetized plasma and is usually referred as "Ordinary wave", or, sometimes, simply "O"-mode. It can be intuitively understood if one considers, that in this case high-frequency oscillations of electrons caused by the electric field of the wave are not affected by the magnetic field and so is the dispersion relation. For the

26

incident wave with polarization perpendicular to magnetic field $\mathbf{E} \perp \mathbf{B_0}$, relation can be written as:

$$N^2 = 1 - \frac{X(1-X)}{1-X-Y^2} \tag{2.59}$$

Wave described by this dispersion relationship is referred as "Extraordinary wave", or "X"-mode.

2.3.5 Wave propagation in non-uniform plasma

It is necessary to consider how wave will propagate in medium with spatial gradients in electromagnetic properties. Mathematically, the harmonic solution of the form $e^{i(\mathbf{k} \cdot \mathbf{x} - \omega t)}$ no longer separately satisfy Maxwell's Eq. (2.31). Yet solution can still be expressed with sum of such Fourier modes, but these will, in general, be coupled, with coupling provided by aforementioned nonuniformities of the medium. Example of such coupling is partial wave reflection in opposite direction of wave propagation when wave encounters density gradient along its direction of propagation. If properties of medium vary slow enough in space, then the electromagnetic properties are well defined locally, allowing to treat such propagation as in an approximately uniform medium, and hence, making previously obtained results valid. In 1923 Harold Jeffreys has developed and published such technique for a class of differential equations governing waves [23]. Three years later technique became widespread with its re-invention and application to Schrodinger's equation by Wentzel, Kramers and Brillouin [24], [25], [26]. Solving such wave-type equations in slowly varying medium is often referred as geometrical optics (WKBJ) approximation. For the propagation of the EM wave field for a given frequency is expressed in the form:

$$E \approx E_0 e^{i(\int \mathbf{k}(\mathbf{x},t) \cdot \mathbf{dl} - \omega t)} \tag{2.60}$$

Where l is the distance along the beam path and $\boldsymbol{k}$ is the local solution of the homogeneous plasma dispersion relation for the given ω. This approximation holds while fractional variation of $\boldsymbol{k}$ is small on the wavelength:

$$\frac{|\nabla_x k|}{k^2} \ll 1 \tag{2.61}$$

or, in terms of refractive index:

$$\frac{N}{|\nabla_x N|} \gg \lambda \tag{2.62}$$

which states that the refractive index measurements are applicable when the characteristic scale length of non-uniformity of medium properties is significantly larger than wavelength of probing microwave beam. When the condition of Eq. (2.62) is not satisfied it is necessary to solve the full set of Maxwell equations which are usually carried out via computer simulation. All further discussed calculations assume the applicability of WKBJ approximation, if not stated otherwise. When WKBJ is applicable, phase of the emerging wave given by $\int \mathbf{k} \cdot \mathbf{dl}$ can be expressed through refractive index as:

$$\int \mathbf{k} \cdot \mathbf{dl} = \int \frac{\omega}{c} N \, dl \tag{2.63}$$

For reflectometry, however, such approximation is not suitable, because condition $n \ll n_c$ could not be satisfied in the vicinity of the reflection layer. Nevertheless, under careful consideration the following equation for phase difference at position between incident and waves reflected from a uniform plasma slab with linearly growing plasma density under normal incidence was obtained by Ginzburg [27]:

$$\delta\phi = \frac{\omega}{c} \int_{x_c}^{a} \mu(x) \; dx - \pi/2 \tag{2.64}$$

where x_c is used to denote location of the layer with critical density and a is the location of the plasma boundary. The result indicates that reflection from plasma is very similar to reflection from a mirror (conducting surface with roughness scale significantly smaller than wavelength). Resulting phase will be identical to what can be calculated with a straightforward WKBJ approach, minding, however, inclusion of an additional phase of $\pi/2$.

2.4 Magnetic field fluctuations and MHD activity

The magnetic field configuration plays a critically important role in confinement of plasma. Charged particles are "guided" along the magnetic field lines. If the magnetic field is locally perturbed it can increase local transport, e.g., cause particle losses. Certain topology of nested magnetic flux tubes allows tokamak to confine plasma effectively. It is possible though that reconnections and separation of independent flux tubes within this structure can occur. These separated formations are called magnetic islands. Range of phenomena associated with interaction between plasma and magnetic field is vast, however this section will briefly provide information relevant to the understanding structure of the magnetic field, its perturbation and possible connection to various types of MHD-instabilities that can develop within plasma.

2.4.1 Flux freezing

Collisionless plasma, having high conductivity along the magnetic field lines, possesses an outstanding property - magnetic flux "freezing". Magnetic flux through any closed contour in plasma, moving with certain velocity is approximately conserved quantity. This result can be obtained, if magnetic flux, Φ, through a surface, $\mathbf{S}$, which is moving with the plasma:

$$\Phi = \int_{\mathbf{S}} \mathbf{B} \cdot d\mathbf{S} \tag{2.65}$$

Then, full derivative of 2.65 with respect to time is:

$$\frac{d\Phi}{dt} = - \int_{\mathbf{S}} \nabla \times (\mathbf{E} + \mathbf{V} \times \mathbf{B}) \cdot d\mathbf{S} \tag{2.66}$$

However, in case of ideal MHD (e.g. collisionless plasma) part of Eq. (2.66) brackets vanishes:

$$\mathbf{E} + \mathbf{V} \times \mathbf{B} = \rho \cdot \mathbf{J} \approx 0 \tag{2.67}$$

where $\rho \approx n_i m_i$ is plasma mass density. This implies that the magnetic field should move with plasma. In other words, field lines are "frozen" into the plasma. Though, one should remember, that such treatment of plasma is an approximation, which has limits to its application. For example this condition restricts any change in topology of magnetic field lines (such as reconnection) which is observable in real experiments. This happens due to large but finite conductivity of plasma. However, this property might be used for diagnostic purposes. Allowing to suggest that plasma movement on sufficiently fast timescales can be directly coupled and coincide with perturbation of the magnetic field, possibly indicating that magnetic flux surfaces might move together with layer of plasma and have certain similarity in their shape or structure.

2.4.2 Magnetic fluctuations

In plasma shaped in a torus, because of periodicity in poloidal and toroidal directions, field perturbation can be expressed as a sum of helical Fourier modes:

$$e^{i(m\theta + n\phi)} \tag{2.68}$$

where m and n are poloidal and toroidal mode numbers (integers) respectively. Their combinations can be visualized as helical distortion of plasma column, which are undesired. For particular case of $n = 0$ they represent radial equilibrium ($m = 0$), position ($m = 1$), and shape ($m \geq 2$) of plasma column. Different instability modes are presented in Fig. 2.4. If perturbation of such mode lies along the direction of the closed magnetic field somewhere within plasma, this mode is said to be resonant. If such mode will have nonzero component along the normal of equilibrium magnetic surfaces, it will cause change in field topology and formation of magnetic 'islands'. Magnetic islands are separated flux tubes that break the equilibrium plasma topology of inlaying magnetic surfaces. Figure 2.3 illustrates that deviation in topology in the poloidal cross-section of the plasma.

Direction of the field perturbation can be derived [17]:

$$\frac{\tilde{B}_\varphi}{\tilde{B}_\theta} = \frac{nr}{mR} \tag{2.69}$$

Which implies that the tangential field perturbation points parallel to helical coordinate $m\theta + n\varphi$. In devices like tokamaks, where m/n is typically of order 1 or larger, this causes perturbations to be predominantly in poloidal direction, $\tilde{B}_\theta$, as $r/R \ll 1$. These perturbations can be remotely compared to elongated ripples on the magnetic surface. Magnetic perturbations usually occur near the rational surface. The magnetic perturbation structure may propagate in torus, either rigidly tied to plasma motion or independent of it, in
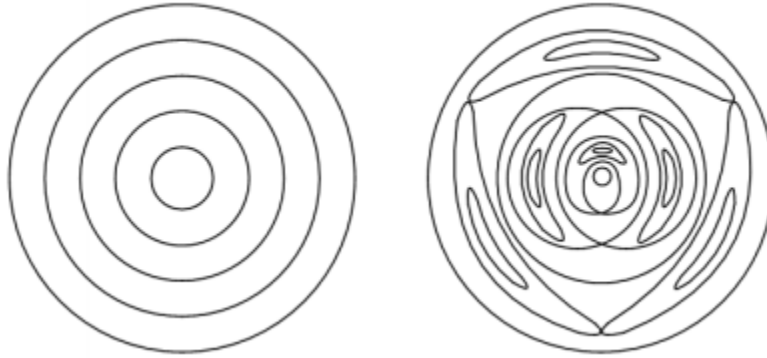
Figure 2.3: Poloidal cross-section of equilibrium plasma (left) and plasma with magnetic islands (right).

the form $e^{i(m\theta+n\phi-\omega t)}$ where ω is the oscilatory angular frequency for observation at a fixed location. For observation at fixed toroidal angle along the poloidal direction it will appear to be rotation of that rippled surface in the poloidal direction. Rational values of m/n on the other hand, can cause standing waves allowing amplification of these perturbations. Islands can cause significant particle and energy losses from core plasma, cooling it and degrading the confinement. Moreover, if the island grows big enough it can trigger instabilities in plasma and induce minor disruptions or even dangerous major disruption causing a total loss of confinement and an end of discharge.
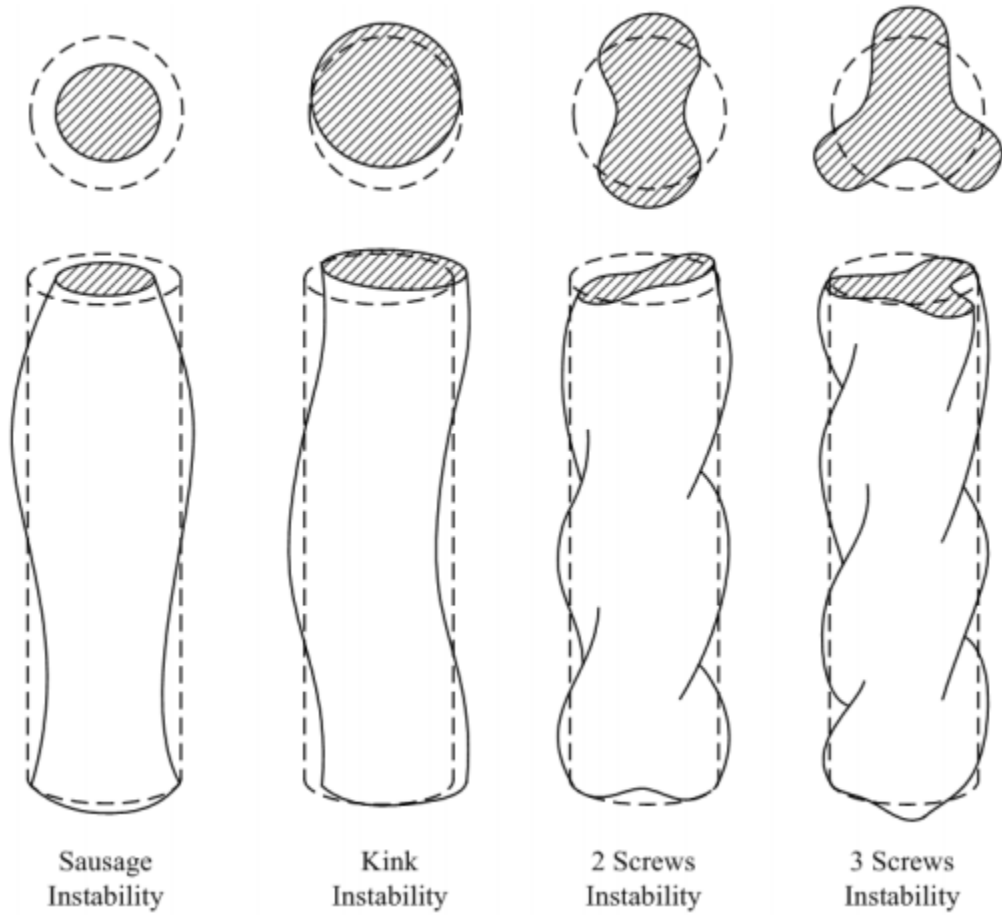
Figure 2.4: Poloidal modes with different mode numbers $m = 0, 1, 2, 3$ developed on a plasma column together with a cross-sectional view for each case.

Chapter 3

Measurement techniques and data analysis

Firstly, this chapter introduces general data analysis techniques that were used for processing of experimental data. Secondly measurement techniques and their interpretation of such diagnostics as microwave interferometry, reflectometry, Mirnov coils and Langmuir triple probe are reviewed. Thirdly certain algorithms that are utilized in phase counting for refractive index measurements and their numerical implementations are explained.

3.1 Data analysis techniques

Visual analysis is impractical for comparison of signals as it does not provide any metrics for quantitative comparison. Overview of analysis techniques will be given in this section to describe processing tools that were utilized in this work. Experimental data is recorded, stored and analyzed digitally, e.g., represented by discrete time series of samples recorded via analog-to-digital converter (ADC) from diagnostic outputs. To investigate features of fluctuating signals of different nature (from different diagnostic tools) time and frequency domain analysis were used, along with their combinations such as 2 dimensional time-frequency spectral diagrams (spectrograms).

3.1.1 Time domain analysis

Correlation between two (generally) complex time-domain signals, $x(t), y(t)$, is a measure describing their similarity as a function of time displacement, τ, of one relative to another. So that if some characteristic feature is observed in both signals, but at different moments in time (t_1 and t_2) unity cross-correlation will be observed at a time lag $\tau = t_2 - t_1$. Cross-correlation, R_{xy}, between two continuous functions, $x(t), y(t)$, can be calculated by following integral:

$$R_{xy}(\tau) = (x(t) \star y(t))(\tau) = E[x(t)y^*(t)] \equiv \int_{-\infty}^{\infty} x(t)y^*(t + \tau)dt \qquad (3.1)$$

where $y^*(t)$ stands for complex conjugate of $y(t)$ and $E[y(t)]$ denotes expectation value of $y(t)$ calculated from $t = 0$ to $t = T$ is defined below for continuous and discrete cases:

$$E[y(t)] = \int_{t=0}^{t=T} y(t)p(t)dt \tag{3.2}$$

$$E[y[t]] = \sum_{t=0}^{t=T} y[t]p[t] \tag{3.3}$$

where p is a statistical weight. Equations 3.2 reduces to the mean in case of equal unitary weights. Auto-correlation is a particular case of cross-correlation and is calculated by taking cross correlation with signal itself:

$$R_{xx}(\tau) = (x(t) \star x(t))(\tau) = \int_{-\infty}^{\infty} x^*(t)x(t+\tau)dt \tag{3.4}$$

Being closely related to correlation, covariance is used to analyze fluctuating components of signals by subtraction of mean values, μ_x, μ_y, from them:

$$K_{xy}(\tau) = E[(x(t) - \mu_x)(y(t) - \mu_y)^*] \tag{3.5}$$

Normalisation of covariance by standard deviation of signals, $\sigma_x\sigma_y$ yields unity-normalised Pearson correlation coefficient:

$$\rho_{xy}(\tau) = \frac{K_{xy}(\tau)}{\sigma_x\sigma_y} \tag{3.6}$$

where σ_x is a standard deviation of variable x defined as:

$$\sigma_x = \sqrt{E\left[x - E[x]\right]} \tag{3.7}$$

The normalisation of covariance ranges from $\rho_{xy} = 1$ for correlated signals to $\rho_{xy} = -1$ for anti-correlated signals.

Correlation is a useful tool in signal processing, utilized for detection and measurement of similarity between two time series. Additionally correlation can help to extract periodic fluctuations from noisy data. Auto-correlation of periodic function is periodic. If random noise is present, it will not have significant auto-correlation, thus will be filtered out. That allows to perform spectral analysis of noisy signals by applying it to auto-correlation of those signals instead of directly to the sampled data, increasing signal to noise ratio. Auto-correlation will always have its maximum value of one at a zero time lag, $R_{xx}(0) = 1$. For a finite length, real valued, discrete signals, $x[t], y[t]$, of length N, cross-correlation can be expressed as a sum:

$$R_{xy}[\tau] = (x[t] \star y[t])[\tau] \equiv \sum_{\tau=-N}^{N} x[t]y[t+\tau] \tag{3.8}$$

In real world applications correlation is not usually calculated over the whole length of the signal but instead

measured on a shorter span of time windows and sufficient lags to minimize computational cost.

3.1.2 Spectral analysis

In the majority of cases it is easier to investigate periodic signals in the frequency domain rather than in the time domain. Fourier transform (FT) is an integral transform that serves a fundamental role in modern physics, mathematics and, particularly in signal processing applications. Fourier transform is an integral transform decomposing a function into an infinite sum of harmonics, translating it between time and frequency domains. This transform allows representation of aperiodic function as an integral sum of periodic functions. For a real valued, continuous time domain signal, $x(t)$, its frequency space representation, $X(f)$ is defined below:

$$X(f) \equiv \int_{-\infty}^{\infty} x(t)e^{-i2\pi ft}dt \tag{3.9}$$

or, equivalently, using cyclical frequency, $\omega = 2\pi f$ and minding normalization:

$$X(\omega) \equiv \frac{1}{\sqrt{2\pi}} \int_{-\infty}^{\infty} x(t)e^{-i\omega t}dt \tag{3.10}$$

Inverse transforms then can be recorder for equations 3.9,3.10:

$$x(t) \equiv \int_{-\infty}^{\infty} X(f)e^{-i2\pi ft}dt \tag{3.11}$$

$$x(t) \equiv \frac{1}{\sqrt{2\pi}} \int_{-\infty}^{\infty} X(\omega)e^{-i\omega t}dt \tag{3.12}$$

The result of an FT is generally complex, which can be easily seen from its representation by substituting Euler's formula $e^{-i\omega t} = \cos(\omega t) - i\sin(\omega t)$ in Eq. (3.10):

$$X(\omega) = \frac{1}{\sqrt{2\pi}} \int_{-\infty}^{\infty} x(t)\cos \omega t dt - \frac{i}{\sqrt{2\pi}} \int_{-\infty}^{\infty} x(t)\sin \omega t dt \tag{3.13}$$

For example, application of FT to a time dependent function will yield its representation as complex coefficients, carrying information about amplitude and phase, as a function of frequency. Applications in signal processing are not, however, limited only to time signals, in the same fashion FT can be applied to space dependent function and yield spatial harmonics. In analysis of signals from different sources or of different nature it is the magnitude of these complex coefficients that is, usually, of the most interest. Such widespread utilization of FT is a consequence of Parseval's theorem, which proves conservation of signal energy between time and frequency representations:

$$E = \int_{-\infty}^{\infty} |x(t)|^2 dt = \int_{-\infty}^{\infty} |X(f)|^2 df \tag{3.14}$$

where $|X(f)|^2$ is signal spectral density, that describes distribution of energy of a signal as a function of frequency. 'Energy' is generally used in the sense of signal energy, but can be, for example interpreted as an electrical energy of oscillating voltage. This treatment is adequate for signals that are transient - e.g. finite in their duration, thus having finite total energy. For such signals notion of Energy Spectral Density (ESD) is applicable:

$$E_{xx}(f) = |X(f)|^2 \tag{3.15}$$

However, if the signal is stationary, ESD is not useful, as energy will not be finite. In order to counteract this, power can be used. Defining power of the signal as its square:

$$P = \lim_{T \to \infty} \frac{1}{T} \int_0^T |x(t)|^2 dt \tag{3.16}$$

Notion of finite length signal, $t = (0, ..., T)$, implies that FT has to be truncated as well, giving amplitude spectral density:

$$X(\omega) = \frac{1}{\sqrt{T}} \int_0^T x(t) e^{-i\omega t} dt \tag{3.17}$$

From which Power Spectral Density (PSD) can be directly calculated:

$$P_{xx}(f) = \lim_{T \to \infty} \frac{1}{T} E\left[|X(f)|^2\right] \tag{3.18}$$

Comparison of spectral composition of two signals, $x(t), y(t)$, can be calculated with Cross-Power Spectral Density (CPSD), which is closely related to ordinary PSD, however manipulating two functions instead of one:

$$P_{xy}(f) = \lim_{T \to \infty} \frac{1}{T} E\left[X^*(f) Y(f)\right] \tag{3.19}$$

Output is generally complex, from which difference in phase and magnitude between signals at different frequencies can be extracted.

3.1.3   Time evolution of spectral composition

Limitation of regular FT is that it does not allow to observe evolution of spectral composition, for example two different linear chirp signals with rising and decaying frequencies will have the same PSD. One of the ways to overcome this is Short-Time Fourier Transform (STFT) which allows to track changes in spectral composition of signals as a function of time by decomposing them from 1D time array into 2D time-frequency space. This technique is implemented by selecting part of the studied signal in vicinity of a time point, by applying a windowing function, $w(t)$, to smooth out the sharp edge effect and then performing spectral decomposition of the result via FT. The result is assigned to the time point τ where the center of windowing function was located. Then the windowing function is shifted further along the time axis and the process is repeated yielding spectral composition of signal as a function of time. This process includes various parameters for

adjustment, such as windowing function, its length and overlap for neighboring measurements.

$$X(\tau,\omega) \equiv \int_{-\infty}^{\infty} x(t)w(t-\tau)e^{-i\omega t}dt \tag{3.20}$$

where the windowing function $w(t)$ is a square integrable short-time function of fixed width, that is shifted by τ along the time axis. Hamming window is widely used in analysis 3.21:

$$w(t) = 0.54 - 0.46\cos\left(\frac{2\pi t}{T}\right) \tag{3.21}$$

with T denoting window length and $w(t)$ is defined within $[-T/2, T/2]$ and the values are zero outside the window. It can be seen that the result of STFT is, analogous to the output of FT, is generally complex, representing time-evolution of phase and magnitude of the input signal. Like the FT, most applications of STFT are concerned with energy distribution within the spectrum. Spectrogram takes the same approach as PSD, by taking square of magnitude of complex vectors of STFT:

$$E_{xx}(\tau,\omega) = |X(\tau,\omega)|^2 \tag{3.22}$$

Analogous to CPSD, being a result of multiplication of two Fourier-images of signals, cross-spectrogram can be defined as a multiplication of two STFT-images of two signals:

$$E_{xy}(\tau,\omega) = |X(\tau,\omega)Y^*(\tau,\omega)|^2 \tag{3.23}$$

Comparison between FT and STFT applied to the same chirp signals discussed earlier is demonstrated in Fig. 3.1. Main consideration with the utilization of STFT is the limited resolution. That follows the uncertainty relation:

$$\Delta t \Delta f \geq (4\pi)^{-1}, \text{or equivalently} \quad \Delta t \Delta \omega \geq (2)^{-1} \tag{3.24}$$

This constraint appears as resolution in frequency space is proportional to the number of the analysed data points multiplied by the sampling rate , e.g., to the length of the window. On the opposite, the time resolution is inversely proportional to the window length, e.g., increases with shortening of window.

3.2 Refractive index measurements

3.2.1 Amplitude measurements

First reflectometer experiments based on plasma refractive index were quite straightforward: propagation, attenuation and reflection of microwave signal were studied. Signal from a MW generator with a known frequency passes a one-way ferrite valve and directional coupler and gets launched to plasma by a horn antenna. Part of the signal is successfully transmitted, a fraction is absorbed, and a fraction is reflected
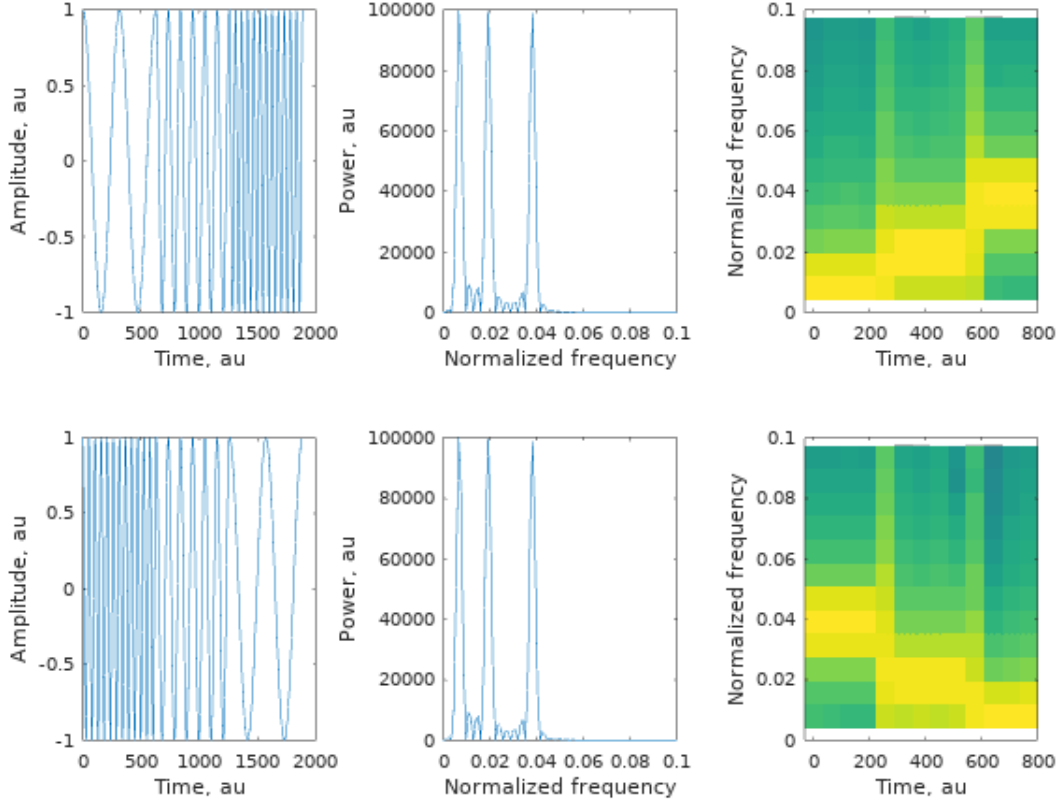
Figure 3.1: Two different chirp signals (left) analysed via FT (middle) and STFT (right).

back. The reflected signal, detected by the same emitting antenna is separated by a directional coupler and detected. This diagnostic provides relative measurements of the reflected and transmitted signals. When the plasma density is significantly lower than critical, the MW beam propagates through the plasma with negligible attenuation and gets detected by a receiving antenna horn. However, as plasma density gets closer to the critical, attenuation and reflection grow, until the moment of the resonance when critical density is reached. At this moment beam transmission abruptly decreases almost to zero, and, if plasma density keeps increasing, plasma with density above critical level causes increase in signal reflection. Then, when plasma density decreases below critical density, a reverse process will occur, bringing transmission to a high level. This method allows to determine the moment when plasma somewhere along the beam path reaches critical density, a known value for a certain frequency of microwaves. This method may be extended by adding an array of similar systems operating on different frequencies at the same cross-section, effectively allowing determination of the time when plasma density reaches critical density for each beam, and then the time when it decreases below the critical values, thus increasing resolution of measurements. One antenna on one side can be utilized both for launching and receiving in the following fashion: instead of being picked-up by a receiving antenna, the signal simply reflects of the opposite conductive wall of the vacuum vessel and propagates back to the transmitter antenna. Due to superposition, the amplitude of the detected signal will

be proportional to the sum of transmitted and reflected signals. Exactly at the time when plasma density is equal to the critical density, wave will be effectively absorbed by plasma ($\omega_{MW} \approx \omega_{plasma}$), resulting in significant decrease in the amplitude of the output signal. Signals illustrating above stated experiments for both one- and two-antenna setups are provided on Fig. 3.2, which depicts transmitted and reflected signals for an arbitrary time-dependent density profile. These techniques allow one to obtain information about moment of time when plasma density reaches critical value somewhere along the beam path based exclusively on amplitude of the signals.
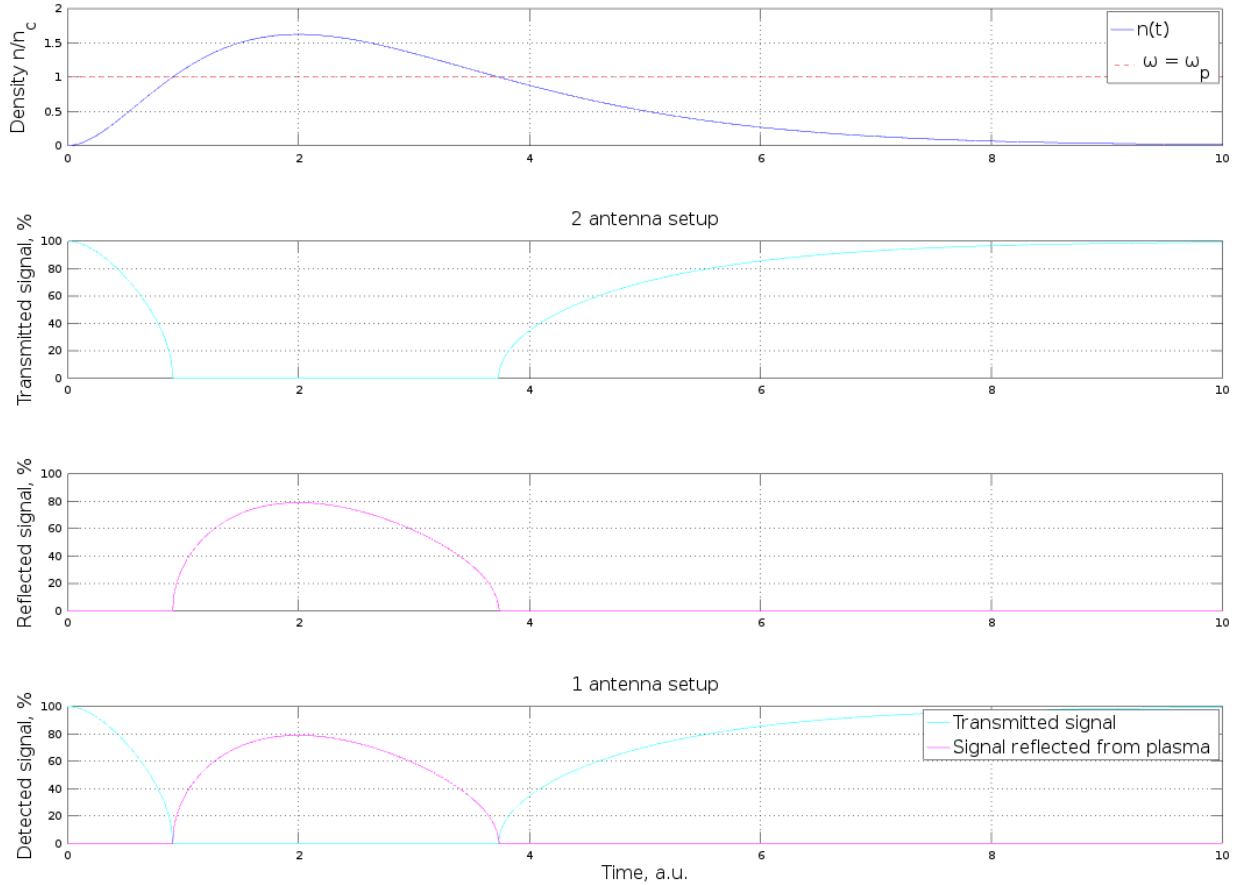
Figure 3.2: Plasma density experiment based on change in plasma refractive properties when critical density is reached.

3.2.2   Line average density measurements

Phase shift occurring during propagation of microwave beam through plasma can be written:

$$\phi = \int N \frac{\omega}{c} dx \tag{3.25}$$

Then, by subtracting phase lag of reference arm without plasma:

$$\delta\phi = \int (N-1)\frac{\omega}{c}dx \tag{3.26}$$

and by substituting N, one can obtain:

$$\delta\phi = \frac{\omega}{c}\int \left(\sqrt{1-\frac{n}{n_c}}-1\right)dx \tag{3.27}$$

Above equation provides information for line average density along beam path, and for $n \ll n_c$, which holds true for most interferometer applications, N can be approximated:

$$N \approx 1 - \frac{1}{2}\left(\frac{n}{n_c}\right) \tag{3.28}$$

Resulting in:

$$\delta\phi_I = -\frac{\omega}{2cn_c}\int n(x)dx \tag{3.29}$$

Line average density can be defined as:

$$\bar{n} = \frac{1}{2a}\int_{-a}^{a} n(x)dx \tag{3.30}$$

where a and $-a$ are plasma boundaries. So the line average density as a function of probing beam's phase can be expressed and measured:

$$\bar{n}(t) = -\frac{cn_c}{a\omega}\delta\phi_I(t) = -\frac{cn_c}{a2\pi f}\delta\phi_I(t) \tag{3.31}$$

3.2.3 Wave reflection from rippled surface

As it has already been demonstrated, if an EM-wave travelling through plasma encounters a region with density higher than critical value, it will not be able to propagate and will be reflected. Distance over which reflection happens has finite length, Δr, and is determined by wavelength, λ, of probing wave and steepness of density gradient in plasma. In typical fusion experiments this distance is of the order of 10 mm, or larger. However, there is evidence from correlation reflectometry experiments, which indicates that radial coherence lengths are smaller, typically of the order of several mm in tokamak edge regions [28]. Which suggests that the reflection region is significantly more localized, $\Delta r \ll \lambda$, allowing to treat that region as an infinitely conducting thin layer. Such a layer of plasma, where local density is equal to critical density, $n(\mathbf{x},t) = n_c(\omega)$, is called the reflection layer. Despite the fact that all plasma fluctuations along the beam path contribute to parameters of wave, theoretical and experimental evidence supposes strongest sensitivity in the close vicinity of the reflection layer [29] [19] [27] . That allows in first approximation to use the simplified "distorted reflector" model, which only includes effects from the vicinity of the reflection layer, to interpret the reflectometer signals. Following the model proposed by Conway [28], plasma will be treated as

a smooth conducting surface. As the reflectometer detects reflected EM-wave, it is necessary to understand how properties of that wave will change with movement and modulation of that surface, $\xi(\mathbf{x}, t)$. The scalar electric field, $E_2(\mathbf{x_0})$[1], can be calculated with Helmholtz integral:

$$E_2 = \frac{1}{4\pi} \int \int \left(E_S \frac{\partial \psi}{\partial n} - \psi \frac{\partial E_S}{\partial n} \right) dS \tag{3.32}$$

where E_S is the field at the reflective surface and n is the normal vector to the surface. As the distance from the reflection surface is large, Green's function for scattered wave will be plane wave:

$$\psi = \frac{e^{i(k_2 \cdot r_0 - \mathbf{k_2} \cdot \mathbf{r})}}{r_0} \tag{3.33}$$

where $\mathbf{k}_2$ is wave vector and r is distance from surface to point $\mathbf{x_0}$. In order to to solve that problem the electric field at surface, E_S, should be defined, which can be done in Kirchhoff approximation, as already the smoothness of the surface was assumed:

$$E_S = (1 + F)E_1 \tag{3.34}$$

$$\frac{\partial E_S}{\partial n} = (1 - F)E_1 \mathbf{k_1} \cdot \mathbf{n} \tag{3.35}$$

where F is Fresnel reflecting coefficient which is defined as:

$$F = \frac{E_2}{E_1} \tag{3.36}$$

At plasma cut-off $\epsilon \to 0$, so $F \to 1$. Incident beam can be modelled as a paraxial Gaussian with unit amplitude and independent of time:

$$E_1 = e^{-x^2/w^2} e^{i(\mathbf{k_1} \cdot \mathbf{r})} \tag{3.37}$$

where w is the beam radius at $1/e$ amplitude.

Now it is necessary to define the reflecting surface more precisely. The following derivation for 2D perturbation should be sufficient for this particular application. Dominant modes in tokamak are poloidal, e.g. variation happens with poloidal angle. resulting in a reflective surface with perturbation 'ripples' elongated along magnetic field lines, i.e. predominantly in toroidal direction. These ripples propagate perpendicular to the reflectometer beam in predominantly poloidal direction. Using procedure of Beckmann and Spizzichino [30] for perturbation defined in a region from $-L$ to L expression for E_2 can be obtained:

$$E_2 = \frac{ike^{ikr_0}}{4\pi r_0} \int_{-L}^{L} (a\xi' - b) e^{-x^2/w^2} e^{i(v_x x + v_z \xi)} dx \tag{3.38}$$

---

[1]Here and further in this section subscripts 1 and 2 are used for incident and reflected waves respectively

where

$$a = (1 - F)\sin\theta_1 - (1 + F)\sin\theta_2 \tag{3.39}$$

$$b = (1 - F)\cos\theta_2 - (1 - F)\cos\theta_1 \tag{3.40}$$

$$v_x = k_1(\sin\theta_1 - \sin\theta_2) \tag{3.41}$$

$$v_z = -k_1(\cos\theta_1 + \cos\theta_2) \tag{3.42}$$

$$\xi = h\cos(2\pi x/\Lambda + \vartheta(t)) \tag{3.43}$$

$$\xi' = \frac{\partial\xi}{\partial n} = \frac{\partial\xi(x,t)}{\partial x} \tag{3.44}$$

θ is an angle between beam and normal. In this model surface perturbations are imitated with periodic harmonic function, of amplitude h, wavelength Λ, with variable phase, $\vartheta(t)$, demonstrated in Fig. 3.3. Equation (3.38) can be normalised by field, E_{20}, reflected from a smooth flat, ($\xi = \xi' = 0$) conducting ($F = -1$) surface in the specular direction ($\theta_1 = \theta_2$) to give scattering coefficient, ρ:

$$\rho(t) = \frac{E_2}{E_{20}} = \frac{\int_{-L}^{L}(a\xi'(t) - b)e^{-x^2/w^2}e^{i(v_x x + v_z \xi(t))}dx}{2\cos\theta_1 \int_{-L}^{L} e^{-x^2/w^2}dx} \tag{3.45}$$

Then the mean reflected power, $\langle P_2 \rangle$, can be expressed:

$$\langle P_2 \rangle = \frac{1}{2\epsilon_0\mu_0}\langle E_2 E_2^* \rangle = \frac{1}{2\epsilon_0\mu_0}|E_{20}|\langle\rho(t)\rho^*(t)\rangle \tag{3.46}$$

The detected reflectometer power and phase signals according to the model should follow:

$$P_{Refl}(t) \propto \langle\rho(t)\rho^*(t)\rangle \tag{3.47}$$

$$\phi_{Refl}(t) = \arctan\left(\frac{\text{Im }\rho(t)}{\text{Re }\rho(t)}\right) \tag{3.48}$$

For the case of reflectometer normal incidence is occurring

$$|R|e^{i\psi_r} = \frac{1 - \sqrt{\epsilon}}{1 + \sqrt{\epsilon}} \tag{3.49}$$

It was shown that for such harmonically perturbed surface three distinct regimes exist depending on the wavelength of ripples [28]:

1. Long ($\Lambda/\lambda \geq 10\omega/\lambda$): Surface appears flat to incident beam irrespective of ripple height h. Modulation of reflected power is small, however, as the reflective surface moves inwards and outwards from the antenna, phase will be modulated at a frequency $f_r = v_{ph}/\Lambda$.

2. Short ($\Lambda/\lambda \leq 2\omega/\lambda$): Due to Bragg scattering, power can be significantly attenuated at certain ripple heights, h, which makes phase detection problematic or even impossible. Power modulation with ripple

41
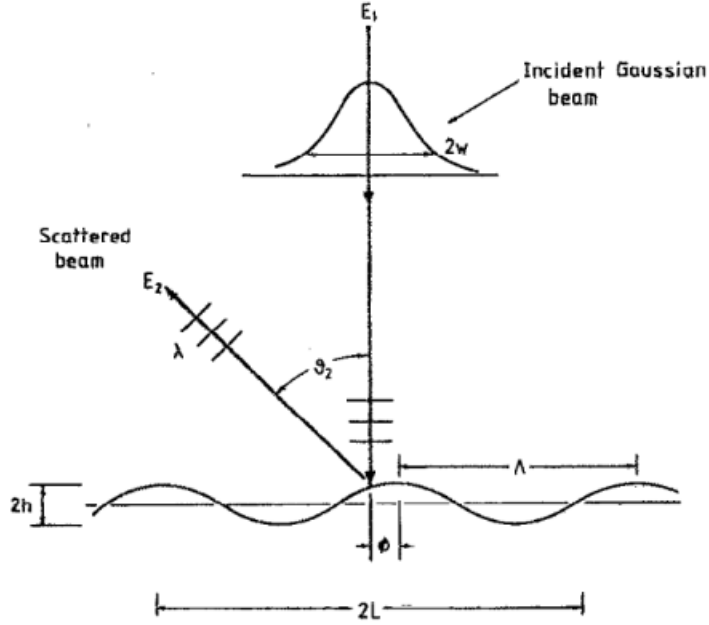
Figure 3.3: Illustration of a simulated surface, incident Gaussian and scattered beams. Adopted from: G. D. Conway. Scattering of reflectometer signals from rippled surfaces. *Review of Scientific Instruments*, 64(10):2782–2788, 1993.

phase is weak.

3. Intermediate ($2\omega/\lambda \leq \Lambda/\lambda \geq 10\omega/\lambda$): Overlap of zeroth and first-order scattering lobes gets swept across antenna as ripple phase changes, causing substantial modulation of power at frequency of $2f_r$. The back scattered power as well depends on ripple height and wavelength.

3.2.4 Displacement of reflective surface

By utilizing the long ripple wavelength approximation, and considering reflection from a smooth surface, information about displacement of the cut-off layer as a function of time can be extrapolated from the reflectometer phase. Such experiments were conducted at JET tokamak [29]. Rewriting total phase change of MW beam accumulated on its way to plasma, due to reflection and on the way back to detector:

$$\delta\phi = \frac{\omega}{c}\int_{x_c}^{a} N(x)\ dx - \pi/2 + \frac{\omega}{c}\int_{a}^{x_c} N(x)\ dx \tag{3.50}$$

Where a stands for plasma outer edge and x_c is the coordinate of the layer with critical density n_c. Assuming that plasma properties do not change significantly during the time that the wave travels through plasma, the second integral in Eq. (3.50) should yield approximately the same value as the first one. Defining a mean refractive index:

$$\bar{N} = \frac{1}{a - x_c}\int_{x_c}^{a} N(x)\ dx \tag{3.51}$$

allows to rewrite Eq. (3.50):

$$\delta\phi = \frac{\omega}{c} 2\bar{N}(x_c)(a - x_c) - \pi/2 \tag{3.52}$$

For the density profile of the following form $n(r,t) = n_0(t)\left(1 - (r/a)^\eta\right)$, it was shown, that $\bar{N}$ depends weakly on the profile shape, defined by parameter η. Except for in nearly flat regions, $\bar{N}$ lies in the range 0.5-0.66, for η in the range 1-10. So a constant value of $\bar{N} \approx \check{N} = 0.6$ can be substituted with accuracy within 15%. So that displacement of the cut-off layer can be expressed:

$$\delta x_c(t) = \frac{c}{\omega 2\check{N}} \delta\phi(t) \tag{3.53}$$

3.2.5 Phase measurements

Both 17mm and 4mm interferometer systems use identical quadrature phase detection and, because of that, have many similarities in their arrangement and data processing techniques. Algorithm of the phase measurements will be identical for both. Result of interference between two fields $E_1 \exp i\omega t$ and $E_2 \exp i(\omega t + \phi)$ with phase difference ϕ is a superposition of the field E_S, which is being detected by a single detector:

$$E_S = (E_1 + E_2 \exp(i\phi)) \exp(i\omega t) \tag{3.54}$$

Defining amplitude in the reference $E_1 = E_{ref}$ and plasma $E_2 = E_{pl}$ arms of interferometer we can rewrite previous equation, taking into account, that MW diodes work as square-law detectors, e.g. with output proportional to square of electric field $V_{out} \propto |E|^2$.

$$V_{out} \propto |E_s|^2 = (E_{ref}^2 + E_{pl}^2)\left[1 + \frac{2E_{ref}E_{pl}}{E_{ref}^2 + E_{pl}^2}\cos\phi\right] \tag{3.55}$$

Detected signal consists of a constant component plus a component varying like $\cos\phi$. Difference in phase arises from the changes of refractive index in one of the arms of the interferometer. However, if one attempts to measure the phase shift based on Eq. (3.55), two obstacles arise:

1. Amplitudes of E_1 and E_2 may be varying, so it is necessary to distinguish them from the phase variations, which are of the main interest.

2. Ambiguity of phase change direction. This happens when $\phi = 0, \pi, 2\pi$ and so forth, because sensitivity of interferometer turns to zero $d|E_t|^2/d\phi = 0$. So it is impossible to distinguish if any change of the sign of $d\phi/dt$ happened. Such information may be obtained from other diagnostic tools, however it is not always applicable.

Quadrature detection scheme was introduced to prevent ambiguity in measurements. It is based on introduction of the third interferometer arm, acting as a second reference. Additional information can be obtained if a $\pi/2$-delay device is added to that arm. By comparing the signal from plasma to different

references separated by $\pi/2$ phase delay allows to overcome the ambiguity, because there is never a moment when $d|E_t|^2/d\phi = 0$ for both of the channels simultaneously. Still it is important to mention, that such modification is obviously more complicated in realization. This allows to overcome ambiguity of phase change, however, does not account for possible changes in amplitudes E_1, E_2 of interfering waves.

3.2.6 Zero-crossing algorithm for phase counting

Zero-crossing technique is a straightforward technique, allowing to overcome difficulty of possible amplitude variation. For both interferometer and reflectometer measurements which, in fact, as it has already been shown, rely on the same scheme of signal detection it is necessary to extract information about change of phase ϕ from detector signal F, sometimes also referred to as interference fringe, of the form:

$$F = A(t)\cos(\phi(t)) \tag{3.56}$$

From the time of its first implementation on STOR-M 4mm homodyne interferometer utilized an analogue fringe-counter circuit. It provided density measurements by means of analog fringe counting circuit based on zero crossing detection.

This method works under assumption that amplitude of fringe, when attenuated, stays positive and detectable, which allows to associate signal zero to the condition when $\cos(\phi) \to 0$. By detecting those zero-crossings of the single signal it is possible to track phase change in increments of π. Application of the same algorithm to signals obtained via quadrature detection not only allows to determine sign of the phase change, but additionally increases overall the resolution to $\pi/2$. However, implementation of analogue counter had issues, routinely requiring adjustments of the signal bias for comparator circuits. Problem manifested itself in 'divergent' density calculations, e.g. miscounted steps of increasing or decreasing phase. This shortcoming can be easily understood: if one follows the aforementioned procedure for a periodic signal with a constant offset, same justification and understanding of zero crossing technique will not be justified. In extreme cases, for relatively low amplitude to bias ratios, signal will be offset from original axis so much that its peak will not reach it, e.g. no zero crossing will be detected, leading to miscounting. Biasing of the diodes is an operational necessity, so it cannot be avoided. Application of RC-filtering after pre-amplification stage in order to eliminate DC-bias is also not possible, as not only it may potentially distort signals, but more importantly, impeding algorithm from proper functioning at constant or sufficiently slowly varying phases. To eliminate the necessity of frequent manual bias adjustments and to increase reliability of measurements an objective was set to convert the system to a digital processing.

Numerical implementation of zero-crossing algorithm in Octave code was done with emphasis on vectorization. Vectorization is the term used to describe techniques that handle not individual data cells of a signal array via iterative operations, but the whole signal as a vector. This technique is particularly useful for such programming languages such as Octave or Matalab, which are specifically optimized to perform such types

of operations faster and with higher efficiency. This is highly motivated as in line average density calculation for interferometer, such operation is invoked until the proper offset for the signals is found. This would be extremely inefficient otherwise.

It is necessary to obtain $\delta\phi(t)$ as a function of time from two fringe signals $I[t]$ and $Q[t]$. Algorithm of the zero-crossing counter is as follows. At the first stage both $I[t]$ and $Q[t]$ are passed to *sign* function which is defined:

$$\text{sign(x)} = \begin{cases} 1, & x \geq 0 \\ -1, & x < 0 \end{cases} \tag{3.57}$$

Then, to reveal the time points of zero-crossings, each array is piece-wise multiplied with a copy of itself shifted one sample forward in the following fashion:

$$Cr_I[t] = \text{sign}(\text{I}_{\text{sign}}[\text{t}]) * \text{sign}(\text{I}_{\text{sign}}[\text{t}+1]) \tag{3.58}$$

In order to complete this operation array has to be extended by one element, this is done by copying last value of the array $(I_{\text{sign}}[t_{end}+1] = I_{\text{sign}}[t_{end}])$. The result is truncated after multiplication at the last digit, to preserve the same number of elements as an original signal. Effects at this last digit are insignificant as sampling ends at stationary regime, after the end of the discharge, when no plasma is present. Operation results in 2 arrays, Cr_I and Cr_Q, where locations of zero crossings will have value -1. Equation (3.58) in essence multiplies neighboring signals and output can only be negative if in the time interval between samples a sign change has occurred. For all other cases signs will cancel out to be positive. Then all positive values are nullified and sign of negatives is changed to positive:

$$Cr_I[t] = \begin{cases} Cr_I[t] = -Cr_I[t], & Cr_I[t] < 0 \\ Cr_I[t] = 0, & Cr_I[t] > 0 \end{cases} \tag{3.59}$$

yielding an array with values of 1 at locations of zero-crossings and 0's elsewhere. Then, in order to interpret if phase was increased or decreased at each step, array of zero-crossings of signal $I[t]$, Cr_I is piece-wise multiplied by arrays of signs of $I[t+1]$ and $Q[t+1]$:

$$\delta\phi[t] = Cr_I[t] * \text{sign}(\text{Q}_{\text{sign}}[\text{t}+1]) * \text{sign}(\text{I}_{\text{sign}}[\text{t}+1]) \tag{3.60}$$

giving the rate of change of phase. This operation might be easier to understand, when properties of quadrature detection are considered. As $I[t] \propto \cos\phi[t]$ and $Q[t] \propto \sin\phi[t]$, so there is $\pi/2$ phase delay between them. For example if phase is growing, cos will be 'lagging', and product of $sign(Q_{sign}[t+1]) * sign(I_{sign}[t+1]) < 0$ will be negative. If phase decreases, $sign(Q_{sign}[t+1]) * sign(I_{sign}[t+1]) > 0$. Resulting signal will have spikes of unitary magnitude at each zero crossing, with the sign indicating either increase or decrease of phase. After integrating the signal numerically, by taking a cumulative sum, phase signal is recreated. Applying the

45

same treatment to both signals and combining the outputs will result in a signal as a function of time, with resolution of $\pi/2$ and temporal resolution of one sampling period. Example of application of zero-crossing algorithm to synthetic time traces at its different stages is presented on Fig. 3.4.
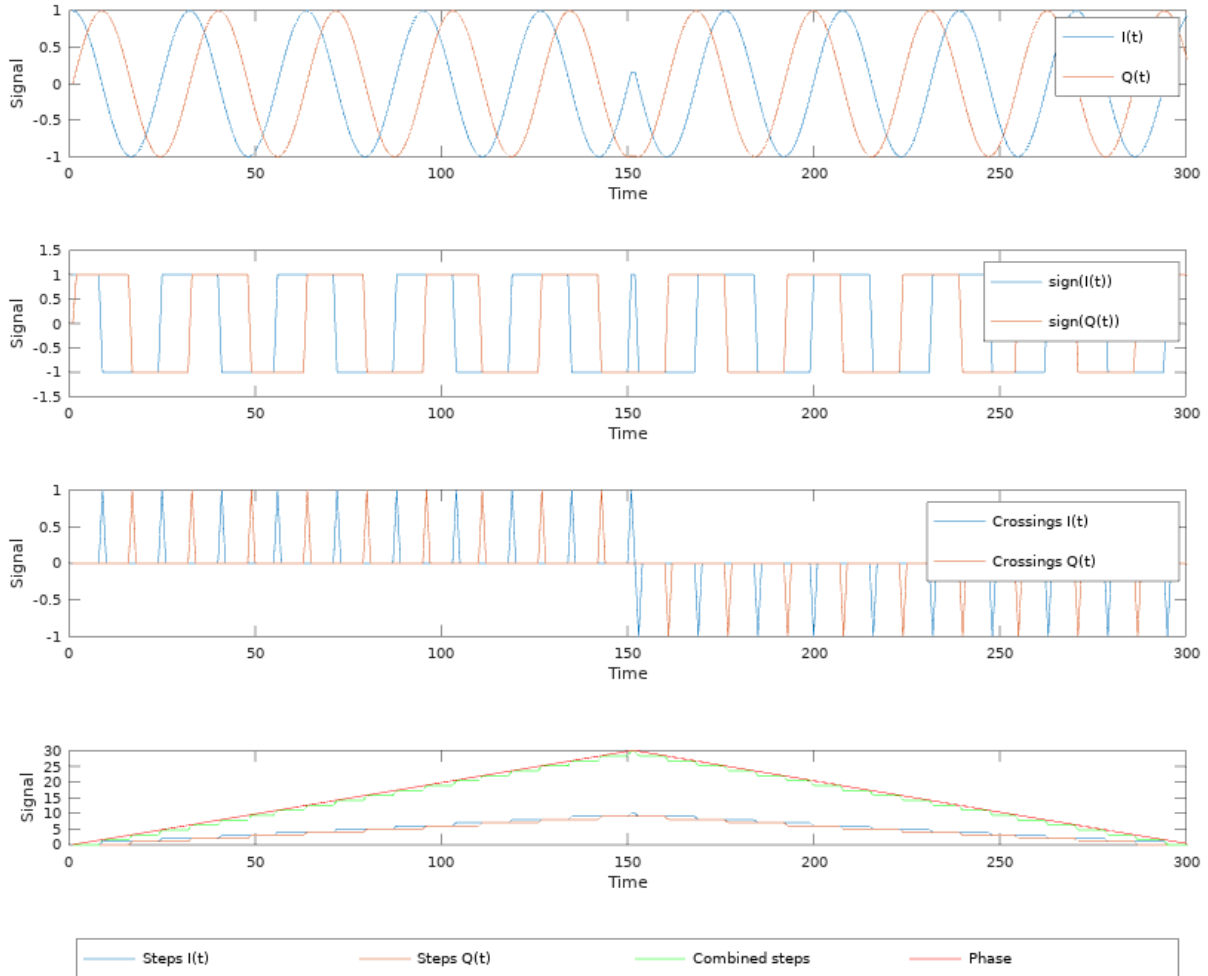
Figure 3.4: Demonstration of stages within zero-crossing algorithm for synthetic data.

3.2.7 Continuous phase counting

After digitizing the signal it becomes possible to perform more complicated computation than with an analogue counter, so it is profitable to use this opportunity and improve the phase detection resolution. In order to do so fringe counting technique should be substituted by a way to continuously measure the phase change. Output fringes $I(t), Q(t)$ of quadrature detection scheme are two signals shifted $\pi/2$ relative

to each other:

$$I(t) = A_1(t)\cos(\phi(t)) \tag{3.61}$$

$$Q(t) = A_2(t)\cos(\phi(t) + \pi/2) = -A_2(t)\sin(\phi(t)) \tag{3.62}$$

Where A_1, A_2 are amplitudes of signals. Then phase as a function of time can be expressed:

$$\phi(t) = -\arctan\left(\frac{A_2(t)}{A_1(t)}\frac{\sin(\phi(t))}{\cos(\phi(t))}\right) \tag{3.63}$$

It is necessary to know those amplitudes $A_1(t)$, $A_2(t)$ as a function of time to perform the calculation. However those amplitudes are related to the same signal from receiver antenna $A_0(t)$ attenuated by waveguides coming from antenna to each of detectors. As the frequency of the probing beam is constant and physical parameters of waveguides do not change, it is fair to assume that attenuation of the waveguides does not change as well. That allows to express $A_1(t)$, $A_2(t)$:

$$A_1(t) = \zeta_1 A_0(t) \tag{3.64}$$

$$A_2(t) = \zeta_2 A_0(t) \tag{3.65}$$

$$\phi(t) = -\arctan\left(\frac{\zeta_2}{\zeta_1}\frac{\sin(\phi(t))}{\cos(\phi(t))}\right) \tag{3.66}$$

Where $\zeta_{1,2} \leq 1$ represent attenuation coefficients for waveguides, combined with amplification gains. In case if amplifier gains are chosen to compensate proportionally to losses in waveguides, and assuming negligible variation in gains as a function of amplitude (ideal amplifier):

$$\zeta_1 = \zeta_2 \tag{3.67}$$

$$\phi(t) = -\arctan\left(\frac{\sin(\phi(t))}{\cos(\phi(t))}\right) = -\arctan\left(\frac{Q(t)}{I(t)}\right) \tag{3.68}$$

Yet, the signal will provide output only within range of $-\pi/2$ to $\pi/2$. This can be fixed by combining results with previously explained zero-crossing technique applied to $I(t)$ providing "ladder" function with steps of π.

3.2.8 Reflected power

Apart from direct measurements, in theory it is as well possible to extract information about reflected power of reflectometer beam from $I(t)$ and $Q(t)$ signals. If represented on a complex plane, where $I(t)$ and $Q(t)$ will represent real and imaginary components. Magnitude of the resultant vector is proportional to the amplitude of the reflected wave, while its angle represents the phase of the detected signal.

3.3 Triple probe

Triple Langmuir probe, as it follows from the name, utilizes three probe tips submerged into plasma, depicted in Fig. 3.5. In contrary to single and double probes, it does not rely on analysis of I-V curves, instead using simultaneous measurement of current and and voltage, in order to determine local plasma density, $n(\mathbf{x}, t)$, electron temperature, $T_e(\mathbf{x}, t)$, and floating potential, $V_{fl}(\mathbf{x}, t)$. Which allows not only to significantly increase time resolution of measurements, as no voltage sweeping is required, but, additionally considerably simplifies the schematics of the power supply and puts far less strict conditions on impedance matching.
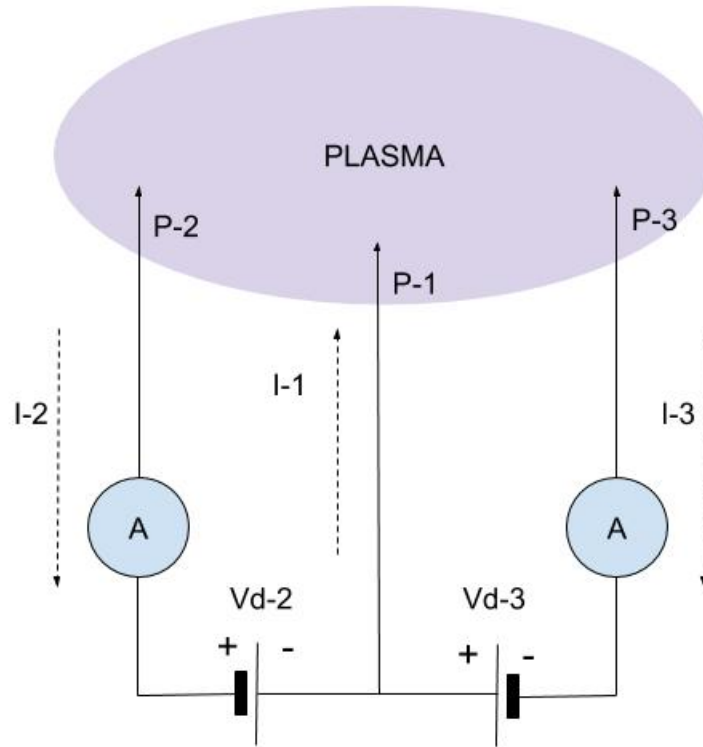
Figure 3.5: Scheme of triple Langmuir probe configuration demonstrating measured currents and voltages.

Effectively probe consists of a combination of a double probe with an additional electrode for floating potential measurements. Double probe electrodes are floated with a DC voltage source and current-meter in their circuit. Additional probe is measuring voltage difference between positively biased tip of double probe and plasma floating potential.

$$\begin{cases} I_1 = I_2 + I_3 \\ V_2 - V_1 = V_{d2} \\ V_3 - V_1 = V_{d3} \end{cases} \tag{3.69}$$

If assumptions made in derivation within section 2.2 are applicable, e.g. VDF is assumed to be Maxwellian, mean free path is significantly larger than sheath thickness (collisionless sheaths) and probe radius (planar sheath approximation). Additionally thickness of ion sheath should be smaller than spatial separation of the probe tips, so that interaction effects between sheaths can be neglected. This allows to express currents in probe tips using following equations 3.69:

$$
\begin{cases}
-I_1 = -SJ_{es}e^{-\phi V_1}SJ_{is}(V_1) \\
I_2 = -SJ_{es}e^{-\phi V_2}SJ_{is}(V_2) \\
I_3 = -SJ_{es}e^{-\phi V_3}SJ_{is}(V_3)
\end{cases}
\tag{3.70}
$$

where

$$
\phi \equiv e/kT_e
\tag{3.71}
$$

$$
J_{es} = n_e e(kT_e/2\pi m_e)^{1/2}
\tag{3.72}
$$

and J_{es} and J_{is} are electron and ion saturation current densities respectively, S is the surface area of the probe tips and k is Boltzmann constant. As ion saturation current weakly depends on voltage, in comparison to one of electrons, an assumption is made that it is equal at all three probes, $J_{is}(V_1) \simeq J_{is}(V_2) \simeq J_{is}(V_3) \simeq J_{is}$. Combining equations in 3.70 yields:

$$
\frac{I_1 + I_2}{I_1 + I_3} = \frac{1 - e^{-\phi V_{d2}}}{1 - e^{-\phi V_{d3}}}
\tag{3.73}
$$

3.3.1 Electron temperature

In the majority of particular applications, one of the probes, in this example tip number 2, is forced to stay at floating potential, V_{fl}, by removal of voltage source V_{d2}. Voltage source is substituted by a high input impedance measurement device (voltmeter or ADC). By this zero condition on current through that probe is imposed, $I_2 = 0$, and from equations 3.69, 3.73 following current ratio is obtained:

$$
\frac{1 - e^{-\phi V_{d2}}}{1 - e^{-\phi V_{d3}}} = \frac{1}{2}
\tag{3.74}
$$

As V_{d2} is measured and V_{d3} is fixed at a known value, it is possible to determine electron temperature, by recalling Eq. (3.71). If V_{d3} is sufficiently high ($\phi V_{d3} \simeq 3$) Eq. (3.74) simplifies further to give:

$$
\frac{1 - e^{-\phi V_{d2}}}{1} \simeq \frac{1}{2}
\tag{3.75}
$$

$$
e^{-\phi V_{d2}} = \frac{1}{2}
\tag{3.76}
$$

$$
\phi V_{d2} = \frac{e V_{d2}}{kT_e} = 0.69
\tag{3.77}
$$

$$
T_e = 1.44 V_{d2}[eV]
\tag{3.78}
$$

3.3.2 Floating and plasma potentials

From Eq. (2.26) plasma potential can be expressed as a function of floating potential, V_f, and electron temperature, T_e:

$$V_p = V_f + \frac{T_e}{2e} \ln \left(\frac{m_i}{2\pi m_e} \right)$$

(3.79)

3.3.3 Plasma density

Current between biased tips of the probe will be limited to ion saturation current by negatively biased tip and can be directly measured. That allows plasma density to be estimated from value of ion saturation current:

$$I_{is}(t) = 0.61 S n_e(t) e v_{Bohm}(t) = 0.61 S n_e(t) e \sqrt{\frac{kT_e(t)}{m_i}}$$

(3.80)

which allows to calculate plasma density, substituting results for electron temperature:

$$n_e(t) = \frac{I_{is}(t)\sqrt{m_i}}{0.61 \ e \ S\sqrt{T_e(t)}} \propto \frac{I_{is}(t)}{\sqrt{T_e(t)}}$$

(3.81)

3.4 Magnetic field measurements

Measurements of magnetic field, and, especially fluctuations, can be indicative of MHD activity within plasma. Various types of magnetic field probes exist, however, considering interest in fluctuations, simple inductor loops without any integrator circuits will be used. Here focus will be on arrays of coils, in which changes in magnetic field will induce voltage fluctuations according to Faraday's law of induction:

$$\varepsilon \approx -\frac{d\Phi}{dt} N$$

(3.82)

where N is the number of turns in the coil and Φ is the magnetic flux defined as:

$$\Phi = \int \mathbf{B} \cdot d\mathbf{S}$$

(3.83)

with integration taken over the small surface enclosed by the coil. Assuming that the area of the detector coil is fixed, output will be proportional to rate of change of the magnetic field:

$$\varepsilon \propto -\frac{dB}{dt}$$

(3.84)

3.4.1 Mode determination

If the magnitude of the poloidal magnetic field is known as function of poloidal angle, it can be decomposed into spatial harmonics - poloidal (m) modes. Realistically, it is impossible to measure this value continuously,

so there is a finite number of measurement locations, resulting in spatial discretization of the signal. Due to that, it is impossible to decompose the signal in the infinite Fourier series, efficiently limiting analysis up to Nyquist frequency, f_N. Nyquist frequency of the discrete signal is defined as half of the sampling frequency, $f_N = \frac{1}{2} f_s$ and it puts a limit to spectral resolution of discrete transform. Which, in turn, limits the highest detectable m-mode to be half the number of spatial samples recorded, $m_{max} = n/2$ where n is the number of coils used. It is important to mention that the mode numbers higher than m_{max} might still exist, but will not be detected due to under-sampling. Effectively, by recording signals simultaneously from all the detectors in the array, it is possible to recover spectral composition by straightforward application of FT, after the data is interpolated. Interpolation in this case is only necessary if sampling distance is non-uniform. If this operation is repeated for consequent moments of time, evolution of mode distribution can be obtained. Figure 3.6 demonstrates an example of such analysis.
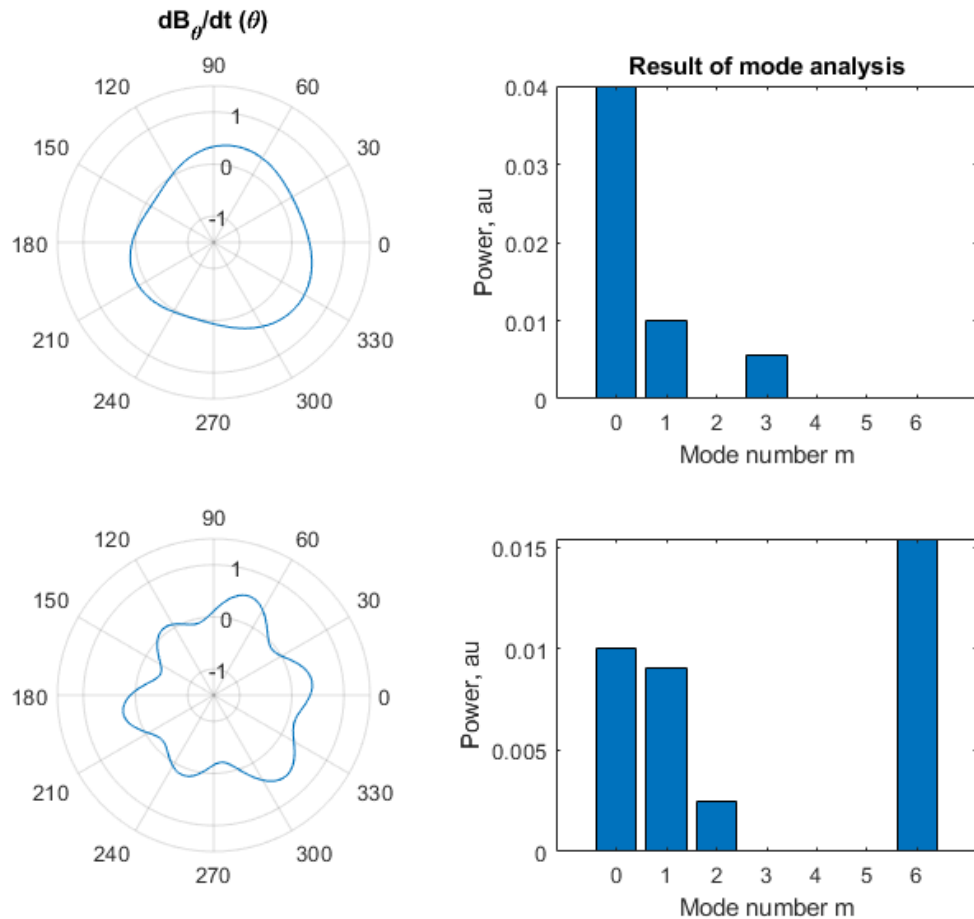
Figure 3.6: Example of mode analysis applied to two different signals.

3.4.2 Angular velocity of perturbations in poloidal direction

If signals between neighboring poloidal coils demonstrate strong cross-correlation it might be interpreted as a propagation of perturbation in the perturbation in the poloidal direction. Knowing angular separation between coils, $\delta\theta$, it is possible to estimate, taking time lag, τ, at peak of cross-correlation, angular velocity of perturbation propagation in poloidal direction:

$$\omega_\theta \approx \frac{\delta\theta}{\tau} \tag{3.85}$$

However, if perturbations are periodic, which can be determined by calculating auto-correlations for each signal individually, the cross-correlation function will be periodic as well. Problem in such case arises with determination of direction of propagation, as multiple peaks of cross-correlations are likely to be present, for both positive and negative values of time lag. In this work, it was assumed that propagation happens in the direction of highest amplitude of cross-correlation.

Chapter 4

Experimental set-up

In this chapter description of STOR-M tokamak is given along with its diagnostics. Particular attention is given to the arrangement, technical characteristics, design and limitations of diagnostics that were used or developed in this thesis work. Applicability of certain approximations and other technical considerations is also examined.

4.1 STOR-M tokamak

STOR-M stands for Saskatchewan Torus-Modified and it is a name of a tokamak device built in University of Saskatchewan's Plasma Physics Laboratory in 1983. The STOR-M tokamak is a Ohmically heated research tokamak designed and built for studies on plasma heating, anomalous transport, and developing novel tokamak operation modes and advanced diagnostics. In 1987 alternating current (AC) mode operation was achieved at 10 kA following the world's first AC tokamak operation (1 kA) on the STOR-1M tokamak, the predecessor of the STOR-M in the same lab. STOR-M has a circular cross section, with a single stainless steel limiter. Ports and coils arrangement is shown in Figs. 4.2, 4.1.

The base pressure is $6.5 * 10^{-8}$ Torr is achieved using one turbo-molecular pump in combination with a mechanical roughing pump. Fairly low pressure is achievable due to routine cleaning of vacuum vessel inner walls by a glow discharge and regular STOR-M operation. The main tokamak parameters are:

Major Radius	46 cm
Minor Radius (vert./hor.)	12/13 cm
Toroidal Magnetic Field	$0.5 \sim 1$ T
Plasma Current	$30 \sim 60$ kA
Electron Density	$1 \sim 3 * 10^{13} \text{cm}^{-3}$
Electron Temperature	$2 \sim 300$ eV
Confinement Time	$20 \sim 50$ ms

Table 4.1: Main parameters of STOR-M tokamak.

Considering the results from the previous experiments the electron temperature in the STOR-M tokamak does not exceed a few hundred eV and is significantly less than relativistic energy:

$$T \leq 250[\text{eV}] \ll M_e = m_e c^2 = 512[\text{keV}] \tag{4.1}$$
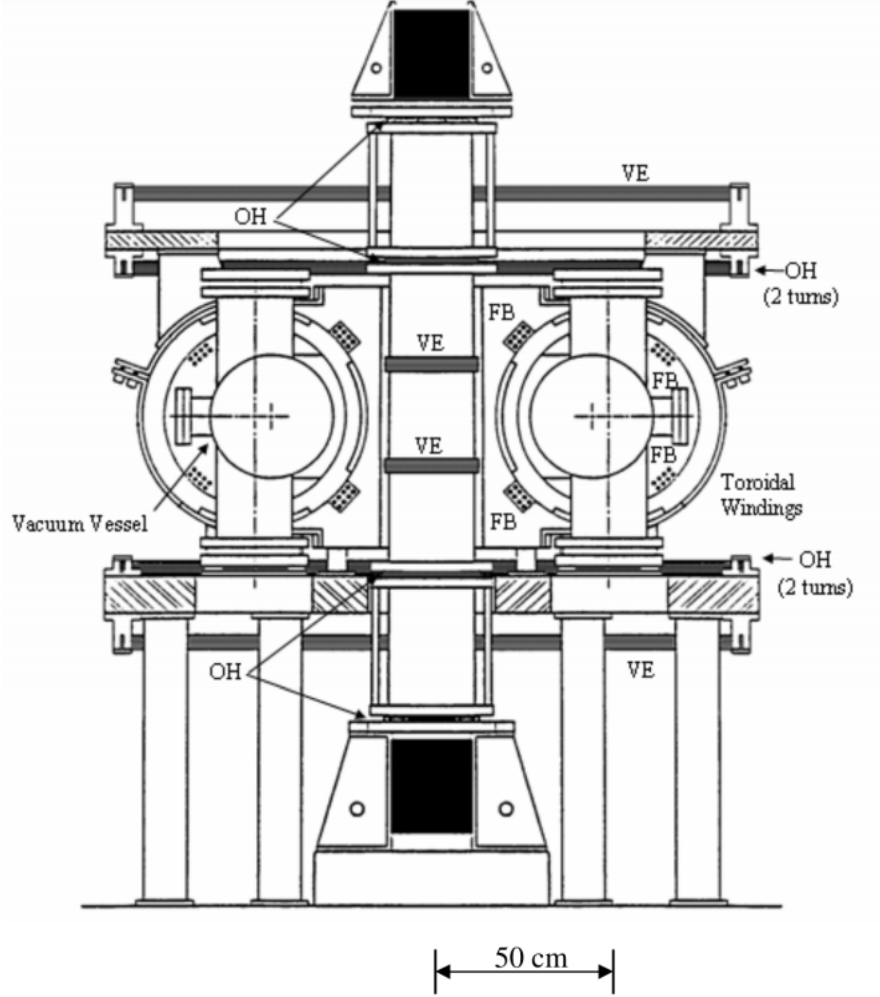
Figure 4.1: Cut-away view of STOR-M tokamak including coils and vacuum-vessel positions. Image courtesy of Plasma Physics Laboratory Archive of University of Saskatchewan.

where m_e is the electron mass. Relativistic correction coefficient for electron mass can be estimated [31]:

$$\sqrt{1 + 5T_e/M_e} = \sqrt{1 + 5 * 0.25[\text{keV}]/512[\text{keV}]} = 1.00122 \approx 1 \tag{4.2}$$

which shows a correction value of 0.1%, thus allowing to neglect relativistic effects. Figure 4.2 provides the layout for ports and diagnostics locations

STOR-M hosts a number of diagnostic tools including 4mm interferometer and 17mm reflectometer which are of our interest.

4.1.1 Effects of magnetic field direction on microwave diagnostics

As it was already shown previously, refractive index and propagation of microwave beam in plasma depends on the orientation of the magnetic field relative to the wave vector **k**. If polarization of incident wave is
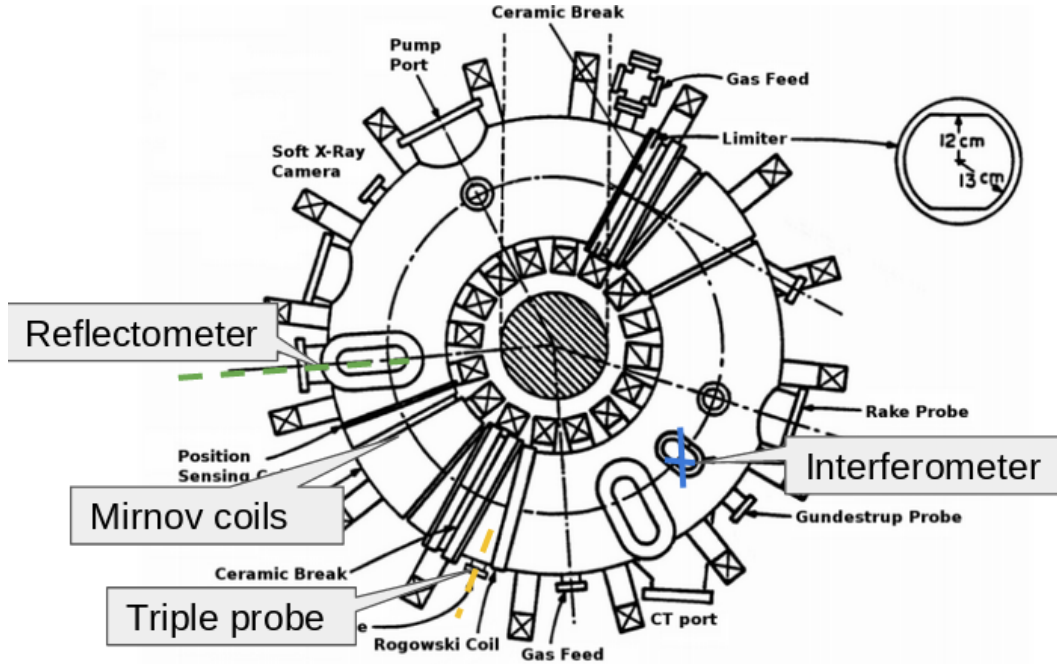
Figure 4.2: Schematic drawing from top view perspective of the STOR-M ports and diagnostics locations. Image courtesy of Plasma Physics Laboratory Archive of University of Saskatchewan.

not fully perpendicular or parallel to magnetic field, it will couple to both X- and O-modes simultaneously, causing two different waves in the plasma. This in turn will result in two different cut-off regions and two different signals picked up by the antenna. Effort should be taken in aligning antenna with respect to magnetic field. However, this gives rise to problems associated with the nature of the tokamak itself - time and spatial dependant magnetic field lines. Absolute value of toroidal field, $B_{\varphi 0}$, is not constant in time, as current inducing it is produced by discharge of capacitor bank through toroidal coils in an RLC circuit. Further, slight ($\delta B_{\varphi 0} < 10\%$) gradient in toroidal field in the direction of major radius, should be taken into account. The spatial magnetic field distribution of B_{φ} can be expressed in terms of the major radius R:

$$B_{\varphi}(R) = \frac{R_0 B_0}{R} \propto \frac{1}{R} \tag{4.3}$$

where R_0 is the radius of the central axis of the toroidal coils. Even if the toroidal field is to be assumed stationary, the poloidal field component is, generally, a function of toroidal current density which is determined by the state of the plasma, and cannot be measured easily. In the case of cylindrical symmetry with respect to the minor radius r:

$$B_{\theta}(r) = \frac{2\pi\mu}{4\pi} \int_0^a j_{\varphi}(r) dr \propto r \tag{4.4}$$

which requires knowledge of current density distribution function, j. However, for EM waves, we are interested in the magnetic field at outer minor radius, $B(a)$, and, particularly its angle, α, relative to the equatorial plane. In tokamaks, dimensionless quantity that describes the relation of toroidal and poloidal fields, and

thus, connected to the pitch angle, α, is known as safety factor q:

$$q(r) = \frac{rB_\varphi}{RB_\theta} = \frac{d\varphi}{d\theta} \tag{4.5}$$

which is generally an increasing function with the radius r for most commonly seen peaked current density distributions. Measurements of $q(a)$ are available in STOR-M, that utilize total plasma current, I_p, to estimate poloidal magnetic field B_θ. The maximum pitch angle α can be estimated:

$$q_{max}(a) = \frac{rB_\varphi}{RB_\theta} = 4.5 \tag{4.6}$$

$$\alpha = \cot^{-1}\left(q(a) \cdot \frac{R}{a}\right) = 3.35° \tag{4.7}$$

In order to excite desired O-mode wave in plasma it is necessary for electric field of the MW beam of magnitude, E_0, to be parallel to direction of the stationary magnetic field $\mathbf{B}$ ($\mathbf{E} \parallel \mathbf{B}(a)$). If E_0 is polarized perpendicular to the major radius R, $\mathbf{E_0} \perp \mathbf{R}$, and in equatorial plane (e.g. parallel to $\mathbf{E_0} \parallel \mathbf{B}_\varphi$), effect of non-zero poloidal field to coupling to X- and O-mode can be calculated:

$$E_O = E_0 \cos\alpha = 0.942E_0 \tag{4.8}$$

$$E_X = E_0 \sin\alpha = 0.058E_0 \tag{4.9}$$

which demonstrates that utilization of horn antenna directed along $\mathbf{R}$ and oriented by its short side (direction of electric field of the MW) parallel to equatorial plane, will have negligible coupling to X-mode, thus verifying configuration chosen for reflectometry measurements.

4.2   4mm Interferometer

Microwave interferometer serves as a main tool for plasma line-average density measurements at STOR-M. This unit is a homodyne single beam $\lambda = 4$mm Mach-Zender interferometer, operating at frequency $f_i = 75$ GHz. System layout is demonstrated in Fig. 4.3. Microwave beam is launched vertically from the top to the bottom of STOR-M, passing through the central chord at $r = 0$. Four microwave detectors, which are installed 2 per channel through a Magic Tee coupler. The reference signal is fed to the H port of coupler and the plasma arm signal to the E port, resulting in constructive interference for one of the detectors and destructive for another, allowing by this to reject noise and increase amplitude of the detected signal. Detectors are arranged in a quadrature detection scheme, allowing to eliminate uncertainty in the sign of phase change. From the moment of its introduction, this device used a "digital" fringe counter circuit to detect zero crossing events of each channel. Given two signals, the counter provided an analogue output as a discreet "stairs" function of phase with resolution of $\pi/2$.
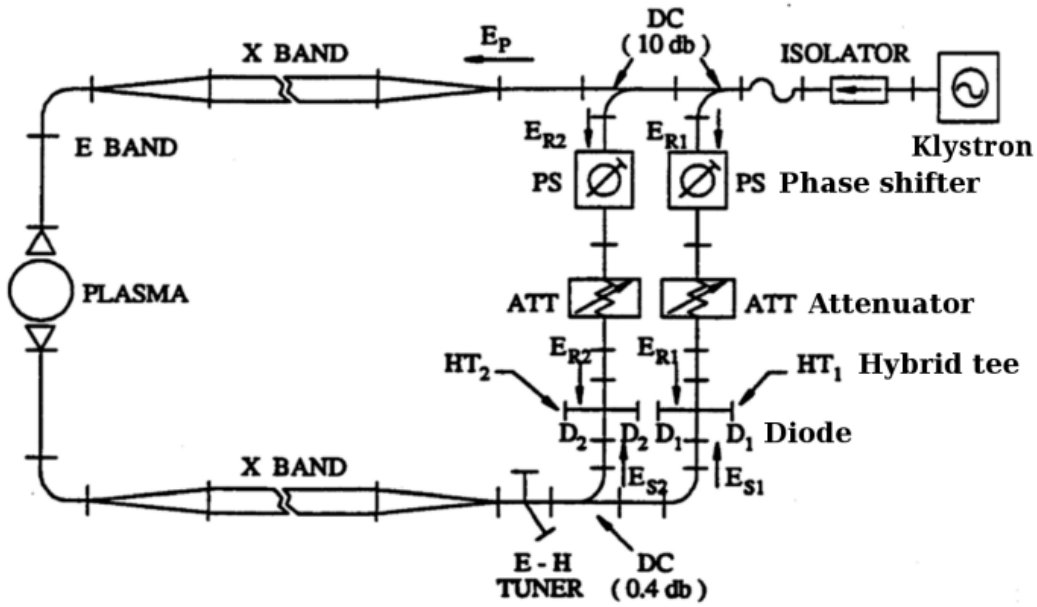
Figure 4.3: Schematic of interferometer system. Image courtesy of Plasma Physics Laboratory Archive of University of Saskatchewan.

4.3   17mm Reflectometer

Fixed frequency homodyne reflectometer is installed at STOR-M tokamak. Continuous MW beam of 200mW power at a frequency of $f_r = 17$ GHz is directed through a ferrite isolator by Ku-band waveguides to a E-H tuner, that matches it to a single 20dB horn-antenna. Its polarization is in the equatorial plane for an O-mode operation and the beam is launched to the plasma surface at the equatorial plane. Plasma is observed through a 9.5 mm thick quartz window, 96mm in diameter, tilted $10°$, to minimize reflections. Additional padding of MW-absorbing foam covering the perimeter of the window serves the same purpose. Reflected wave is detected via the same antenna and separated with directional coupler to additional waveguide. There it is splitted by another directional coupler, to two matched terminated waveguides where the signal is detected via 1N78 diodes. One of detectors, working as a square-law detector, is connected to an isolation amplifier that passes amplified signal to ADC, for direct measurements of reflected power, $P_r(t)$. Second detector is connected by means of co-axial cable to an MW-IC circuit which performs all the necessary signal splitting, phase shifting, mixing and amplification of signals, in order to output two interference signal with $\pi/2$ phase shift, $I(t)$ and $Q(t)$, for application of quadrature detection. Previous experiments [28] have verified MW-beam intensity to be approximately Gaussian within first lobe in both E- and H-planes, with normalized beam width $w/\lambda = 1.1$
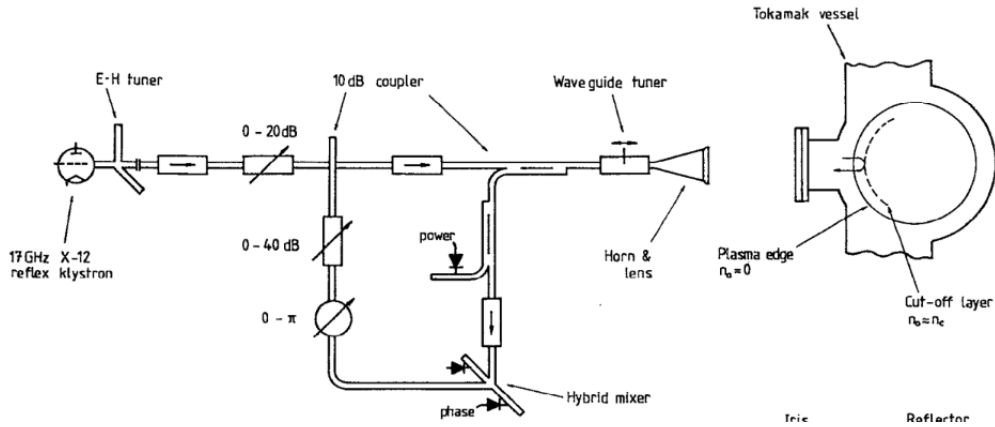
Figure 4.4: STOR-M 17mm reflectometer arrangement. Image courtesy of Plasma Physics Laboratory Archive of University of Saskatchewan.

4.4 Triple Langmuir probe

A Triple Langmuir probe assembly was developed and installed on STOR-M to provide local measurements of plasma density, electron temperature, and floating and plasma potentials in the vicinity of the reflectometer. There is a $\Delta\varphi = \dfrac{3}{8}\pi$ separation in the toroidal angle between the region of plasma which is exposed to the reflectometer beam and the TLP location.

4.4.1 Probe geometry and location

The installed probe is a quadruple probe with only 3 tips connected. The tungsten tips are cylindrical in shape, have the same dimensions of length $l = 2.6$ mm, diameter $d \approx 1$ mm, with minimal separation of $\Delta r = 2.5$ mm. The rest of the tungsten wire is covered by a hollow ceramic rod. Figures 4.6 and 4.5 depict arrangement of the probe and tip geometry. Tips are placed at the end of a linear vacuum feedthrough which allows $\Delta x = 100$ mm of travel distance. When geometry of flange and location of the port are taken into account, the accessible range of the radial positions is $(63 \leq r \leq 163) \pm 3$ mm for the tips of TLP.

4.4.2 Power supply and signal detection circuitry

A power supply unit for operation of TLP was designed and assembled. It serves two purposes simultaneously: firstly, it provides source of DC voltage for probe biasing, driving ion saturation current, and secondly it isolates outputs, allowing to 'float' the power supply. Schematics are presented in Fig. 4.7. The circuit has 4 inputs and 5 outputs. The first two input-output pairs are for floating potential measurements. Only one of them was used in the reported experiments, as the second is provisional for quad-probe operation. The third and fourth pairs are intended for ion saturation current measurements. While the last available connection is for diagnostic and maintenance purposes providing direct measurements of the battery voltage.
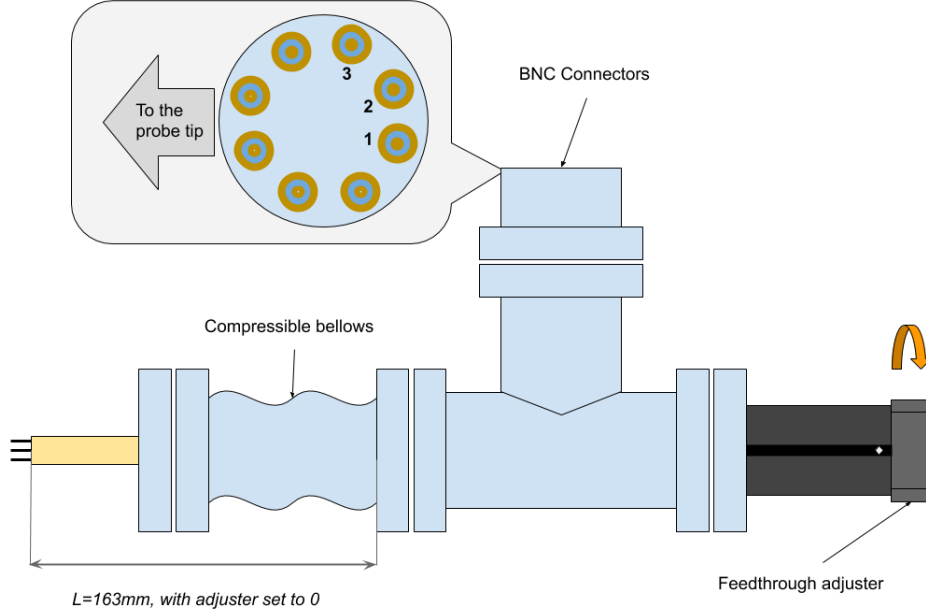
Figure 4.5: Triple probe arrangement and dimensions.

Measurements require the known constant voltage between the biased tips of the probe. Pack of 9V battery arrays, connected via selector, allowing for discrete voltage selections, serves as a convenient voltage source, allowing power supply to be easily floated. To prevent internal resistance of the batteries affecting the measurements, two filtering capacitors are used. They are connected in parallel to the battery array. The required capacitance was calculated by using data from previous experiments. The total charge required can be estimated based on the loss of the charge during the plasma discharge:

$$\delta Q = I_{is}\tau \tag{4.10}$$

where I_{is} is ion saturation current, that can be estimated to be on order of $I_i s \approx 0.1$ A, for edge-region plasma of STOR-M discharge (n=1×10^{10} cm^{-3}, $T_e = 20$eV), and $\tau = 50$ ms is duration of discharge. Substitution yields $\delta Q = 0.005$ C. Though being undesirable, fluctuation in voltage level are acceptable to a certain level, as probe current is not sensitive to changes in voltage $\dfrac{\partial I_{probe}}{\partial V_{bias}} \ll 1$. Maximum allowed voltage sag, δV was set to be within 10% of nominal value, V_{bias}:

$$\delta V \leq 0.1V_{bias} \tag{4.11}$$

Which allows to express capacitance:

$$C = \frac{\delta Q}{\delta V} \tag{4.12}$$
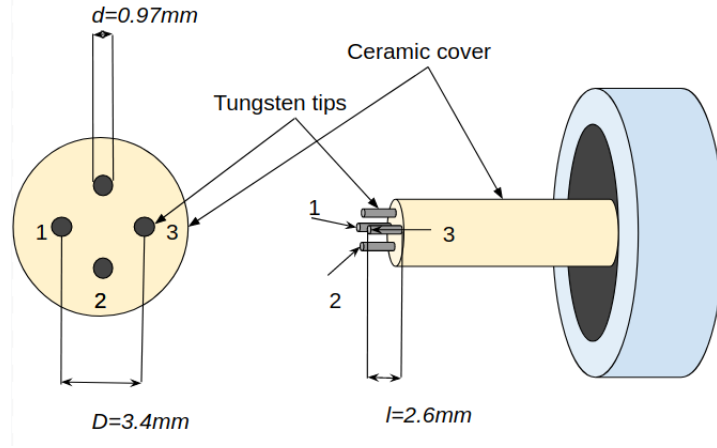
Figure 4.6: Triple probe tip dimensions.

Considering that the minimal setting of bias voltage $V_{bias} = 60$ V, the required capacitance can be calculated:

$$C = \frac{0.005}{6} \approx 1 \text{ mF} \tag{4.13}$$

However, by calculating realistic bias voltage for parameters of STOR-M plasma gives:

$$V_{bias} \geq \frac{5}{e}T_e \approx 100\text{V} \tag{4.14}$$

and, accordingly:

$$C = \frac{0.005}{10} \approx 500 \ \mu\text{F} \tag{4.15}$$

Realistically, a stack of batteries may still provide most of the current, so the calculated value was decreased 2 times, yielding 250 uF. For that electrolytic capacitor was used, additionally shunted by 1 uF ceramic capacitor in parallel, to improve response at high frequency. Voltage divider circuits are used to minimize currents from probe tips to the ground, effectively allowing to 'float' the probe while maintaining connection to DAQ. Voltages were measured with reference to the vacuum vessel wall, by directly connecting case ground to the flange of vacuum vessel. This, however, required to "float" the inputs of ADC, in order to prevent 'ground loop' effect - when wire casing is reconnected to itself via doubled ground connection creating a closed loop, which is undesirable in the presence of time-varying magnetic fields. It should be pointed out that the digitizer inputs can be floated up to 60V. Ideally, a floating amplifier can be used.

4.5   Mirnov coils

Mirnov coils are used for measurements of fluctuations in the poloidal magnetic field in a single poloidal plane. Signal is proportional to the time derivative of a magnetic field. They are routinely utilized to measure MHD activities. Originally, Mirnov coils refer to coils with a harmonically varied winding density and alternating
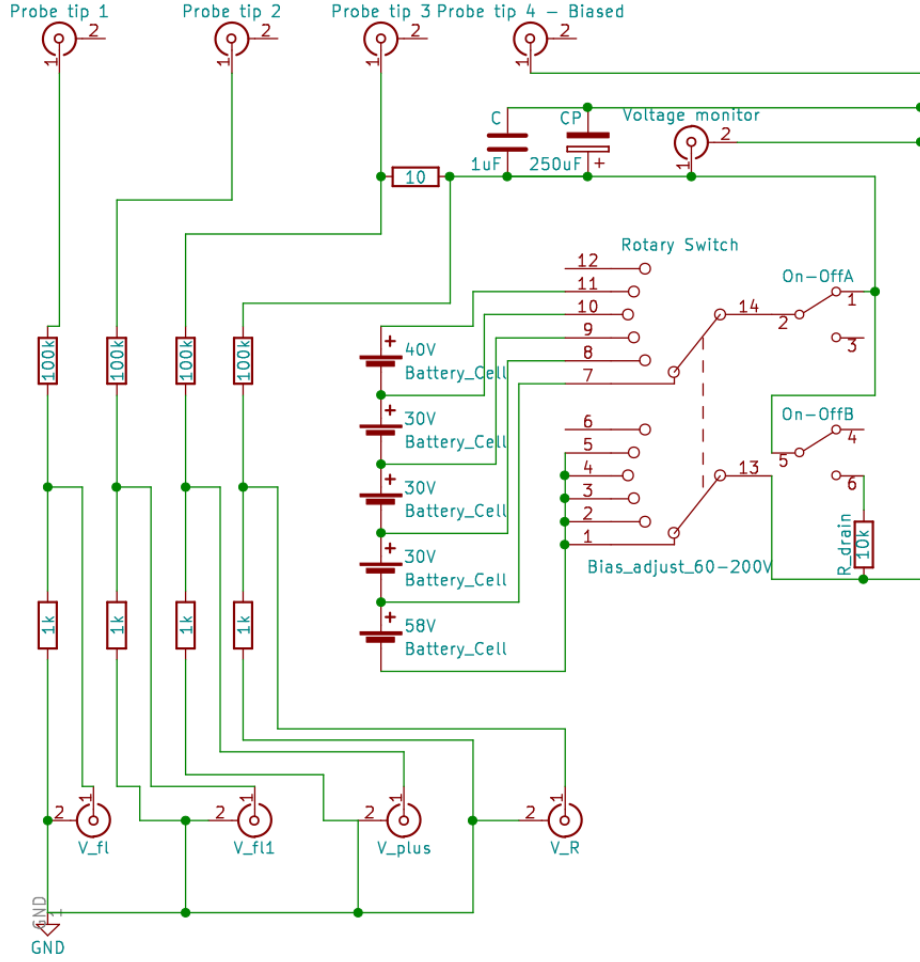
Figure 4.7: Triple probe power supply schematics.

polarity, specifically tuned to detect modes that are integer multiples of the modulation of that winding. This diagnostic technique is limited, as it requires separate coils for different modes. Alternative approach appeared with the introduction of digital data processing - a discreet array of Mirnov coils. These are sets of individual coils that rely on post processing techniques for analysis. One array of 12 discreet coils with equal angular separation was utilized in this experiment [32]. Coils are wound 200 turns each with 30 AWG wire around a teflon strip (3cm by 0.25cm), with constant poloidal spacing of $\pi/6$ in following locations:

$$\theta_i = -15° - 30° \times (i-1), i = [1, 2, ..., 11, 12] \tag{4.16}$$

With counting starting at the LFS (outermost side), as can be seen on the Fig. 4.8. Due to equal separation no interpolation is necessary for mode analysis (DFT can be applied directly due to constant spatial sampling rate). For 12 coils in an array, the maximum resolved mode number is $m = 6$, effectively covering 7 modes: $m = [0, 1, ..., 6]$ [33].

As this array is located outside of the vacuum vessel, attenuation of the magnetic field by bellows should
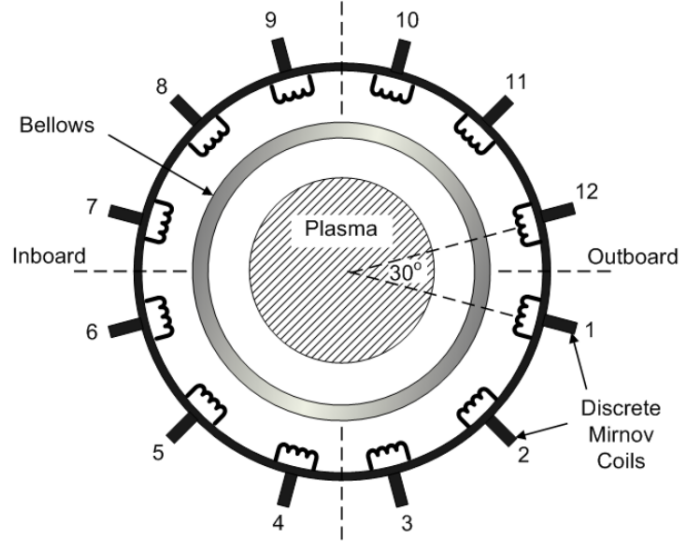
Figure 4.8: Arrangement of Mirnov coils array. Adopted from Adopted from: Sayf Gamudi. Investigation of magnetohydrodynamic fluctuation modes in the stor-m tokamak. Master's thesis, University of Saskatchewan, 2009. `https://harvest.usask.ca/handle/10388/etd-07302009-071402`. Accessed: 2019-09-30.

be taken into consideration. For the thickness of bellows $\Delta x = 0.5$ mm, fabricated out of stainless steel. Attenuation is exponential $e^{x/\delta}$, where δ is characteristic penetration depth of the wave of frequency f, called the skin depth:

$$\delta = \left(\sqrt{\pi f \mu \sigma} \right)^{-1} \tag{4.17}$$

where $\mu \approx \mu_0 = 4\pi \times 10^{-7}$ H/m is magnetic permeability in vacuum and σ conductivity, in particular for stainless steel: $\sigma_{steel} = 1.45 \times 10^6$ S/m. it is possible to estimate the cut-off detectable frequency (at assumption that skin depth is equal to thickness of bellows $\delta = \Delta x$), resulting in:

$$f_{max} = \frac{(1/x)^2}{\pi \mu \sigma_{steel}} \approx 700 \text{ kHz} \tag{4.18}$$

which implies that attenuation is of no consideration up to values of hundreds of kHz. In STOR-M, the MHD fluctuation frequency is $10 - 50$ kHz, well below the cut-off frequency.

4.6 Data acquisition and processing

Data acquisition (DAQ) system in the STOR-M experiment consists of several modules. The main digitizer module, that is active during each discharge, records main plasma parameters, such plasma current, I_p, loop voltage, V_l, plasma position, ΔH, and others. It is a system configured to run 16 channels with sampling rate of 10kHz and 12-bit resolution per channel. Additional National Instruments (NI) PXI-6133 modules are used as supplementary modules for data collection from other diagnostics. These modules

have a maximum sampling frequency of 2MHz with a 16 bit resolution. All of the outputs from further discussed diagnostics were digitized via LabView code operating on NI PXI modules at 2M samples/s rate and 16-bit resolution of ADC. Data post processing was performed using GNU Octave, a Matlab compatible programming environment [34]. Spectral analysis of data was performed using Matlab/Octave compatible Large Time-Frequency Analysis Toolbox (LTFAT) [35]. In order to conduct post processing, it was necessary to combine data from all of the active DAQ modules, calibrate and arrange it. For this purpose Octave/Matlab script was developed. It outputs *struct*-file that contains data from several shots, organized in a convenient way for analysis and visualization.

CHAPTER 5

RESULTS AND DISCUSSION

This chapter presents the results of the measurements of parameters related to the STOR-M plasma properties, including the the line averaged density calculated using a program developed during this research project, magnetic fluctuation signals in terms of the their modes and cross-correlation to reveal the propagation angular velocity, the edge electron density, temperature and space potential measured with the triple Langmuir probe at the STOR-M edge region, and finally the density fluctuations measured with a reflectometer.

5.1 Basic STOR-M discharge features

Figure 5.1 presents basic plasma discharge waveforms including loop voltage, V_l, plasma current, I_p, Hydrogen alpha line intensity, H_α, position of plasma column, ΔH, gas puffing, V_{puff} and line-average density, n_e, of the shot 323737. Time countdown starts with the commutation of two capacitor banks (slow and fast) to the coils located on the core of the transformer, which induces toroidal electric field in the vacuum vessel and causes the breakdown. Dip in loop voltage and rise in plasma current roughly at 1 ms indicate the beginning of the discharge and appearance of plasma. Plasma current increases and other parameters evolve during the ramp-up phase which happens within 1 ms $\leq$ t $\leq$ 10 ms. The 'flat-top' region of the discharge, $10 \leq t \leq 20$ ms, is suitable for measurements as no abrupt changes occur to any of macro-scale parameters. After 20 ms of the discharge, the level of fluctuations in loop voltage increases, plasma current starts to slowly decay up to the 34 ms when the discharge terminates.

5.2 Interferometry

To overcome problems of analog fringe-counter, interferometer signals were digitized and processed. For the zero-crossing algorithm to be applicable, both fringes have to oscillate around zero, so that zero crossing can be detected. This requires removal of any DC component from signals, which is problematic, as density and, hence, the phase growth rate, along with duration of the shot are inconsistent. This implies that straightforward subtraction of mean value from signals does not strictly guarantee proper 'zeroing', and can only give initial point for further adjustments. Problem is especially prominent with $\cos(\phi)$ signal, as in absence of plasma it will always be positive, causing higher mean value and overcompensation when
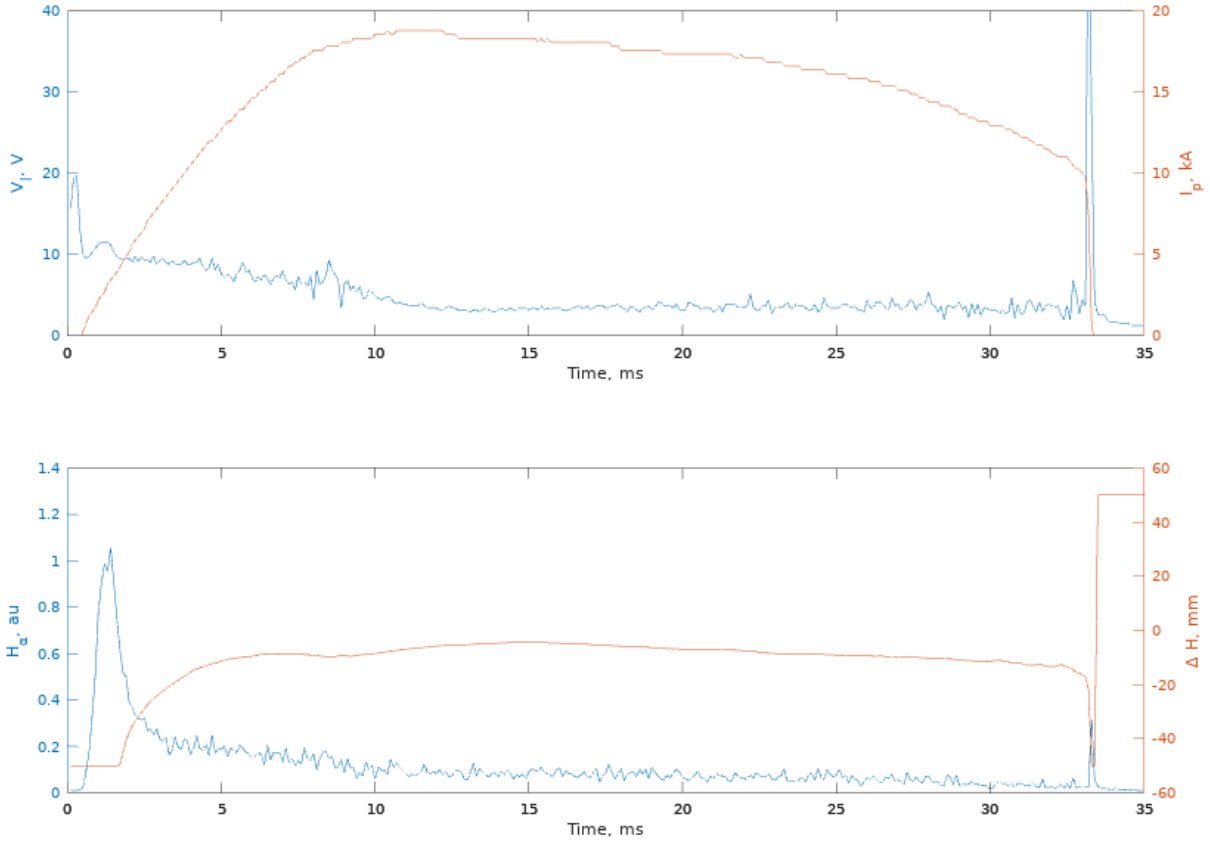
Figure 5.1: Main parameters $(I_p, V_l, \Delta H, H_\alpha)$ of the STOR-M shot 323737.

average is subtracted. Phase calculated via zero-crossing algorithm is a non-linear function of initial fringe positions and it is not possible to predict or approximate any constant offsets or way to systematically adjust for them. A program developed solves this problem by application of readily available computational power - phase is calculated for a set of offsets, until a satisfactory result is achieved. That explains the high importance of optimized implementation of algorithms for phase calculation, and necessity for their simplicity and robustness. In the particular case of Matlab/GNU Octave, it required vectorization of calculations. As the majority of calculations within the algorithm are binary, even large array sizes (associated with high sampling rate of DAQ) does not require any noticeable time for processing. For example application of vectorized zero-crossing algorithm to 25000 element data vectors, takes less than 10 ms to compute the result. In comparison, the un-optimized application of the same algorithm via conditional *for*-loop takes over 40 seconds for the processing of the same data set. The function used to calculate density is invoked with two vectors, containing data from fringes $I(t)$ and $Q(t)$ respectively. Prior to phase calculation, signals are unitary normalized and mean is subtracted. Then various offsets are applied to each signal and phase is calculated for each pair of offset values. The calculated phase should satisfy several criteria in order to be considered successful:

- Initial and final phase values are the same and equal to zero: $\phi_I[1] = \phi_I[end] = 0$.

- Phase cannot have positive values for density to be positive (following from 3.27): $\phi_I[t] \leq 0$.

- Certain threshold value,M, has to be reached: $max(|\phi_I[t]|) \geq M$

Program presents the user with the positions of both fringes relative to zero, along with the calculated phase. The user is prompted to confirm the calculation, asking whether the result is satisfactory. If the calculation is not validated by the user, the algorithm will proceed with attempting different offsets to bias signals. If none of the results suggested by the algorithm are satisfactory, the user is prompted to manually input values for bias corrections. Results of the off-line phase calculation and interface are illustrated in Fig. 5.2. After calculation, zero-crossing data is saved. Then, an algorithm for continuous phase calculation is invoked, to be performed over the obtained data, providing better resolution within the density steps. Results for zero-crossing and continuous counting are saved separately. The resultant density for the STOR-M shot 323737 is shown on Fig. 5.3 as an example.
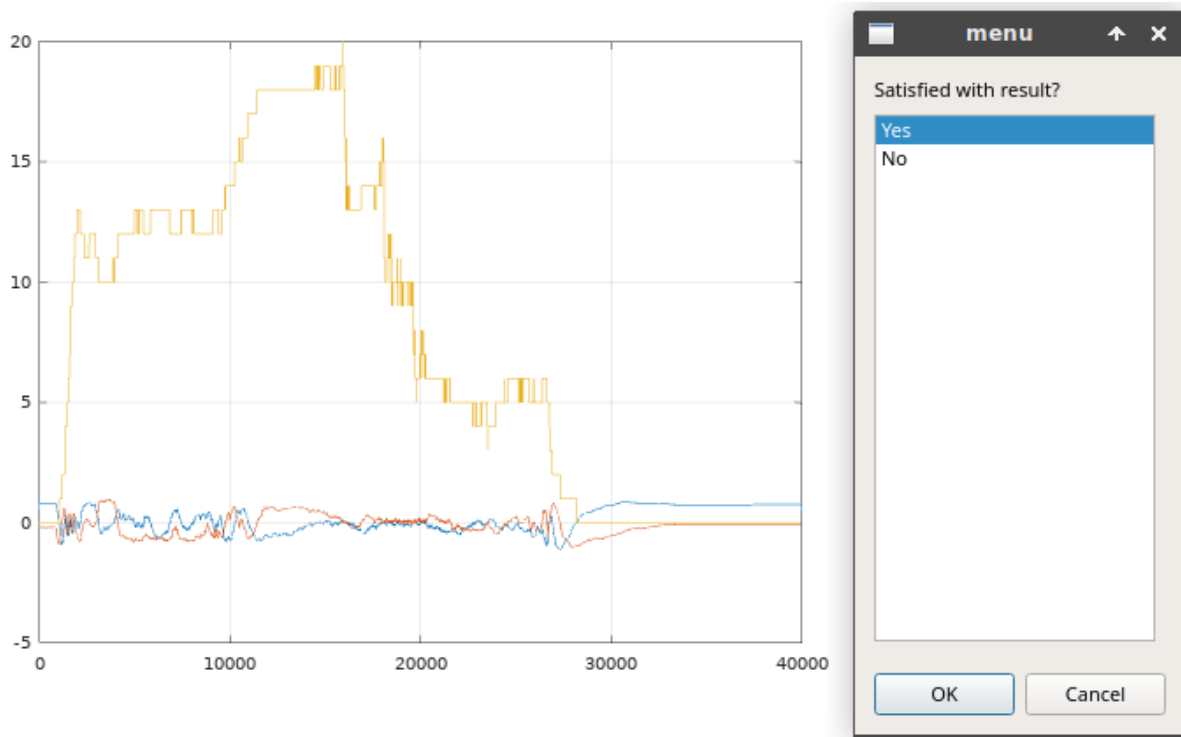
Figure 5.2: Interface for the *GNU Octave* program prompting a user to verify the acceptance of the density calculation.
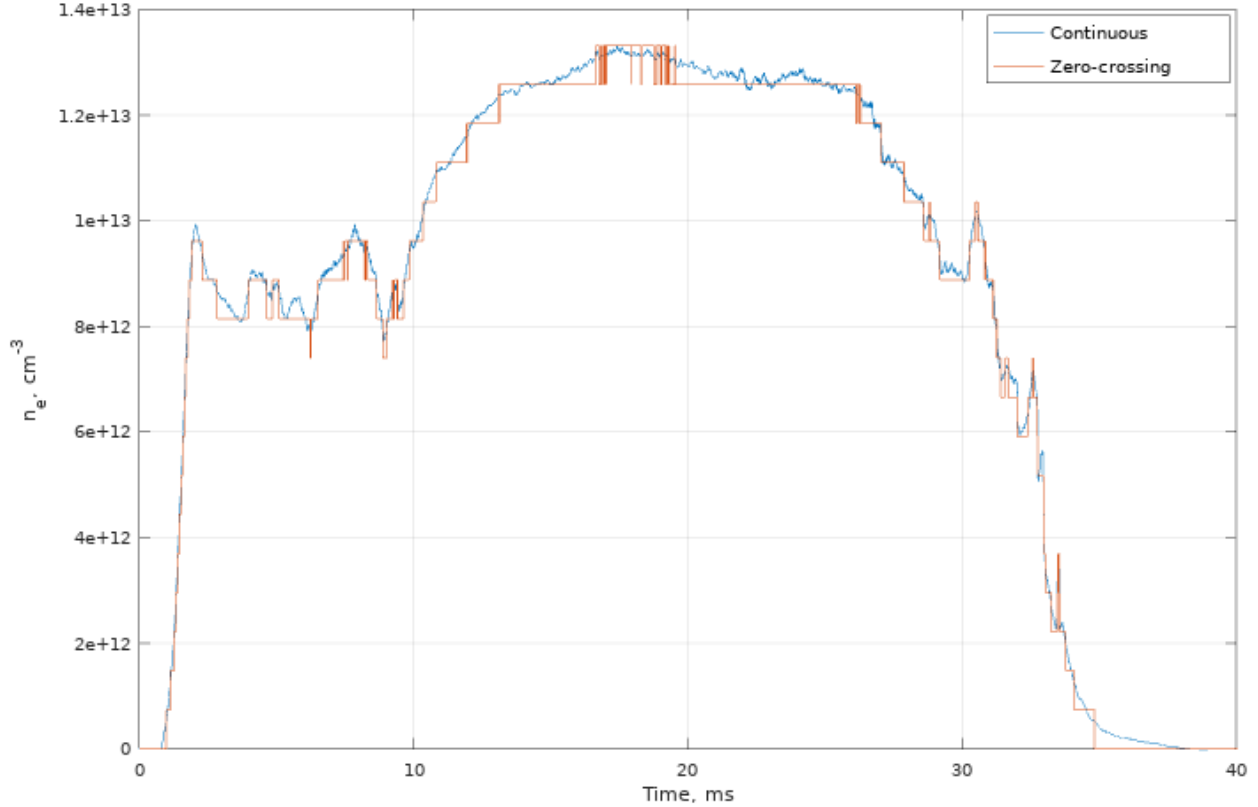
Figure 5.3: Comparison between the density measurements via "zero-crossing" algorithm and continuous phase counting for the STOR-M shot 323737.

5.3   Magnetic fluctuations

Signals from the array of 12 coils collected during the shot 323737, along with the expanded plot for the time interval from 13 to 18 ms, are presented in Fig. 5.4 in the form of the heatmap (colored 2D contour plot).

Figure 5.5 provides a comparison between two of the spectrograms of Mirnov array signals at the low field side (LFS, outer board of the torus) and at the high field side (HFS, inner board) of the poloidal cross section. This comparison shows that the frequency (about 20-30 kHz) of the oscillations does not change with the poloidal angle, but the magnitude of the fluctuations decreases at HFS, possibly due to higher value of stationary magnetic field, $\mathbf{B_0}$. The signal at LFS is of particular interest as it is one of the closest poloidal locations to the TLP and of the reflectometer probing region and it will be used for further comparison.

5.3.1   Correlation measurements

Cross correlation between neighboring Mirnov signal channels is remarkably high. Minding equal angular spacing of the coils, it was used to estimate the poloidal angular velocity of the fluctuations by means of determination of time lag corresponding to the highest cross-correlation value and the poloidal angular separation between the two probes. Figure 5.6 shows the plot of the cross-correlations between the signals
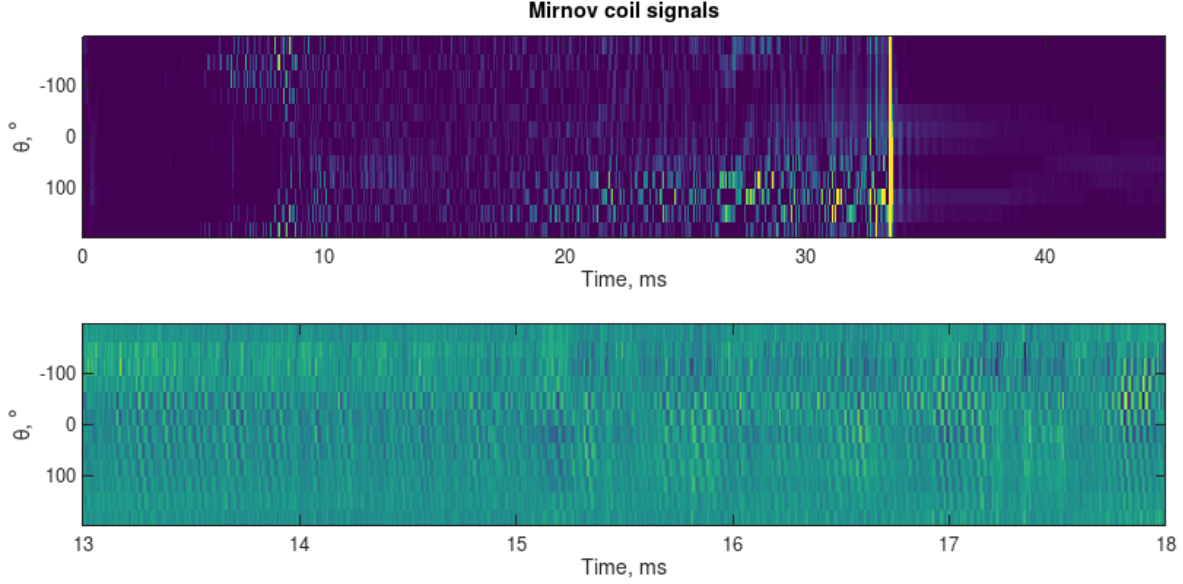
Figure 5.4: Heatmap of Mirnov coil signals for different timescales for the STOR-M shot 323737.

measured by the Mirnov coils in the time interval between 13 and 18 ms during the discharge 323737. The correlation is the strongest on the LFS (probably due to higher amplitude of oscillations) and the angular velocity in poloidal direction appears to be the lowest there as well.

5.3.2 Mode analysis

Spectral intensity for poloidal modes ($m = 0, ..., 6$) and their time evolution is presented in Fig. 5.7 for the discharge 323737. It can be clearly seen that the signals are attributed to the actual MHD activity, and are not induced by pick-up of toroidal electric field of Ohmic-heating, as they appear only after plasma is formed and not when OH(Ohmic heating) bank is fired (peak of V_l at the beginning of the discharge). The initial phase of the discharge, 1 ms $\leq$ t $\leq$ 5 ms, is dominated by low mode numbers, mostly $m = 0$. When the discharge current starts to approach the plateau during the final ramp-up phase ($5 \leq t \leq 10$ ms), some MHD activities can be observed simultaneously with both high ($4 \leq m \leq 6$) and low ($0 \leq m \leq 1$) modes. However, it is important to highlight that in such straightforward analysis the appearance of the 0-th order mode may be possibly attributed to aliasing, caused by undersampling of the signal (insufficient number of poloidal locations), but it appears to be unlikely in this particular case since the amplitude of the $m = 0$ mode is steadily decreasing and appears to be unaffected by the appearance of higher order modes (which would be the case with aliasing). The amplitude of MHD activity during the 'flat-top' region of the discharge, $10 \leq t \leq 20$ ms, is low and does not have any significant hot-spots. After 20 ms of the discharge, mild activities at higher modes appear. As current starts to ramp down at 25 ms of the discharge, the MHD activity becomes more and more prominent, originating from the higher order modes, gradually transforming to lower modes, eventually leading to the disruption at 34 ms.

68
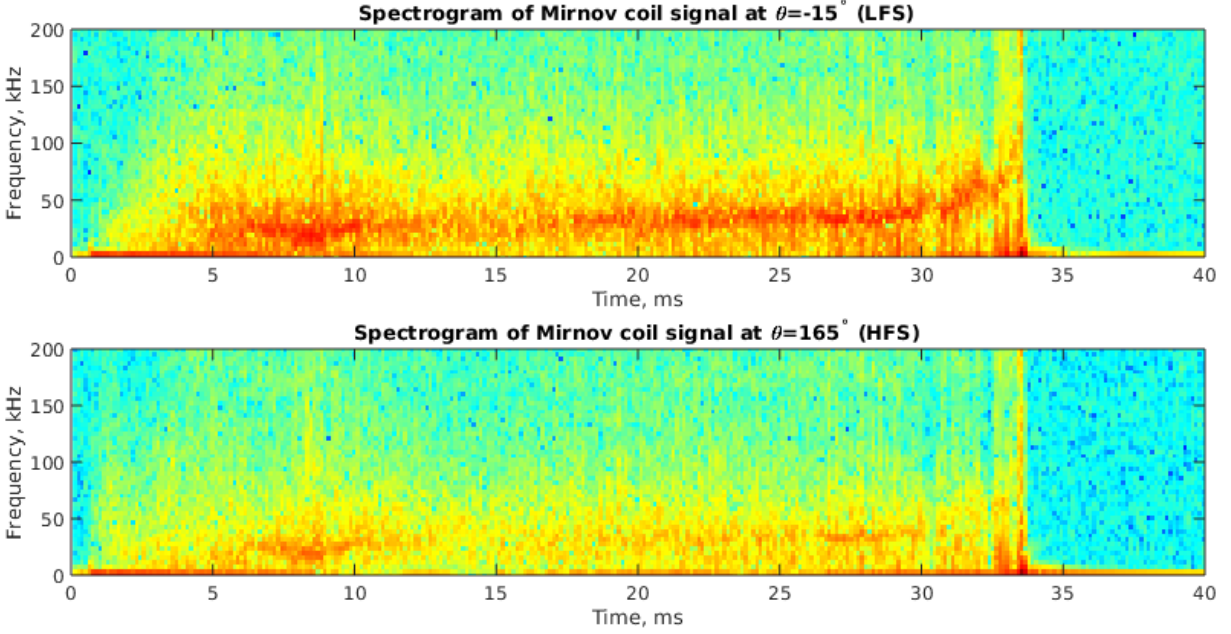
Figure 5.5: Comparison of spectrograms between LFS and HFS of Mirnov coils located accordingly at $\theta = -15°$ and $\theta = 165°$ for the STOR-M shot 323737.

5.4   Local plasma density, potential and electron temperature

The Langmuir triple probe signals were measured at minor radius in the Scrape-off-Layer (SOL) and edge regions from $r = 14.5$cm to $r = 10$cm. The measurements at larger insertion depths (smaller radius location) were not possible as not only the probe was exposed to excessive thermal loads, but more importantly caused instabilities and triggered disruptions of the discharge. The Key STOR-M discharge parameters, such as plasma current, $I_p(t)$, and plasma loop voltage, $V_l(t)$ were utilized to judge the effects of the presence of the probe on the plasma quality. These effects for different radial locations of the probe are presented in Fig. 5.8. It can be seen that the radial locations smaller than $r_{TP} < 12$ cm cause significant decrease in the peak plasma current and duration of the discharge. Degradation of plasma parameters appear to be proportional to insertion depth of the probe. Following these findings and considering possible negative effects, conservative radial location of 14.5cm was chosen for the TLP, in the majority of experiments to guarantee that the effects of the probe on discharge parameters can be neglected. This position was kept constant during experiments with reflectometry and MHD mode analysis. The behaviour of the electron temperature, $T_e(t)$, plasma density, $n(t)$, floating, $V_f(t)$, and plasma, $V_p(t)$, potentials were investigated based on the slow time-varying

69
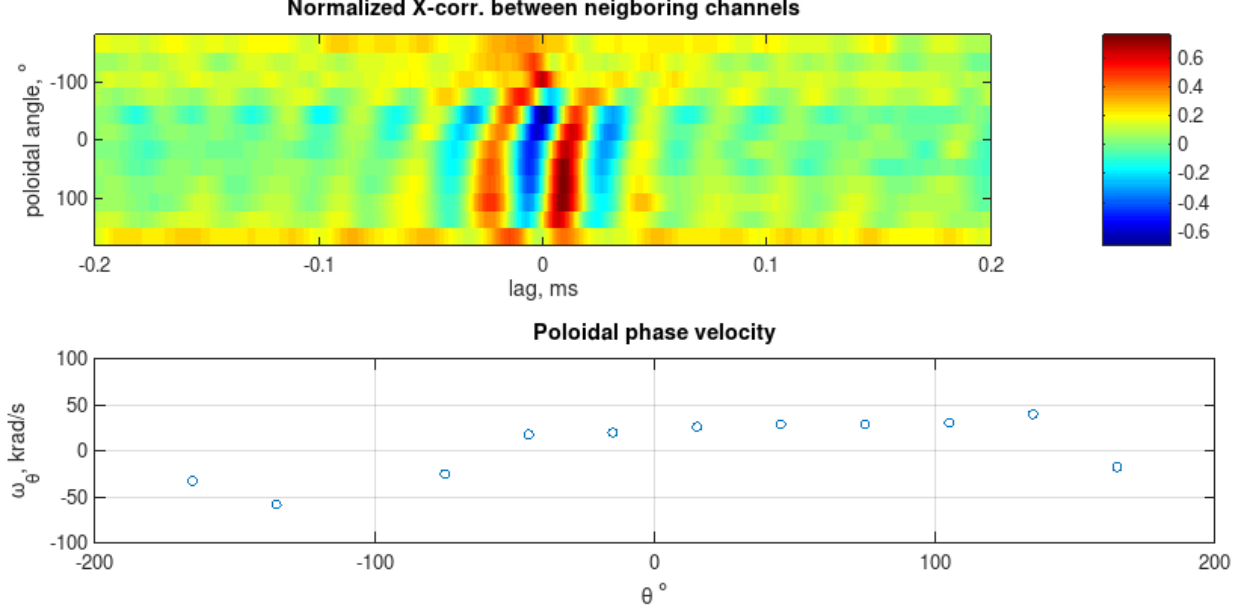
Figure 5.6: Cross-correlations between signals measured by Mirnov coil coils, along with a graph of the poloidal angular velocity $\omega_\theta(\theta)$ as a function of poloidal angle θ.

and high frequency fluctuation components:

$$T_e(t) = \bar{T}_e(t) + \tilde{T}_e(t) \tag{5.1}$$

$$n_e(t) = \bar{n}_e(t) + \tilde{n}_e(t) \tag{5.2}$$

$$V_p(t) = \bar{V}_p(t) + \tilde{V}_p(t) https://www.overleaf.com/project/ \tag{5.3}$$

The slow time-varying component is extracted by taking a sliding average over 400 samples of the measured data or over $200\mu s$ since the sampling frequency was 2 MHz . The fluctuating component can be extracted using formula 5.1. The fluctuating components of the TLP signals and parameters are examined at the 'flat-top' phase of the discharge when the plasma current, $I_p(t)$, and plasma loop voltage, $V_l(t)$, are almost constant. For that purpose a 5ms time frame between 13 to 18 ms of the discharge was selected. The fluctuations of parameters measured by TLP and other diagnostic tools will be compared and discussed in the following Sub-sections.

5.4.1   Electron temperature

TLP allows direct measurement of electron temperature evolution, $T_e(t)$, by proper scaling of voltage difference between two of its pins. The calculated slow time-varying electron temperature is plotted as a function of time for the STOR-M shot 323737 in Fig. 5.9. The result is in good agreement with previous findings on STOR-M [36], providing $\bar{T}_e(t)$ in the range of 10-15 eV during the discharge. The previous measurement was based on the voltage scan to produce a I-V characteristics curve in order to extract the information on
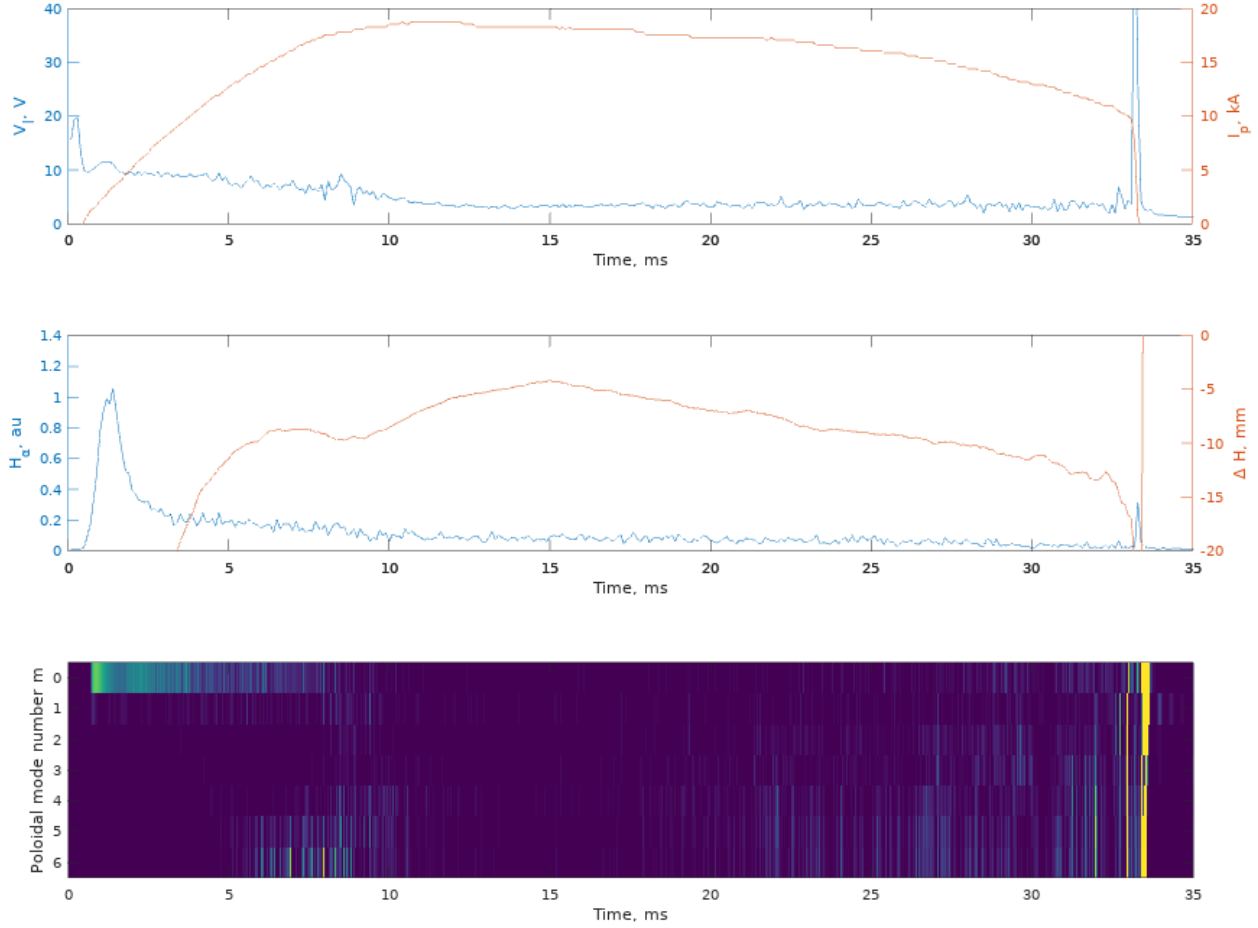
Figure 5.7: Main parameters $(I_p, V_l, \Delta H, H_\alpha)$ of the STOR-M shot 323737 along with the heatmap of mode distribution.

electron temperature, density and space potential. The temporal resolution was about 2 ms. For the first time onSTOR-M, TLP was used in this project to achieve high temporal resolution measurements of local plasma parameters. The evolution of spectral composition of the fluctuating component of $T_e(t)$ is analyzed via STFT (1024 point, ≈ 0.5ms, Hanning window with 50% overlap) and the result is presented in Fig. 5.10. It demonstrates widespread spectrum mostly contained within the 100kHz range, without any well determined peaks, but with highest values somewhere around 50kHz.

5.4.2 Electron density

Plasma density is calculated based on the directly measured ion saturation current and electron temperature. The value of the slow varying component, $\bar{T}_e(t)$, is used for that purpose. Following the procedure described above, averaged plasma density, $\bar{n}_e(t)$, and its fluctuating component, $\tilde{n}(t)$, are calculated. Averaged density from TLP is compared with interferometer measurements in Fig. 5.11. It can be seen that signals share some common features, specifically in the beginning of the discharge, but during the discharge plasma density in
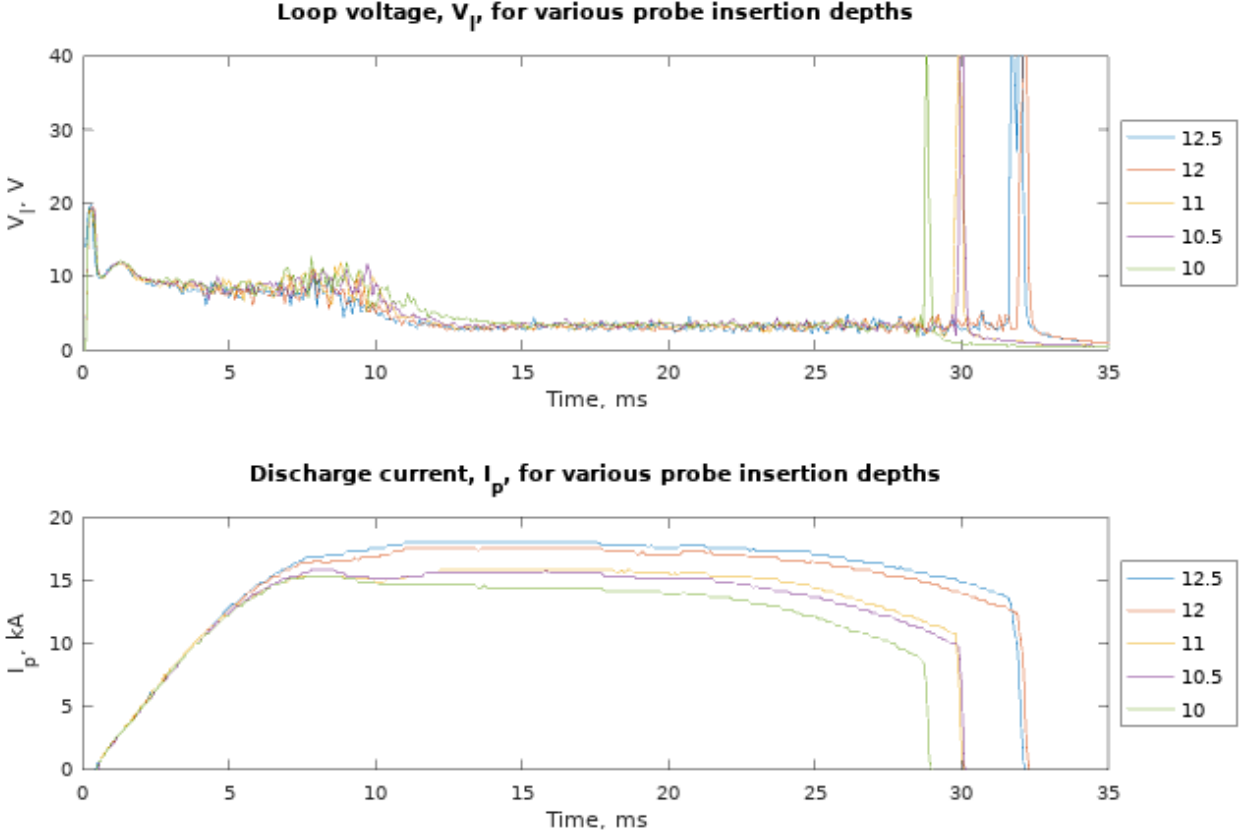
Figure 5.8: Effect of insertion of the probe on discharge parameters (I_p, V_l) for various radial locations of the probe (cm).

SOL stays almost constant and only during the termination phase of the shot large amplitude spikes can be observed.

The spectral composition of density fluctuations is analyzed via STFT analogous to previous signals (1024 point 0.5ms, Hanning window with 50% overlap) with results depicted in Fig. 5.12. The result is reminiscent of electron temperature fluctuations - spectrum is widespread without clearly visible maximum, with the highest intensity at approximately 50kHz.

5.4.3 Floating and plasma potentials

The floating potential is measured directly in the current TLP set-up with one of the probe tips. The plasma potential, V_p, is obtained by substitution of $\bar{T}_e(t)$ into the Eq. (3.79). Consequently, plasma potential can be utilised for reconstruction of radial electric field if the measurements are carried out at more than two locations, at the same time. The 0.2ms sliding average of the plasma potential for the shot 323737 is shown in Fig. 5.13.
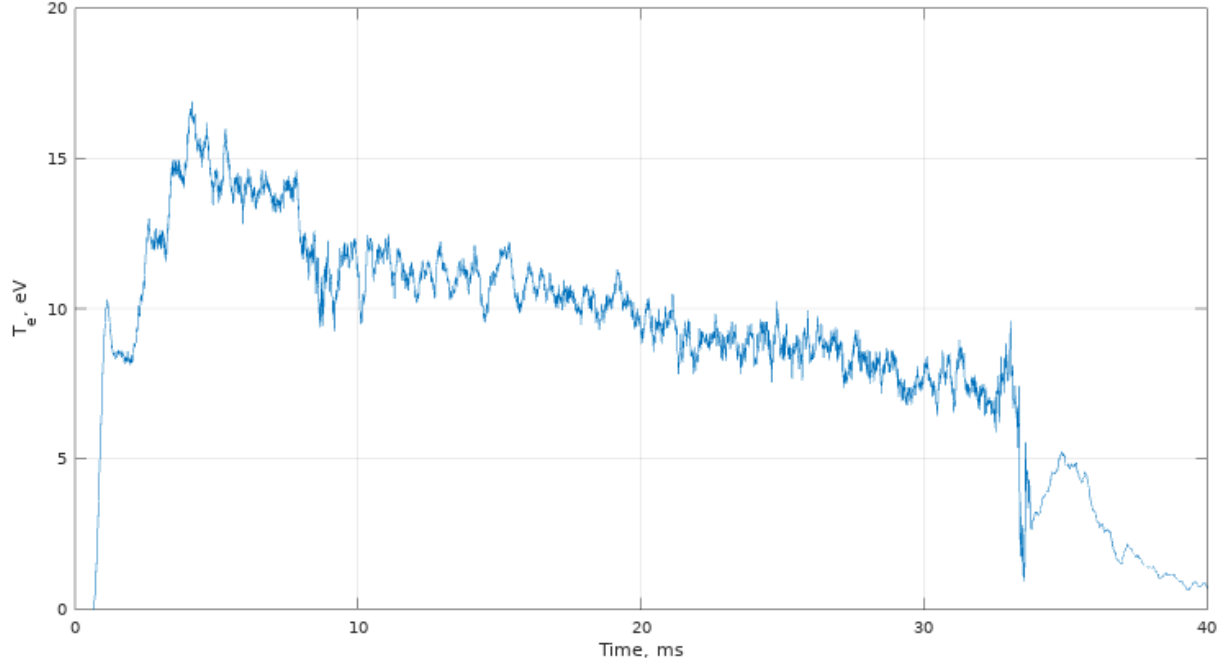
Figure 5.9: Mean (slow time-varying) electron temperature, $\bar{T}_e$, sliding average over 0.2 ms of the STOR-M shot 323737.

5.4.4 Radial profile reconstruction

Series of experiments was conducted to reconstruct radial profiles of plasma parameters via the triple probe. Measurements for each insertion depth were taken shot-by-shot, with 0.5 cm increments, starting from 14.5 cm down to 12.5 cm, resulting in 5 measurement locations. The discharge parameters of shots 326786, 326791, 326793, 326795 and 326798 were kept identical for all the measurements and only probe insertion depth was varied. Similarity between discharges can be verified via line-averaged density measurements which are of remarkable similarity from shot to shot, they are demonstrated in Fig. 5.14.

Figure 5.15 shows the slow time-varying (0.2 ms sliding average) evolution of electron temperature, $\bar{T}_e(r,t)$, electron density,$\bar{n}_e(r,t)$, plasma potential,$\bar{V}_p(r,t)$, and radial electric field $\bar{E}_r(r,t)$ The plots are intentionally downsampled to ease visual perception.

Results of spectral analysis of fluctuating components did not reveal any clear dependencies of spectral composition on the insertion depth for none of the parameters. For that purpose, spectrograms of electron temperature, $\tilde{T}_e(r,t)$, electron density, $\tilde{n}_e(r,t)$ and plasma potential, $\tilde{V}_p(r,t)$ were compared. It is hard to specify any particular frequency that is dominant, giving a broad range of frequencies up to 100 kHz.

5.5 Reflectometry

In comparison to data from TLP or Mirnov coils, reflectometer data interpretation is not as straightforward since the reflected signal power and phase depend on many variables and are integral characteristics of plasma
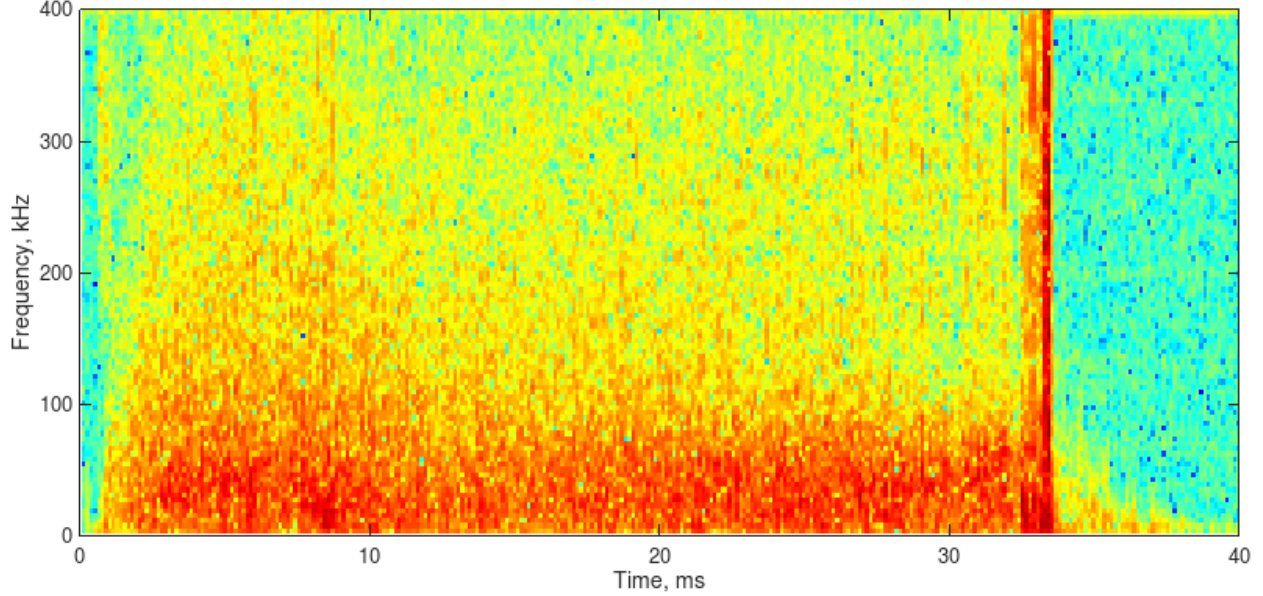
Figure 5.10: Spectrogram of electron temperature fluctuations, $\tilde{T}_e(t)$, of the STOR-M shot 323737.

density along the beam path and shape of the reflective surface. This implies that extra caution should be taken to use the correct model for data interpretation. For example, at the beginning and in the end of the discharge, the reflectometer works effectively as an interferometer. As plasma density is not high enough to cause a reflection, the MW-beam propagates all the way to the inner metal surface of the vacuum vessel at HFS, where it is reflected back, travels back through the plasma and gets detected after. During that period, as plasma density increases, the phase will continuously change and this change should not be mistaken with reflection from plasma. Transition between transmission and reflection can be detected by observing the point when the detected power briefly vanishes, as described in subsection 3.2.1. For the given frequency of reflectometer the critical density can be calculated from 2.48:

$$n_{cr}(17 * 10^9 \text{Hz}) \approx 3.6 * 10^{12} \text{cm}^{-3} \tag{5.4}$$

Thus, allowing to estimate reflecting layer location to be $10\text{cm} \leq \text{r}_{cr} \leq 12\text{cm}$, depending on the steepness of the density profile and peak density value during the "flat-top" phase of the discharge current..

5.5.1 Phase

The reflectometer phase signal from the STOR-M shot 323737, was reconstructed using a combination of zero-crossing and continuous counting techniques, the same techniques used for the 4mm MW interferometer. At the beginning of the discharge, the reflectometer effectively works as a Michelson interferometer, by reflecting from the inner wall of the vacuum vessel. This regime is observed until the time τ when plasma reaches critical density somewhere along the beam path. At that moment the amplitude of the reflectometer signal
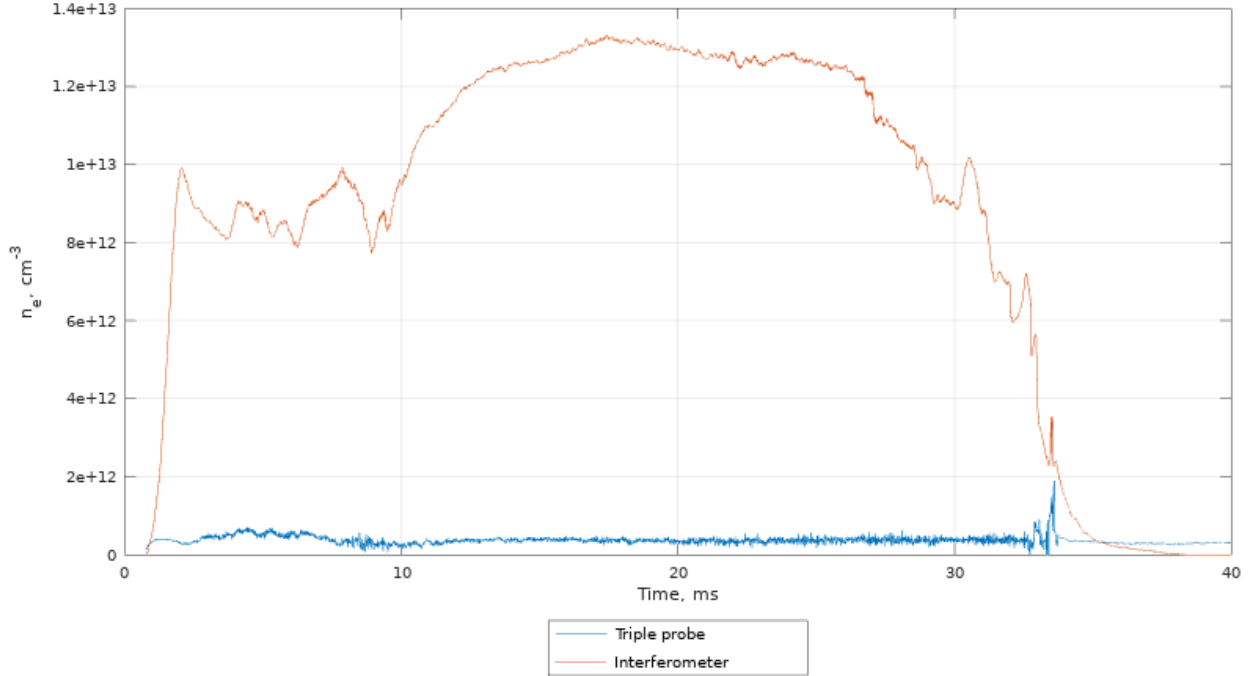
Figure 5.11: slow time-varying electron density measured via TLP (localized), $\bar{n}_{TP}$, compared to interferometry density (line averaged) measurements, $\bar{n}_I$.

almost vanishes. Further, as plasma density grows, an effective reflective surface should grow proportionally and move towards the reflectometer antenna horn, leading to an increase in amplitude of the reflected signal. This is shown in Figure 5.16. Interesting results can be obtained, if treatment discussed in subsection 3.2.4 is applied and phase change is attributed to displacement of the cut-off layer. Total displacement of cut-off layer from τ to 1.7 ms can be calculated if Eq. (3.53) is recalled and actual phase difference of approximately 20 rad is substituted:

$$\Delta x_c = \frac{c}{\omega \tilde{N}} \Delta \phi \approx 9 \text{cm} \tag{5.5}$$

which coincides with the scale of tokamak's minor radius and does not contradict the observed density growth at that moment.

During the period of stable discharge parameters, phase is continuously growing or decaying. This might be attributed to the so-called effect of phase 'run-away'. It was observed in several experiments on other devices [37], [38]. Proposed explanation is as follows: due to the asymmetric shape (f.e. saw-tooth like) of perturbations on the plasma surface, along with their poloidal rotation, causes the main portion of the reflectometer beam to be reflected off-axis. In that region the center of the effective reflection surface shifts from equatorial plane, where it will have non zero component of velocity towards the reflectometer antenna, possibly explaining such behaviour of the signal. According to numerical simulations and experimental observations the phase runaway does not occur when the plasma surface is smooth. Rotation velocity of the perturbations on the plasma surface cannot be deduced from the rate of phase change as it depends on
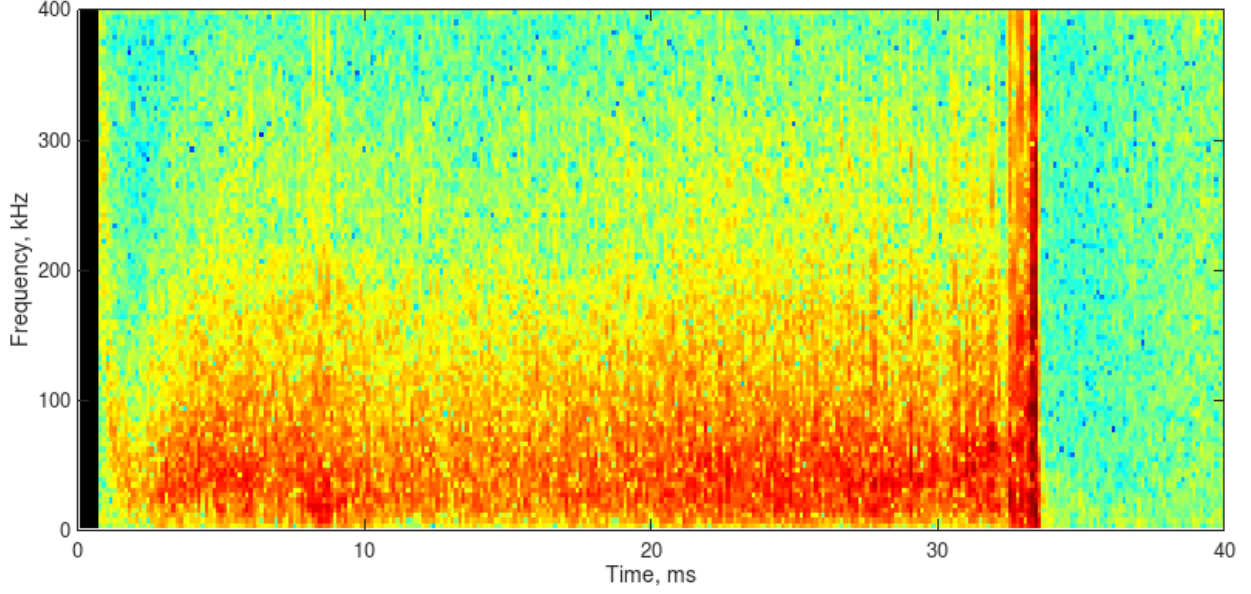
Figure 5.12: Spectrogram of plasma density fluctuations derived from $\tilde{n}_e(t, f)$ measured using TLP.

turbulence parameters [38]. Thus, rendering the reflectometer phase signal useless for the majority of the discharge, as no rapid changes in the phase are observed, just a slow-varying component associated with the phase runaway.

5.5.2 Reflected power

Figure 5.17 shows the reflected power signal spectrogram (bottom panel) for the shot 323737, along with the heatmap of the MHD mode numbers (top panel). The vertical stripes at spectrogram at 14 ms and 30 ms are caused by the undesired capacitive coupling to the mains at 60 Hz. The signal has two distinguishable peaks. The one at roughly 20-25 kHz is present throughout the whole duration of the discharge, and the other one does not appear persistently at higher frequencies around 160 kHz. The two peaks might have come from two origins. The first mechanism may be attributed to the aforementioned problem of coupling to the mains as those highlights occur every 8.3ms, corresponding to the 120Hz frequency or second harmonic of 60Hz of the mains. Alternatively this might be due to the change in the plasma parameters. It can be seen that during the spikes of the MHD activities at high order modes ($4 \leq m \leq 6$), at $5 \leq t \leq 8$, $14 \leq t \leq 16$, $21 \leq t \leq 26$, $30 \leq t \leq 32$ ms, the oscillations at relatively high frequency, $f \approx 165$ kHz, are excited. Possible explanation can be the following: if an assumption is made, that the actual MHD fluctuations are directly affecting the cut-off layer (reflection surface) displacement (e.g. 'frozen-in' magnetic field), which allows to treat perturbations to magnetic flux surface as perturbations to reflective layer. Following from Section 3.2.1, the reflected power modulation will happen in particular case when the wavelength of non-uniformities, Λ,
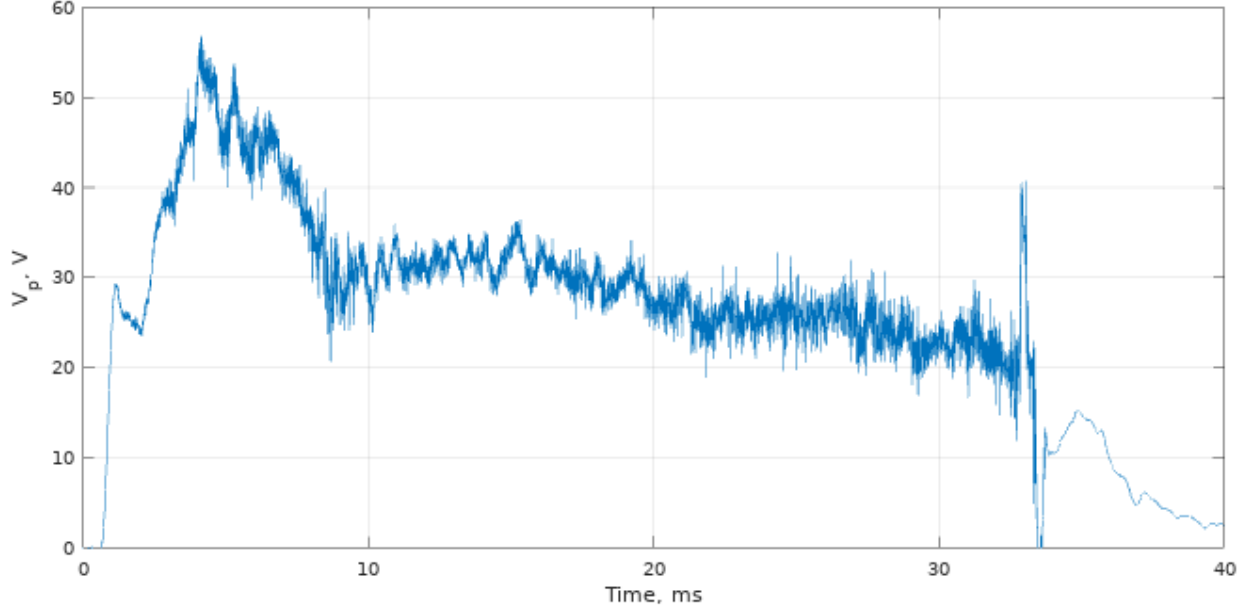
Figure 5.13: Plasma potential, $\bar{V}_p$, , sliding average over 0.2 ms.

of the surface is within certain range, namely:

$$2w/\lambda \leq \Lambda/\lambda \geq 10w/\lambda \tag{5.6}$$

where Λ represents the ripple distance of the mode and can be estimated as $\Lambda = \dfrac{2\pi r_{cr}}{m}$, where r_{cr} is the radial location of the reflecting layer and m is the poloidal mode number. Substitution of $r_{cr} = 11$ cm, $w/\lambda = 1.1$ and $\lambda = 17.65$ mm yields:

$$1 \leq \frac{17.7}{m} \leq 5 \tag{5.7}$$

which implies that poloidally propagating modes in a range of $4 \leq m \leq 17$ will cause modulation of reflected power at the frequency of $f = \dfrac{2v_\theta}{\Lambda}$, defining the rate of phase change of the periodical perturbation of the reflecting surface. This equation can be expressed alternatively:

$$f = \frac{2v_\theta}{\Lambda} = \frac{2\omega_\theta r_{cr}}{2\pi r_{cr}/m} = \frac{\omega_\theta m}{\pi} \tag{5.8}$$

where ω_θ is the angular velocity of perturbations in the poloidal direction, which can be found from the cross-correlation measurements of neighboring coils in the Mirnov array to be $\omega_\theta = 20 - 25$ krad/s.

5.6 Comparison between fluctuation features

The coherence between any two of the following fluctuating components of the measured parameters has been analyzed: reflectometer power fluctuations, $\tilde{Re}_{pow}(t)$, density fluctuations from TLP, $\tilde{n}_e(t)$, and MHD

77
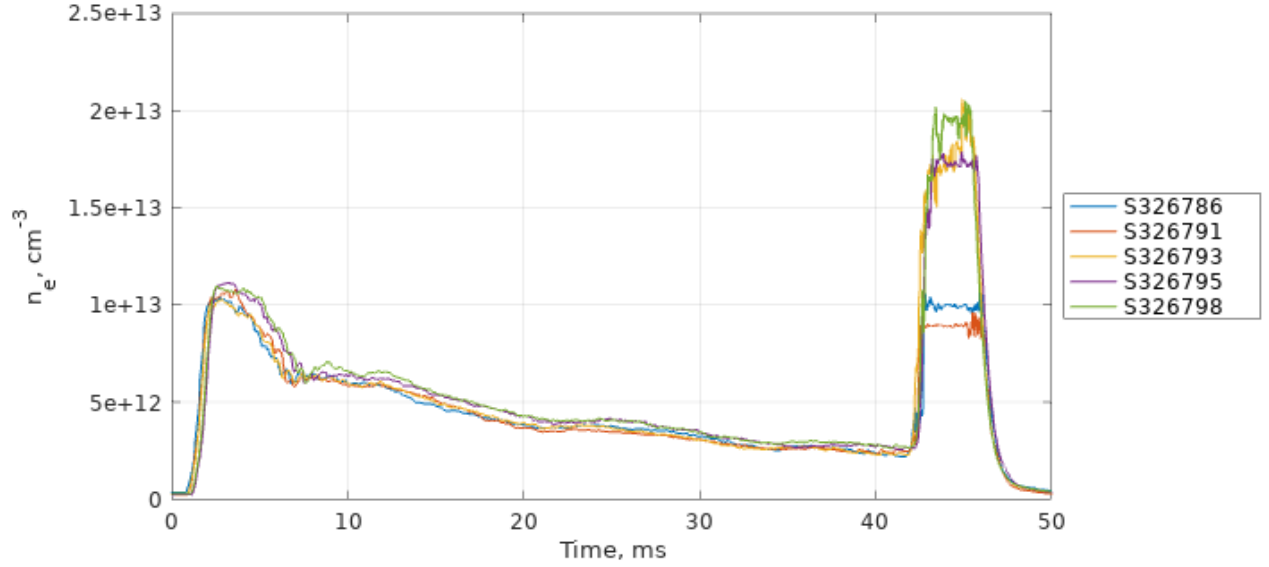
Figure 5.14: Comparison of line-averaged plasma density recorded via interferometer during the discharges used for reconstruction of radial profiles.

fluctuations from one of the Mirnov coils, $\dfrac{\partial B_{\theta 1}}{\partial t}(t)$. Data was taken during the 'flat-top' phase ($13 < t < 18$ms) of the discharge 323737. From the results shown in Fig. 5.18 it can be found that only $C_{Refl \to n}$ and $C_{\partial B/\partial t \to n}$ demonstrate significant values. However, taking into account the spectral composition of the input signals, where PSD is almost fully contained within 100kHz, only $C_{\partial B/\partial t \to n}$ is significant. Phase was not considered, as these diagnostics are toroidally separated. Thus no clear connection between the localized reflectometer power and density fluctuations was established. This means that the long range correlation between those two signals has not been found in this experimental campaign. Contrary to this, the MHD fluctuations are generally global in nature and may affect many localized measurements and any locations (refelctometer and TLP). The findings seem to support the aforementioned hypothesis that 'frozen-in' approximation can be used for high frequency signals.
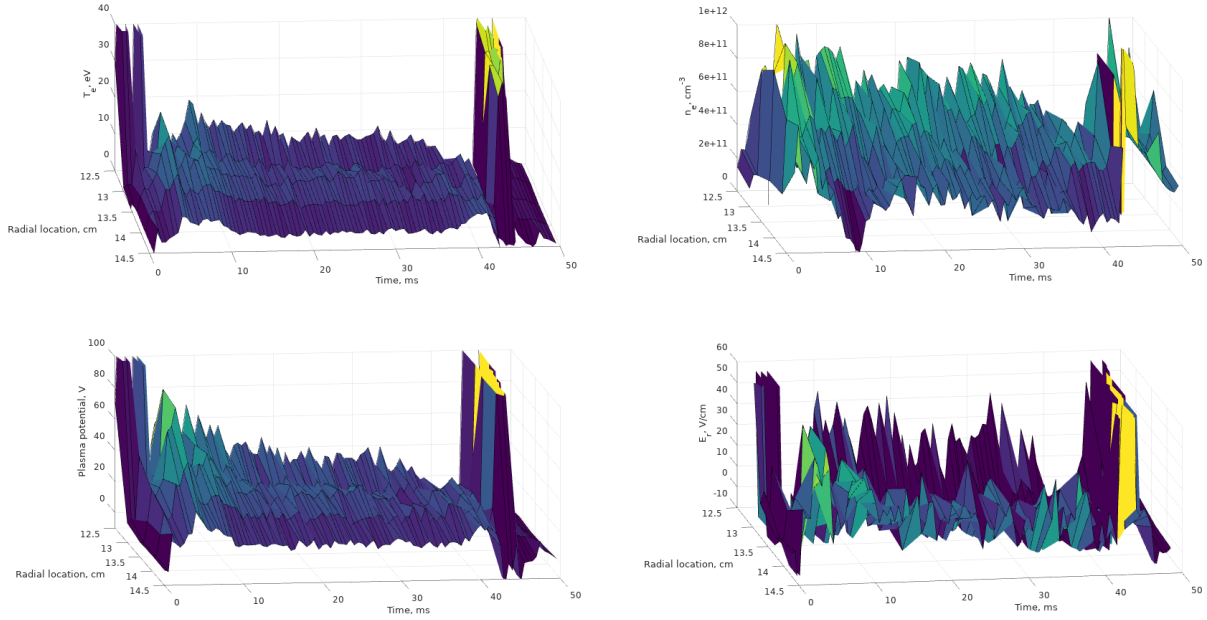
Figure 5.15: Radial profile time evolution of slow varying electron temperature, $\bar{T}_e(r,t)$, plasma density,$\bar{n}_e(r,t)$, plasma potential,$\bar{V}_p(r,t)$, and radial electric field $\bar{E}_r(r,t)$.
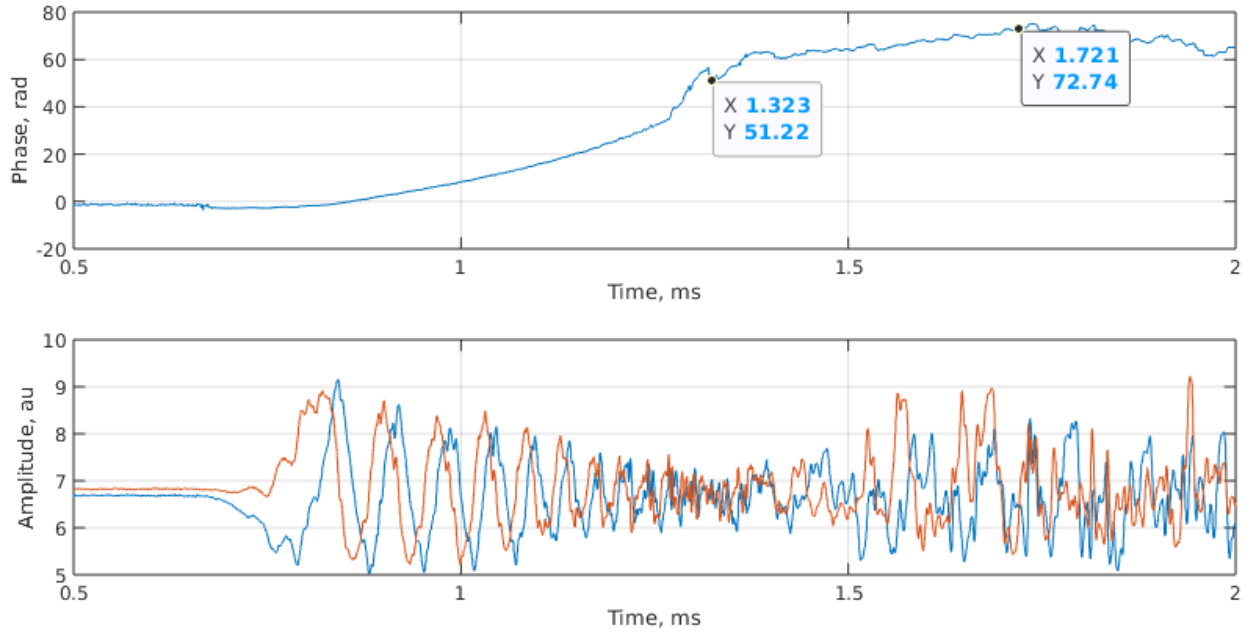
Figure 5.16: Reflectometer phase (top panel) and I and Q signals (bottom panel) around the transition time τ=1.315ms from the interferometry to reflectometry mode.
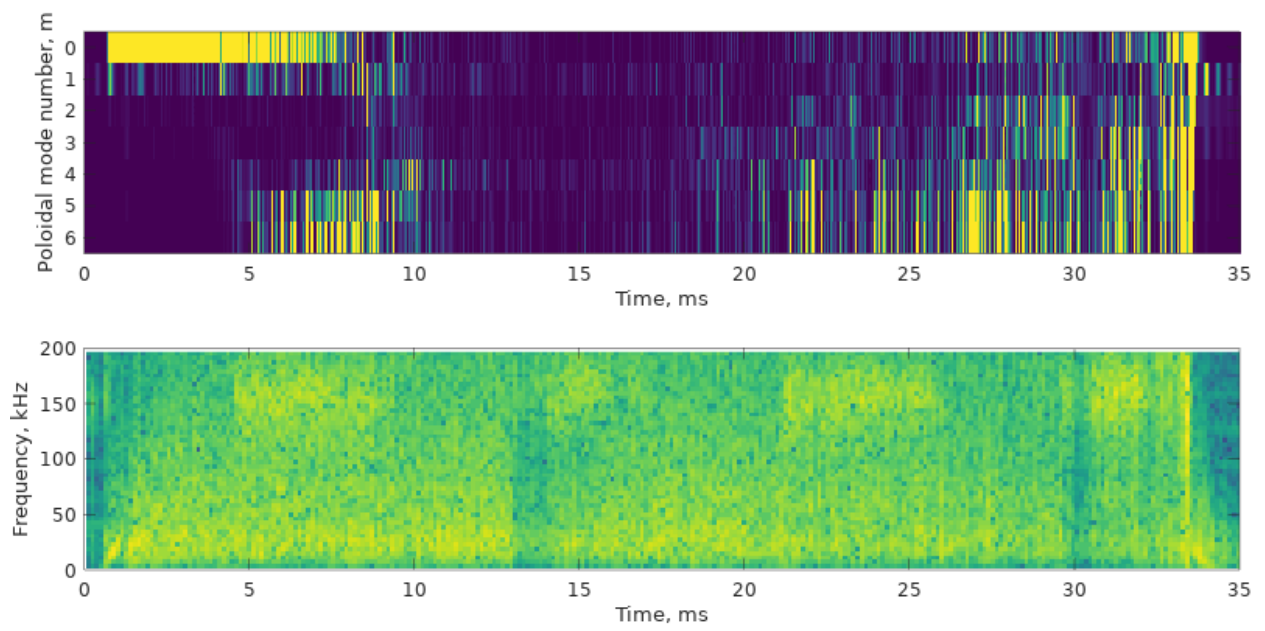
Figure 5.17: Spectrogram of reflected MW-beam power fluctuations (bottom) and heatmap of MHD modes (top).
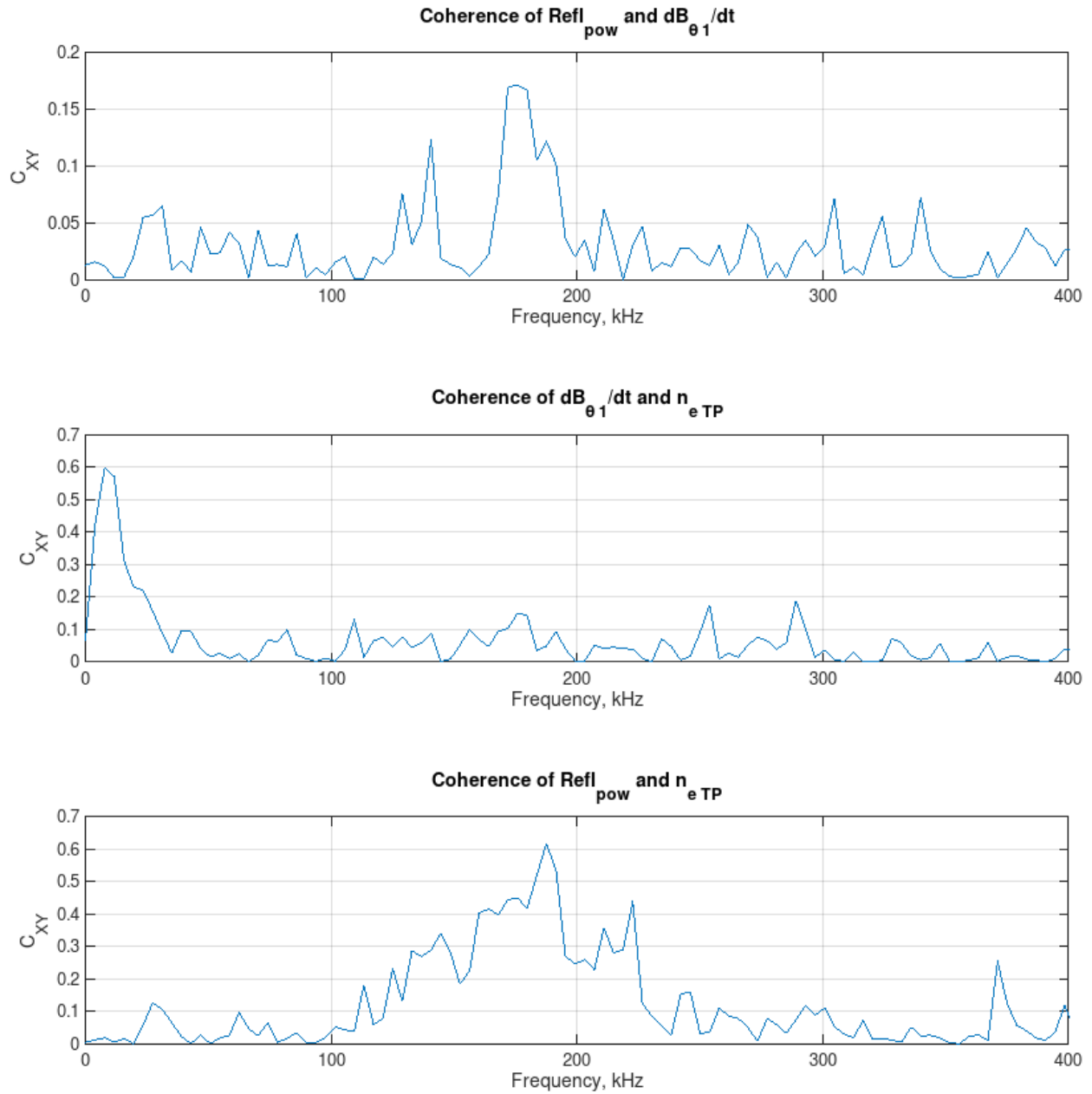
Figure 5.18: Coherence coefficients for the signal pairs (from top): $\tilde{R}e_{pow} - \tilde{n}_e$, $\partial B/\partial t - \tilde{n}_e$, and $\partial B/\partial t - \tilde{R}e_{pow}$.

CHAPTER 6

CONCLUSION

In this chapter results of the work are summarized and a conclusion is drawn. Potential improvements and further directions for investigation are suggested.

6.1 Conclusion

Applications of three different diagnostic techniques to measurements of edge plasma fluctuations in the STOR-M tokamak were studied in this work. During the course of this work, several diagnostic tools on STOR-M were improved and one new successfully implemented. The code for robust phase calculation with increased resolution was developed and implemented for the interferometer and reflectometer.

The triple Langmuir probe has proven to be a useful tool for this study, allowing not only for analysis of fluctuating components, but additionally the time-resolved measurements of plasma density and electron temperature. This allowed reconstruction of averaged time-resolved radial profiles of plasma density, electron temperature and plasma potential. Latter permitted calculation of radial electric field. It is important to note however that this diagnostic does not allow for such spatial resolved measurement within on discharge and requires adjustments to probe positions between discharges with identical plasma parameters. Spectral composition of fluctuating component of probe signals such as ion saturation current, floating potential and derived electron temperature share similar characteristics: detected fluctuations are broadband, mostly below 200 kHz, with a characteristic peak frequency observed at approximately 50 kHz. Time evolution of peak frequency throughout duration of the discharge is within a range of +/-15 kHz.

Interpretation of the reflectometry data has proven itself to be challenging. This is due to the involved model and simplistic set-up of the reflectometer. Nevertheless several interesting effects and observations, such as phase runaway and possible connection between excitation of particular MHD modes with change in frequency of the reflected power fluctuations, were observed. Possible explanations of these effects were proposed and improvements to conceptual model were suggested. Experimental data obtained from a reflectometer during the breakdown and ramp-up was suggested as a possible way to estimate plasma density profile explained in Appendix A.

Data from Mirnov coil array allowed for measurement of poloidal mode number and by cross-correlation measurements it was possible to estimate the poloidal angular rotation velocity of the MHD structures in the

plasma. Spectral composition of fluctuations from Mirnov coils has well defined peak frequency that evolves overtime in a range of 20 50 kHz, which can be speculated to be a geodesic acoustic mode type of oscillation. Spectral evolution is the same for LFS and HFS postions, however at latter amplitude of fluctuations is lower. Evolution of poloidal mode strength distribution ($0 \leq m \leq 7$) was measured and analysed to reveal different level of MHD activity at different stages of the discharge. At moments with high level of such activity the level of fluctuations in other diagnostics, specifically TLP, and coherence between TLP and Mirnov array were observed to be higher. This might serve as a confirms the right interpretation of signals from Mirnov as MHD modes which cause large scale global perturbations to the confined plasma detectable by other diagnostics. Angular velocity of magnetic perturbations in poloidal directions was measured by the means of cross-correlation of neighboring channels to be on order of 15 25 krad/s at LFS of plasma.

Baseline for future studies of edge plasma was established. Results and developments of this work should aid future studies of the STOR-M tokamak plasma in the edge region with triggered H-mode transition, such as plasma biasing, lithium coating, turbulent heating and resonant magnetic perturbations (RMP).

6.2 Future work

Work could be potentially improved by development and numerical simulation of a more sophisticated model of reflection surface described in Section 2.3, for it to include curvature effects and, possibly, asymmetric periodic functions of surface perturbations. Additionally, specifically for studies of fluctuations, it appears beneficial to improve current reflectometer set-up by inclusion of additional horn antennas, which would allow correlation measurement along with Doppler-effect reflectometry. Studies of floating potential fluctuations, using the current triple probe assembly, might give better understanding of direction of their propagation and scale of fluctuations in toroidal direction. Inclusion of rake probes or additional radially separated pins to the probe for radial potential measurements should allow studies of radial electric field evolution.

References

[1] F.F. Chen. *Introduction to Plasma Physics and Controlled Fusion*. Springer, 2016.

[2] B.B. Kadomtsev. *Collective Phenomena in Plasma*. Pergamon Press, 1982.

[3] E.W. Laing B.B. Kadomtsev. *Tokamak Plasma: A Complex Physical System*. CRC Press, 1993.

[4] International Atomic Energy Agency. *Fusion Physics*. Vienna: IAEA, 2012.

[5] Wikimedia Commons. Average binding energy per nucleon in mev against number of nucleons in nucleus. `https://commons.wikimedia.org/wiki/File:Binding_energy_curve_-_common_isotopes.svg`. Accessed: 2019-06-09.

[6] J. Wesson. *Tokamak*. Oxford Science Publication, 2011.

[7] Naval Research Laboratory. *NRL: Plasma Formulary*. NRL, 2004.

[8] J.D. Lawson. Some criteria for a power producing thermonuclear reactor. *Atomic Energy Research Establishment*, 79(4), 1955.

[9] Olivier Février. *Global modelling of magnetic island control in tokamaks*. PhD thesis, Université d'Aix-Marseille, 2016.

[10] A.A. Skovoroda. *Magnitnoye Uderzhaniye Plasmi (Magnetic confinement of plasma)*. Fizmatlit, 2009.

[11] Z. Ren S. Li, H. Jiang and C. Xu. Optimal tracking for a divergent-type parabolic pde system in current profile control. *Abstract and Applied Analysis*, 2014, 2014.

[12] Martin Kocan. *Ion temperature measurements in the scrape-off layer of the Tore Supra tokamak*. PhD thesis, Université Henri Poincaré, 2009.

[13] F. Wagner, G. Fussmann, T. Grave, M. Keilhacker, M. Kornherr, K. Lackner, K. McCormick, E. R. Müller, A. Stäbler, G. Becker, K. Bernhardi, U. Ditte, A. Eberhagen, O. Gehre, J. Gernhardt, G. v. Gierke, E. Glock, O. Gruber, G. Haas, M. Hesse, G. Janeschitz, F. Karger, S. Kissel, O. Klüber, G. Lisitano, H. M. Mayer, D. Meisel, V. Mertens, H. Murmann, W. Poschenrieder, H. Rapp, H. Röhr, F. Ryter, F. Schneider, G. Siller, P. Smeulders, F. Söldner, E. Speth, K. H. Steuer, Z. Szymanski, and O. Vollmer. Development of an edge transport barrier at the h-mode transition of asdex. *Phys. Rev. Lett.*, 53:1453–1456, Oct 1984.

[14] M Keilhacker. H-mode confinement in tokamaks. *Plasma Physics and Controlled Fusion*, 29(10A):1401–1413, oct 1987.

[15] K. H. Burrell. Effects of exb velocity shear and magnetic shear on turbulence and transport in magnetic confinement devices. *Physics of Plasmas*, 4(5):1499–1518, 1997.

[16] Boudewijn van Milligen. Sketch of h-mode profile and pedestal. `http://fusionwiki.ciemat.es/wiki/File:H-mode.png`. Accessed: 2019-09-30.

[17] I.H. Hutchinson. *Principles of Plasma Diagnostics*. Cambridge University Press, second edition, 2002.

[18] D.A. Sheglov E.I. Kuznetsov. *M'etodi diagnostiki vysokotemperaturnoy plasmi (Diagnostic methods of high temperature plasma)*. Atomizdat, 1974.

[19] C.B. Wharton M.A. Heald. *Plasma Diagnostics with Microwaves.* Wiley, 1965.

[20] D.L. Brower et al. Interferometry techniques for fusion plasmas. *Fusion Science and Technology*, 56(5-6):983–988, 2017.

[21] F. Simonet. Measurement of electron density profile by microwave reflectometry on tokamaks. *Review of Scientific Instruments*, 56:664, 1985.

[22] E. Mazzucato. Microwave reflectometry for magnetically confined plasmas. *Review of Scientific Instruments*, 61:2201, 1998.

[23] H. Jeffreys. On certain approximate solutions of linear differential equations of the second order. *Proceedings of the London Mathematical Society*, 23, 1924.

[24] H.A. Kramers. Wellenmechanik und halbzahlige quantisierung. *Z. Physik*, 39, 1926.

[25] G. Wentzel. Eine verallgemeinerung der quantenbedingungen für die zwecke der wellenmechanik. *Z. Physik*, 38, 1926.

[26] L. Brillouin. La mécanique ondulatoire de schrödinger: une méthode générale de resolution par approximations successives. *Comptes Rendus de l'Académie des Sciences*, 183, 1926.

[27] Vitaliy Lazarevich Ginzburg. The propagation of electromagnetic waves in plasmas. *International Series of Monographs in Electromagnetic Waves, Oxford: Pergamon, 1970, 2nd rev. and enl. ed.*, 1970.

[28] G. D. Conway. Scattering of reflectometer signals from rippled surfaces. *Review of Scientific Instruments*, 64(10):2782–2788, 1993.

[29] A.E. Costley A.E. Hubbard and C.W. Gowers. A simple fixed-frequency reflectometer for plasma density profile measurements on jet. *Journal of Physics E: Scientific Instruments*, 20(4):423, 1987.

[30] André Spizzichino. *The Scattering of Electromagnetic Waves from Rough Surfaces.* Pergamon Press, 1963.

[31] H Bindslev. Relativistic effects in plasma reflectometry. *Plasma Physics and Controlled Fusion*, 34(11):1601–1618, nov 1992.

[32] Sayf Gamudi. Investigation of magnetohydrodynamic fluctuation modes in the stor-m tokamak. Master's thesis, University of Saskatchewan, 2009. `https://harvest.usask.ca/handle/10388/etd-07302009-071402`. Accessed: 2019-09-30.

[33] Kadomtsev B. B. Landau damping and plasma echo. *Advances in Physical Sciences*, 95(1):111, 1968.

[34] John W. Eaton, David Bateman, Søren Hauberg, and Rik Wehbring. *GNU Octave version 4.2.1 manual: a high-level interactive language for numerical computations*, 2017.

[35] Z. Průša, P. L. Søndergaard, N. Holighaus, Ch. Wiesmeyr, and P. Balazs. The Large Time-Frequency Analysis Toolbox 2.0. In *Sound, Music, and Motion*, LNCS, pages 419–442. Springer International Publishing, 2014.

[36] H. Jeffreys. On certain approximate solutions of linear differential equations of the second order. *Proceedings of the London Mathematical Society*, S2-23:428–436, 1925.

[37] E Holzhauer, M Hirsch, T Grossmann, B Brañas, and F Serra. Theoretical and experimental investigation of the phase-runaway in microwave reflectometry. *Plasma Physics and Controlled Fusion*, 40(11):1869–1886, nov 1998.

[38] B. Brañas, M. Hirsch, J. Sánchez, and V. Zhuravlev. Geometrical optics interpretation of the phase runaway in microwave reflectometry. *Review of Scientific Instruments*, 70(1):1025–1029, 1999.

Appendix A

Possible approach to approximation of density pro-

file from reflectometer signals

At the beginning of the discharge, while density in plasma column does not exceed the critical density n_c for the frequency of reflectometer beam, reflectometer acts as an Michelson interferometer. This happens as beam propagates through the whole plasma column without reflection, gets reflected by the metallic wall of the vacuum vessel on the high field side and propagates back through plasma column to the antenna. For two dimensional (assuming toroidal symmetry) density profile of poloidal plasma:

$$n(x, y, t) = n_0(t) f(x, t) g(y, t) \tag{A.1}$$

Where $f(x), g(y)$ are density distribution functions along $\mathbf{x}$ and $\mathbf{y}$ respectively and $n_0(t)$ is a peak density at a given moment. Additionally an assumption has to be made regarding constant shape of the density profile time e.g. $n_0(t) \ f(x,t) \ g(y,t) \Rightarrow n_0(t) \ f(x) \ g(y)$, and under assumption of poloidal symmetry these two functions $f(x) \ g(y)$ can substituted by single function of minor radius $h(r)$:

$$n(r, t) = n_0(t) \ h(r) \tag{A.2}$$

Approximation for density profile suggested at [29] is commonly used for measurements on STOR-M, this approximation assumes profile of form:

$$h(r) = 1 - (r/a)^\eta \tag{A.3}$$

Knowledge of parameter η is required to extract any information about peak density n_0. With the use of reflectometer, amplitude of its signal can be utilized to deduce the value of parameter η. Reflectometer signal amplitude vanishes as plasma density n_0 approaches the critical value n_{cR} (see Eq. (2.51)). By observation of the cutoff for reflectometer signal (transition between "interferometer" and "reflectometer" modes) it is possible to determine the time τ_c when plasma reaches critical density n_{cR} somewhere along the reflectometer beam. This gives:

$$n_0(\tau_c) = n_{cR} \tag{A.4}$$

$$\phi_R(t) = \int_0^{\tau_c} \delta\phi_R dt = \int_0^{\tau_c} 2\frac{\omega}{c} \int_{-r}^{r} \left(\sqrt{1 - \frac{n(r,t)}{n_c}} - 1 \right) \ dr \ dt \tag{A.5}$$

Then by substituting density profile from Eq. (A.2) parameter η is numerically fitted to satisfy measured value of total reflectometer phase change from the Eq. (A.5). Calculation results in value of $\eta = 2.7$, which exceeds previously utilized assumption of $\eta = 2$ for calculation of peak density from interferometer measurements. These results, however, require further investigation, as an assumption regarding conservation of density profile is not validated, neither position of plasma column is not tracked at this stage of the discharge.